

ALMA MATER STUDIORUM – UNIVERSITÀ DI BOLOGNA

DOTTORATO DI RICERCA IN

Meccanica e scienze avanzate dell'ingegneria

Progetto n. 4

Ciclo XXIII

Settore scientifico-disciplinare di afferenza: ING-IND/18

**Design and Setup of a New HPGe Detector
Based Body Counter Capable of Detecting
Also Low Energy Photon Emitters**

Presentata da Olaf Marzocchi

Coordinatore dottorato
Prof. Dr. Ing. G. Minak

Relatore
Prof. Dr. Ing. D. Mostacci
Co-relatore
Prof. Dr.-Ing. M. Urban

Esame finale anno 2011

Design and Setup of a New HPGe Detector
Based Body Counter Capable of Detecting
Also Low Energy Photon Emitters

Olaf Marzocchi

Abstract

English

The present work describes the development of a new body-counter system based on HPGe detectors and installed at IVM of KIT. The goal, achieved, was the improvement of the ability to detect internal contaminations in the human body, especially the ones concerning low-energy emitters and multiple nuclides. The development of the system started with the characterisation of detectors purchased for this specific task, with the optimisation of the different desired measurement configurations following and ending with the installation and check of the results. A new software has been developed to handle the new detectors.

Italian

Il presente lavoro descrive lo sviluppo del nuovo sistema di conteggio basato su rivelatori HPGe installato presso l'IVM situato al KIT. L'obiettivo, raggiunto, era quello di migliorare la capacità di rilevazione di contaminazioni interne del corpo umano, specialmente di quelle inerenti basse energie e quelle contenenti nuclidi multipli. La progettazione del sistema è stata effettuata ex-novo, a partire dalla caratterizzazione dei rivelatori acquistati per l'uso, proseguendo con l'ottimizzazione delle diverse configurazioni di misura richieste e terminando con l'installazione e la verifica dei risultati. Parallelamente è stato sviluppato un software per gestire i nuovi rivelatori.

Declaration of Originality

I, Olaf Marzocchi, declare that this thesis is my own work and has not been submitted in any form for another degree at any university or other institute of tertiary education. Information derived from the published and unpublished work of others has been acknowledged in the text and a list of references is given in the bibliography.

Acknowledgments

I wish to thank Bastian Breustedt for the support and guidance throughout the different phases of my thesis work and also the colleagues of the INE-ASF (former HS-KES and later ISF) department for the hospitality I received here.

I would also like to thank Professor Urban for giving me the opportunity to work at KIT in a very stimulating environment and for the advices throughout my thesis work and Professor Mostacci for the supervision he offered me during these four years.

Contents

Abstract	I
Acknowledgments	III
Contents	V
List of Figures	VIII
List of Tables	XI
1 Introduction	1
1.1 In-Vivo Measurements of Radionuclides in Man	1
1.2 History and State of the Art	3
1.3 Objective and Structure of This Work	4
2 Hardware	7
2.1 Sensors	7
2.1.1 Geiger-Müller Counters	7
2.1.2 Dosimeters	9
2.2 Scintillators	10
2.2.1 Phoswich Detectors	12
2.3 Semiconductor Diode Detectors	13
2.3.1 Common Semiconductor Detectors	16
3 Metrology	19
3.1 Basic Calibrations: Energy and Shape	19
3.2 Peak Search and Area Calculation	21
3.3 Efficiency Calibration Methods	24
3.3.1 Interpolation of the Efficiency Values	25
3.3.2 Physical Phantoms	27
3.3.3 Monte Carlo Simulations	29
3.3.4 Numerical Phantoms	35

3.3.5	Sources of Error in Efficiency Calibrations	39
3.4	Nuclide Identification	42
3.5	Limits of detection	43
4	Application to Existing Devices	47
4.1	The Facilities and the Detectors	47
4.1.1	Partial Body Counter	47
4.1.2	Whole Body Counter	49
4.1.3	HPGe Detectors	50
4.2	Characterisation of the Detectors	54
4.2.1	First Revision and Parametric Optimisation	54
4.2.2	Scan and Improvement of the Settings	57
4.2.3	Radiographies and Estimation of the Dead Layer	62
4.3	Validation of the results	65
4.3.1	Contaminated Subject	66
4.3.2	Intercomparison Exercise 2008	68
4.3.3	Validation of a LLNL Torso Voxel Model	70
5	Setup of an Optimised System	75
5.1	Goals	75
5.2	Optimisation of PBC Configurations	76
5.2.1	Set-up of the Modified Phantom	77
5.2.2	The Configurations	79
5.3	Choice of the Counting Configuration	85
5.3.1	The Resulting MDAs	85
5.3.2	The Choice of the System	89
5.4	Definition of the Mechanical Set-Up	92
5.5	Optimisation of a WBC Configuration	98
5.5.1	Method	98
5.5.2	Distributions of Standard Deviations	102
5.5.3	Definition of the WBC Detectors Set-Up	104
5.6	Calibration of the New System	111
5.6.1	Measurements of a LLNL Torso Phantom	111
5.6.2	MDAs for ^{241}Am and ^{235}U	113
6	Application to Routine Measurements	117
6.1	Software Design	117
6.1.1	Shortcomings of the Old Platform	117
6.1.2	Requirements of the New Platform	118
6.1.3	Structure of the Software and Operation	119
6.2	First Applications of the New System	124

6.2.1	Measurement of Potential ^{210}Pb Contaminations	124
6.2.2	WBC Measurements with an IGOR Phantom	129
7	Overview and Conclusions	137
A	Software Developed	139
A.1	Database	139
A.2	Software and Routines	142
A.2.1	Energy Calibration	142
A.2.2	Interpolation of Energy Points	143
B	Publications	147
B.1	Peer-Reviewed Articles	147
B.2	Internal Reports	148
B.3	Conference Proceedings	149
	Bibliography	151
	Acronyms	159

List of Figures

2.1	Scheme of a Geiger-Müller tube.	8
2.2	Scheme of a MOSFET device.	10
2.3	Energy band structure of an activated scintillator crystal.	12
2.4	Scheme of a phoswich detector.	13
2.5	Scheme of a diode junction.	15
2.6	Different geometries of germanium crystals.	18
3.1	Energy calibration curve of one of the HPGe installed at IVM.	20
3.2	Example of a peak and two possible background approximations.	23
3.3	Different efficiency curves for germanium detectors.	25
3.4	The LLNL phantom partly disassembled.	30
3.5	Knee phantom.	30
3.6	IGOR phantom.	31
3.7	Bottle phantom.	31
3.8	Example of pile-up.	34
3.9	Example of a stylised phantom.	37
3.10	A section of the torso of the MEETMan in different resolutions.	37
3.11	Sections of the Zubal model with arms down.	38
3.12	Errors of the first and second kind.	44
4.1	Sketches of the PBC chamber.	48
4.2	Resolution of a phoswich detector in the PBC at the IVM.	49
4.3	Sketch of the WBC room at IVM.	50
4.4	Photo of an XtRa detector mounted on a temporary mechanics.	51
4.5	Simplified drawing of one XtRa detector.	52
4.6	A real filter shape, as taken from DSA-1000 software.	53
4.7	Scheme of the points used to map the detection efficiencies.	54
4.8	Initial results obtained with ISOCS or the MCNPX model.	56
4.9	Effects of the aluminium density on the ^{137}Cs detection efficiency.	58
4.10	Results after the parametric study.	58
4.11	The system used to perform scan of the detector.	60

4.12	The millimetre paper used to track the movement of the rail.	60
4.13	Scheme of the elements found during the lateral scans.	61
4.14	Curves resulting from the lateral scans.	61
4.15	Different models of the corners of the detector case.	61
4.16	FWHM of a detector as function of different flat top values.	63
4.17	FWHM of a detector as function of different rise time values.	63
4.18	FWHM of the different detectors after the optimisation.	64
4.19	Radiography obtained with 125 keV, 1.2 mAs exposure.	65
4.20	The configuration used for the measurement of the subject.	66
4.21	View of the inners of the head phantom used for the calibration.	68
4.22	Configuration used for the P4 phantom.	69
4.23	Results of the intercomparison exercise.	70
4.24	The phantom and the detector used for the experiment.	72
4.25	MCNPX geometry used to validate a liver measurement.	72
4.26	Agreement between simulations and measurements for different counting positions around the reference liver configuration.	73
4.27	Ratio channel-by-channel simulation over measurement.	74
5.1	Sitting configuration of the MEETMan phantom, first revision.	78
5.2	Sitting configuration of the MEETMan phantom, second revision.	78
5.3	Iso-surfaces from bone sources, sitting configuration.	81
5.4	Iso-surfaces from bone sources, stretched configuration.	81
5.5	Set-up for bones measurements, sitting configuration.	83
5.6	Set-up for bones measurements, stretched configuration.	83
5.7	Iso-flux surfaces obtained for a ^{241}Am source in liver.	84
5.8	Arrangement of the detectors for liver measurements.	84
5.9	Iso-flux surfaces obtained for a ^{241}Am source in lungs.	86
5.10	Arrangement of the detectors for lungs measurements, detail.	86
5.11	Space occupied by a minimal system in the WBC room.	90
5.12	Space occupied by a minimal system in the PBC room	91
5.13	The alternatives for the choice of the stretcher/chair.	93
5.14	Drawing of the Cosmoderm Veda wellness stretcher.	93
5.15	Configurations for measurements of the skull.	94
5.16	Configurations for measurements of the liver.	94
5.17	Configurations for measurements of the lungs.	94
5.18	Sketch of a subject with dimensions used in table 5.4.	95
5.19	Drawing of the new PBC/WBC chamber.	96
5.20	Scheme of the support for the detectors hanging from the ceiling.	97
5.21	Scheme and photo of the portal during a measurement.	97
5.22	Detector mounted on a hub in its final configuration.	99
5.23	Final system, ready for measurements.	99

5.24	Phantoms MEETMan, Godwin, Klara in reclined set-up.	100
5.25	Integrated and normalised distribution of the NSD values in the volumes of the mesh tally.	103
5.26	Normalised distribution of the NSD values when a 1460 keV source is located in different organs.	104
5.27	Iso-flux surfaces for the 364 keV energy line emitted by ^{131}I in the thyroid.	106
5.28	Iso-flux surfaces and region of space defined by $NSD \leq 20\%$ when the sources are placed in liver, lungs, GIT.	108
5.29	Surfaces corresponding to different values of C for 60 keV sources located in lungs, liver, GIT.	108
5.30	Surfaces corresponding to different values of C for 1460 keV sources located in the whole body.	109
5.31	Position of the detectors for the first and second iterations and surfaces corresponding to different values of NSD for 1460 keV sources in the whole-body.	110
5.32	Regions of space with defined NSD and iso-flux surfaces for 1460 keV whole-body sources.	110
5.33	Final configuration of the detectors for WBC measurements.	112
5.34	Configuration used for the calibration of the system for lung measurements.	112
5.35	Transmission factors for sources in lungs.	114
6.1	Main interface of the new software.	120
6.2	Efficiency calibration with the new software.	121
6.3	Energy calibration with the new software.	123
6.4	Photos of the ^{210}Pb measurements.	125
6.5	Spectra from the two measurements.	127
6.6	Calibration curves obtained for the three detectors used for the measurement of the skull.	128
6.7	IGOR P6 in sitting and reclined configuration.	130
6.8	Detectors in the final WBC configuration.	132
6.9	Detectors in the final WBC configuration, panorama.	132
6.10	Controller used to position the detectors.	133
6.11	Efficiencies calculated for the IGOR P4 phantom.	134
6.12	Efficiencies calculated for the IGOR P5 phantom.	134
6.13	Efficiencies calculated for the IGOR P6 phantom.	134
A.1	Structure of the database.	140
A.2	Diagram of the interpolations performed during the calibration.	144

List of Tables

3.1	List of commonly used sources.	20
3.2	Pros and cons of human model types.	39
4.1	List of the main specifications of one XtRa detector.	52
4.2	Summary of the measured crystal dimensions.	59
4.3	Results of the measurement of a subject contaminated with ^{241}Am	67
4.4	Results of the intercomparison exercise 2008 with phantom P4.	70
4.5	Ratio simulation over measurement for different energy regions of the spectrum.	73
5.1	Simulated MDA values attainable for measurements of the skull with different detector arrangements.	87
5.2	Simulated MDA values attainable for measurements of the liver with different detector arrangements.	88
5.3	Simulated MDA values attainable for measurements of the lungs with different detector arrangements.	89
5.4	Characteristic sizes of subjects, as taken from Tilley (2002).	95
5.5	Degrees of freedom of the detectors, referred to figure 5.18.	95
5.6	Transmission factors measured with the final system.	113
5.7	MDA values for two different nuclides dispersed in the lungs.	115
6.1	Results of the measurements.	126
6.2	Compton producing peaks.	129
6.3	Nuclides and corresponding activities for the different phantoms.	135

Chapter 1

Introduction

The use of radioactive sources is nowadays common in many different fields of the industry (see EPA): manufacturing (e.g. measurement of material thickness, non-destructive analysis of metallic objects, measurement of erosion and wear), food and chemistry (e.g. measurement of densities and of level of filling of containers), but also in agriculture and consumer products, just to cite some. In addition to these relatively new applications, the more traditional ones are still performed: processing of nuclear fuel, decommissioning of power plants and treatment of contaminated materials. These activities pose however a radiological risk for the workers involved, who must be therefore routinely monitored for incorporation of radionuclides. In addition to people routinely exposed, some people are also chronically exposed to high concentrations of radon in the air and a method to detect its decay product (^{210}Pb) deposited in the body would be useful to assess previous exposure.

1.1 In-Vivo Measurements of Radionuclides in Man

Two main classes of bioassay techniques are available for the detection of radionuclides in man: direct methods and indirect methods. The former class consists of whole-body and partial-body measurements, able to detect the radiation (X- and gamma-rays) emitted during the radioactive decays; the

difference between whole-body and partial-body is the configuration of the detectors around the subject: able to attain a detection efficiency independent from the position of the source for the whole-body case, able to reach the highest possible efficiency for sources localised in a specific region of the body for the partial-body case. Indirect measurements are different in that they use formulas to correlate the activity measured in the excretions with the activity retained inside the body.

The suitability of the different methods depends on the nuclides involved and more specifically on the decay modes, since direct techniques require the particles to travel through biological tissues before being detected. Radionuclides emitting gammas of high-energy and/or with high probabilities are best detected directly, while nuclides not emitting gammas or presenting only low probability lines are best suited to indirect measurements: the sample are prepared for the measurement (for example by dissolving them in a sensitive medium) and the detection efficiency is greatly increased.

Three radionuclides can be used as example: ^{210}Po , ^{137}Cs and ^{241}Am . The first one presents high-energy gammas (803 keV) that could easily escape the body and be collected, but the emission probability is too low ($1.2 \cdot 10^{-5}$ per decay) and only high activities would be detected reliably. As consequence, the measurement of excretions is the only choice in this case, being the nuclide also an alpha emitter. Another high-energy gamma emitter but with an high emission probability is ^{137}Cs (main line at 661.6 keV with probability of 0.8499) and it is consequently detected directly. The last example, ^{241}Am , is both alpha emitter and low-energy gamma emitter (main line at 59.54 keV with probability of 0.359) and it could be detected with both methods. Emission energy and probabilities are taken from DDEP.

The International Commission on Radiological Protection (later referenced as “ICRP”) published a report (ICRP78) with an overview of the different radionuclides, their biokinetic behaviour for the different incorporation paths and guidelines concerning the frequency and best method for routine measurements.

1.2 History and State of the Art

The first example of indirect measurement of radionuclides in man dates back to the 1915, when Seil, Viol and Gordon injected radium in volunteers and measured the activity in the excretions to calculate the retention (see Soil et al., 1915). The first direct measurement was performed ten years later by Hoffman, with the aid of an uncalibrated electrometer (see Martland et al., 1925), and in 1929 the first calibrated measurement was performed by Schlundt.

The use of ionisation chambers started in 1947 and allowed for an increase in detection efficiency, further increased in 1955 by the introduction of scintillation crystals (sodium iodide). This kind of detectors is still used today thanks to its low cost and to the attainable size of the crystal, for example 20 cm diameter. The latest generation of detectors is represented by germanium crystals, a semiconductor able to convert the radiation in current pulses directly measurable after amplification but without further intermediate instruments (scintillators require photomultipliers). The biggest germanium crystals are still significantly smaller than other inorganic crystals (e.g. NaI), but the significant increase in resolution (about 2% of the incoming energy, as opposed to about 8-10% of sodium iodides) compensates by making the identification of single lines possible. Complex contamination patterns and a better isolation of the contamination from the background contribution is now possible. For a more detailed discussion of the different radiation detectors see chapter 2.

Calibration techniques are required to relate the values measured with the instruments to the actual amount of radionuclides in the body of the subjects. In the beginning simple water-filled phantoms have been used, later improved to reproduce more realistically the human body: at the end of the '70s the Lawrence Livermore phantom made the reproduction of specific contaminations patterns possible (liver, lungs and other organs are interchangeable) and also reproduced accurately the behaviour of human tissues (see Kramer, 2002). Different phantoms are nowadays available for different types of measurements, see section 3.3.2 of this study for a more

detailed discussion of phantom-related issues and a list of some commonly used phantoms. Concerning the accuracy of calibration data obtained with realistic phantoms, a study was performed to compare the results of measurements performed with direct methods (in-vivo measurements and post-mortem) with the radiochemical analyses performed on the same body contaminated with ^{241}Am . The outcome is positive, showing errors within 40% for three of the four cases and within a factor of 2 for the last case (see Lynch et al., 2009).

The latest development in the field of calibration comes from the introduction in Monte Carlo simulations of realistic models of the human body (see section 3.3.3). Monte Carlo codes have been available since decades, but they have always been coupled to simplified models of the body in order to keep the computational burden low. The recent increase in computing power of computers made the use of “voxel” models (derived from “volume pixel”, see Zankl et al., 2003) possible also with desktop-class machines. These give the user a significantly higher degree of freedom in the setup of the phantom, including the ability to deform and adapt it to different body geometries without the need of manufacturing a real model. For an overview of different phantoms used for Monte Carlo simulations, see e.g. Guadrini and Ferrari, 2010.

1.3 Objective and Structure of This Work

The present thesis describes the process of the renewal of the partial-body counter installed at the Karlsruhe Institute of Technology (“KIT”). The old system, comprised four HPGe detectors and two phoswiches, has been upgraded by replacing the old germaniums with four new HPGe “XtRa” detectors from Canberra (see Canberra Industries Inc, 2010a) on a custom designed mechanics. The new system offers significant advantages over the old one: the degrees of freedom of movement of each detector are significantly increased and consequently also the possible applications of the system (i.e. whole-body measurements); the energy range from 20 keV to 2 MeV allows for the detection of low-energy emitters such as ^{210}Pb with good efficiency; the liquid nitrogen cooling is replaced with an electrical system, to simplify

the management and increase the safety of the system by avoiding leaks of nitrogen in the room.

The work is divided in chapters according to the following structure:

chapter 2 describes the different instrumentations used to detect radiation, from simple sensors able track doses to state of the art high purity germanium crystals suitable for high resolution spectroscopy;

chapter 3 describes the techniques used to analyse the spectra and how the instruments are calibrated using traditional methods or computational methods (Monte Carlo simulations);

chapter 4 describes the application of the methods previously described to the actual detectors available at KIT;

chapter 5 deals with the steps followed to design the new body counter, from the choice of the room to the calculation of the optimised measurement configurations;

chapter 6 describes the structure of the software developed to manage the detectors and the initial series of calibration measurements performed to have a system.

Chapter 2

Hardware

This chapter provides an overview of the different devices apt to detect radiation, with an emphasis on devices able to perform spectroscopy. Among them, the type of detectors used for this work, germanium detectors, are discussed in more detail.

2.1 Sensors

In the simplest approach, a radiation detector is a device able to reveal the presence of radiation, without discriminating about the radiation type and without producing any other information about its characteristics. This kind of sensors can be used to either show an instantaneous radiation flux (e.g. Geiger Müller counters, to monitor the field of a source) or to integrate radiation fluxes over time (e.g. TLD dosimeters, to provide information about doses deposited in tissues). Both devices are described in the following sections.

2.1.1 Geiger-Müller Counters

Geiger-Müller counters are devices able to detect single particles interacting with the active volume of the device, but unable to distinguish between different types of particles. They are used whenever a reading of the frequency of the pulses (as opposed to the energy of the pulses) is enough. Dose estimates

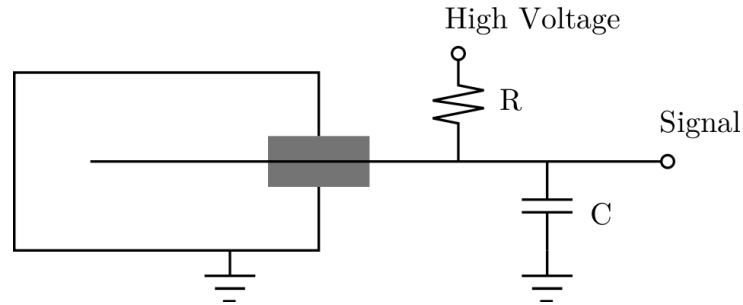


Figure 2.1: Scheme of a Geiger-Müller tube. The voltage is applied between wire and tube case and the values of R (series resistance) and C (capacitance) define the time constant of the pulse. The electronics for the quenching is not shown.

can be reported by some instruments but the value is obtained only with an assumption about the energy deposited per interaction, the value is not actually measured.

The principle of operation of this kind of device is based on the multiplication of the number of electrons freed by the radiation interacting with the active medium. The medium is a low pressure (about 10 kPa) inert gas (helium, neon, argon) kept under high voltage (over 10^5 V/m) between the tube container, acting as cathode, and a wire along the axis of the tube, acting as anode. A scheme of the device is shown in figure 2.1.

Radiation particles entering the active volume may undergo an interaction and release electrons from the gas. These would be accelerated and, thanks to the high electric field, propagate the ionisation and generate an avalanche effect. Being the electric field very high and the electrons impacting the anode at high speed, ultraviolet light produced by these interactions generates further ionisation in the gas, thus making the process exponential until the anode is completely surrounded by electrons and the intensity of the discharge independent from the initial number of ionised atoms. In order to stop the avalanche, additional electronics able to cut the high voltage is added to the circuitry or a secondary (‘quenching’) gas with a more complex atomic structure to stop the discharge is added to the active volume. In either case, the process is relatively slow and Geiger-Müller tubes are not suited to count rates exceeding the thousand impulses per second range.

Concerning the types of radiation detected by these devices, impulses are generated by particles able to penetrate the casing and to generate an interaction in the active volume. This includes photons from about 100 keV to 2 MeV (with varying degrees of efficiency), electrons over 1 MeV (or lower if the device is equipped with a thin entrance window, for example made of mica) and α -particles (only with specifically designed entrance windows). Neutrons are usually not detected, since they do not cause ionisation of the gas, but some device include a moderator to slow the neutrons and boron trifluoride gas mixed in the active medium. This compound converts the neutron into an α -particle that can be detected normally.

Being the device of easy construction, it has the advantage of a lower cost in comparison to other instruments and it can be made rugged enough to be suited to applications on the field. These devices are therefore still widely used, after more than one century from the original design, dated 1908 by Geiger and perfected twenty years later with the help of Müller (Geiger and Müller, 1928).

2.1.2 Dosimeters

Dosimeters are a class of radiation sensors that, in comparison to the Geiger-Müller counters, lose the time resolution (the ability to distinguish pulses) but gain the ability to integrate the actual deposited energy over time. They are used to monitor doses to people occupationally exposed to radiation or objects and can be of different types: badge film, quartz fibre, thermoluminescent, pellet shaped, solid state.

Badge films are one-time only use since radiation changes the properties of the medium in a non-reversible way: they are photographic emulsions sensitive to radiation. Quartz-fibre dosimeters are small ionisation chambers: they can be read visually and are reset by charging them electrostatically. Thermoluminescent devices track doses by shifting electrons to higher energy levels. The new states are metastable and can keep the information over longer times, until the device is heated up and the electrons fall back to the ground state. The process releases a light photon per event and the photons

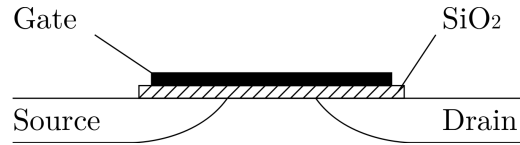


Figure 2.2: Scheme of a MOSFET device.

are counted to obtain the value of the dose: the read-out and the reset of the device happen at the same time. For example, this kind of dosimeters is used in rings for workers in the nuclear medicine department in hospitals, since the radiation exposure is sometimes localised to the extremities (see Rimpler and Barth, 2007).

Solid state dosimeters use the properties of integrated circuits technologies to produce dosimeters that can be easily read-out by simple electronic circuitry. An example is the MOSFET dosimeter (see figure 2.2), where the radiation interacts with the silicon-oxide between the gate and the silicon substrate and generates electron-hole pairs. By applying a positive bias during the exposure time, electrons and hole migrate toward respectively the gate and the silicon-SiO₂ interface and a change in the threshold gate voltage can be observed. The sensitivity of the device can be tuned by changing the bias voltage, the thickness of the silicon oxide and the number of cells per surface unit (Knoll, 2000, chap. 19).

2.2 Scintillators

Scintillator detectors are assemblies made of a scintillation material that converts incoming radiation into light, coupled to a photomultiplier tube (“PMT”) to convert the light into electrical current. This kind of detector was first discovered at the beginning of the last century, when Sir W. Crookes noticed how a zinc-sulfide (ZnS) screen reacted to α -particles (see Ryan and Poston, 2006). Scintillators found greater popularity starting from the ’50s, when pulse multiplier tubes were developed.

In a scintillator the incoming radiation excites the atoms of the medium, that will later emit photons according to three phenomenon: fluorescence,

phosphorescence and delayed fluorescence. Of the three, only the first one is of practical interest, since phosphorescence emits photons at longer wavelengths, not tuned to the photomultiplier, and, just as delayed fluorescence, at later times. Fluorescence is of interest since the emission is prompt, making the light peak short and consequently the instrument able to detect more events per unit of time. All the delayed emissions will constitute a background noise emitted after a random period of time. The light pulse is then collected by a PMT tube that converts it into an electric current, measurable after proper amplification (see Knoll, 2000, chap. 8).

Different scintillation mediums have different light decay and light emission characteristics: efficiency and linearity of the energy-to-light conversion, characteristic wavelength and decay time of the light pulse, density. In applications where an high count rate is required, a short decay time of the pulse is important: organic materials are preferable. Inorganic crystals have however higher densities and higher conversion efficiencies, therefore they can be made smaller and they attain better energy resolutions. In addition, the sharper the peaks, the better the identification of single energy lines.

One crystal often used for in-vivo applications is sodium-iodide (NaI) doped with thallium as activator (about 1% molar fraction). A dopant in the crystal matrix is required to enhance the scintillation properties: a pure crystal has a valence band (where electrons reside in their ground state) and a conduction band (the first energy level that electrons can assume when excited) with an energy gap between them too high to produce visible light, suited to photomultipliers, and in addition the scintillation process is inefficient. The addition of activators provides some additional energy bands, localised in the activation centres, with smaller bandgaps. The electrons released by the incoming radiation first travel to these centres and then recombine, producing longer wavelength light (see figure 2.3). Since the main bandgap of the crystal is higher than the energy of the released photons, the probability of their absorptions is low and the photons can reach the PMT. The crystal behaves as a transparent medium for the scintillation photons.

The conversion efficiency can be reduced by absorption of light in the sites of the activator, but this is present only in small fractions, and by radiation-less

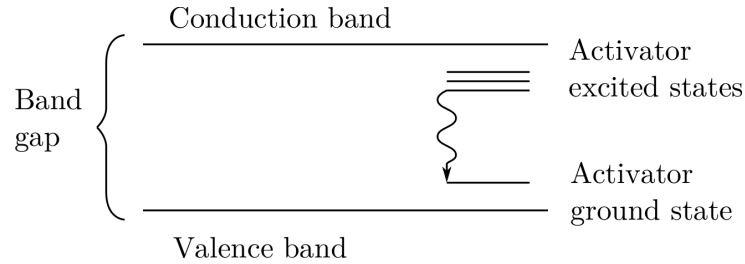


Figure 2.3: Energy band structure of an activated scintillator crystal.

transitions of the electrons to ground states (‘quenching’). As reference values, a NaI(Tl) crystal operated at room temperature has an overall light conversion efficiency of about 10^4 photons/MeV of incoming gamma radiation. Further details on the physics and characteristics of different scintillation materials are available on Knoll (2000).

2.2.1 Phoswich Detectors

A particular type of scintillator detectors are the ‘phoswich’ detectors (from ‘phosphor’ and ‘sandwich’). This class of detectors uses different scintillator crystals with different light decay properties coupled to a single PMT. The advantage of this system is the ability to produce information about the location of the interaction thanks to the different peak shape. This additional information can be then used to remove coincident events, for example Compton interactions depositing energy in both crystals: the result is a lower continuum background and therefore lower limit of detection. A paper describing the calibration and the results attainable is Manohari et al. (2010). The partial-body counter installed at KIT is equipped with two NaI(Tl)/CsI(Tl)/NaI phoswich detectors. The first layer is made of 1 millimetre thick NaI(Tl) to detect low-energy (< 80 keV) photons, while the second 5 centimetres thick CsI crystal is used to capture higher energy gammas and Compton photons originated in the first crystal. The latter layer of undoped NaI is used to shield the crystals and further lower the background of the instrument (see figure 2.4). A more detailed description of the detectors installed at KIT is available in Leone and Breustedt (2010). A downside of this type of detector is the complexity of the electronic chain required to

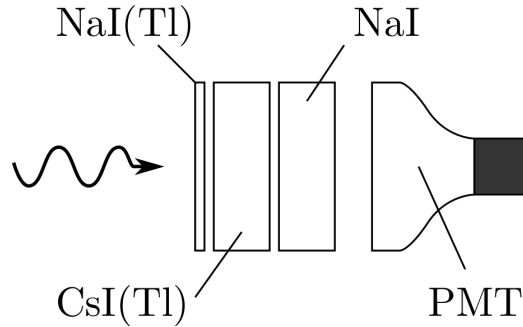


Figure 2.4: Scheme of a phoswich detector.

analyse the output signal, since additional processing steps are required to select the desired peaks in comparison to normal scintillator system.

2.3 Semiconductor Diode Detectors

One of the biggest shortcomings of scintillator detectors is the poor energy resolution, due to the long chain of events from the first interaction of the incoming particle and the acquisition of the signal. Among them, the low number of carriers originated by the interaction of the particle with the medium is the factor contributing the most to the energy resolution. In order to calculate the peak broadening originated by counting statistics, the step of the conversion with the lowest number of carriers has to be calculated, that is the excitation of the first dynode by the electrons originated in the photocathode of the PMT. The following formula (see Knoll, 2000, chap. 10) can be used to calculate such number:

$$N_e = \frac{E_\gamma}{E_g} \cdot \eta_c \cdot \eta_o \cdot \eta_{qe} \quad (2.1)$$

where

N_e is the number of electrons hitting the first dynode;

E_γ is the energy of the incoming ray;

E_g is the bandgap energy of the crystal, expressed in the same unit of measure of E_γ ;

η_c is the scintillation efficiency of the crystal;

η_o is an estimate of the other sources of photon loss (reflections, losses in the interfaces);

η_{qe} is the quantum efficiency of the photocatode of the PMT.

With typical values for a NaI(Tl) crystal ($E_g = 3$ eV, $\eta_c = 0.12$, $\eta_o = 0.75$, $\eta_{qe} = 0.2$) and an incoming ray of 500 keV, the number of electrons available for multiplication is $N_e = 3000$. If a Poisson statistics is assumed, the associated standard deviation is:

$$\sigma = \frac{1}{\sqrt{N_e}} = \frac{1}{\sqrt{3000}} \simeq 1.8\% \quad (2.2)$$

Since the peak width is expressed in full width at half maximum (“FWHM”) and $FWHM = 2.355 \cdot \sigma$, the final resolution loss is about 4.3% for this effect alone. Given the inhomogeneities of the crystal properties, of the reflection properties of the surfaces of the crystal, of the entrance window of the PMT and other sources of error, the final resolution will increase to at least 8%. As reference values, the NaI scintillators installed in the whole-body counter at KIT have a resolution of about 8%, while the phoswich detectors installed in the partial-body counter reach 15-20%. For a more detailed study concerning the sources of resolution loss and in particular the contribution of the PMT, see Mottaghian et al., 2010.

Being the number of carriers and the PMT are two major contributions to the overall energy resolution of the instrument, solid state detectors based on semiconductors were developed: the number of carriers generated in semiconductors is significantly higher than in inorganic crystals (the scintillation process and the light-to-electrons conversion are skipped) and the electrons generated by the ionisation can be collected directly at the sides of the active medium, without further intermediate steps. A downfall of the use of semiconductors is however the thermal noise generated by electrons moving to the conduction band and generating a spurious signal, whose probability is (see Knoll, 2000, chap. 11):

$$p(T) = CT^{3/2} \exp\left(-\frac{E_g}{2kT}\right) \quad (2.3)$$

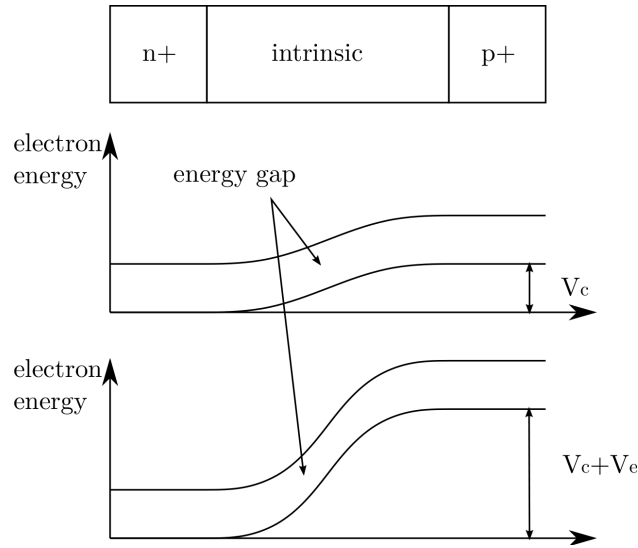


Figure 2.5: Scheme of a diode junction. V_c is the built-in potential after the creation of the n-region and of the p-region, V_e is the additional potential applied externally between n-region and p-region.

where T is the absolute temperature, E_g is the bandgap energy, k is the Boltzmann constant and C is a material-dependent proportionality constant. Cooling the crystals reduces this effect significantly.

A semiconductor detector is made of three different regions: a central ‘intrinsic’ region, where there is a balance of electrons and holes; a ‘n+’ region, where there is abundance of electrons in the conduction band, and a ‘p+’ region, where there is abundance of holes (electron vacancies) in the valence band. The n+ and p+ regions are produced by introducing impurities in the crystal, usually by drifting lithium for the n+ region and by implanting boron for the p+ region, dopants that are either donor or acceptor of electrons (they make available or reduce the availability of electrons in the crystal matrix).

The net result of this process is the creation of a diode junction: if a positive potential is applied between the p+ and the n+ regions, a current will flow from the region with abundance of holes to the region with abundance of electrons. If the voltage is applied in the reverse direction, the built-in difference of potential is enhanced and almost no current will flow. Instead, a stronger electric field will build up in the intrinsic region (see figure 2.5).

As consequence of the applied voltage, the depletion region in the middle of the junction expands, since the holes and the electrons of the p+ and n+ regions will move toward the sides. If the applied potential is high enough, the depleted region in the middle, with no free carriers, will extend to the whole crystal, with free electrons and holes completely shifted to the surfaces. This configuration is called ‘fully depleted’ and is the most favourable for the use of the device as radiation detector, since the depleted region is also the active region. Fully depleted crystals have several advantages over partially depleted ones, for example the strong electric field in the depleted region causes higher migration speed for the carriers generated by the interaction with radioactive particles, therefore improving the time properties of the instrument: the pulses are shorter and the maximum count rate is higher. At the same time, the n+ and p+ regions at the two ends of the crystal become thinner with increasing applied voltage, thus making the dead layer (insensitive to radiation) also thinner and letting lower energy particles enter the active region. The Johnson noise (see Johnson, 1928), generated by current flowing through a resistance, is also reduced with thinner contacts.

The maximum depleted thickness cannot be chosen arbitrarily, but it depends on the original purity of the crystal. Given an initial amount of impurities of p- or n-type, the additional doping/implantation must be intense enough to overcome the intrinsic material behaviour: the higher the impurities, the stronger and the thicker the implanted contacts. The effective thickness of the contacts decreases with higher reverse voltages applied to the crystal, but the upper value is fixed by the breakdown voltage. As final results, an high amount of initial impurities limit the minimum thickness of the contacts and also the maximum thickness of the depleted region.

2.3.1 Common Semiconductor Detectors

Being silicon crystals available only up few parts per million of impurities, the maximum depleted thickness is limited to few millimetres. The use is therefore limited to applications for lower energy particles or heavier ions that can be stopped within the thin layers of the crystal.

Germanium, beside being denser than silicon, can be purified to about one impurity every 10^{12} atoms (high purity germanium, “HPGe”) , therefore enabling the manufacturing of crystals with depleted region of several centimetres and different shapes. Before the refining of the manufacturing processes, an alternative solution to produce intrinsic region was the drifting of additional atoms inside the crystal, in order to compensate the behaviour of the original impurities and allow for thicker depleted regions. A species often used was lithium and the crystal would be defined as Ge(Li). The downside of the method was the strict requirement of keeping the device always cooled at 77 K, in order to avoid the loss of the lithium atoms from the crystal. Newer HPGe detectors do not suffer this problem and can be kept warm when not in use.

Modern HPGe detectors can assume different shapes, listed in figure 2.6. The performances (resolution) of semiconductor detectors depend on the shape of the crystal, since bigger crystal require more time for the charge collection process and the number of recombinations (losses of carriers inside the crystal) increases too. The estimation of the resolution cannot be performed as easily as with a scintillator, since the process does not follow a Poisson statistics (see Knoll, 2000, chap. 11) and a correction factor is required. As reference, the overall resolution in planar germanium detectors ranges from 0.15-0.25 keV for a gamma energy of 5.9 keV (^{55}Fe) to 0.4-0.6 keV at 122 keV (^{57}Co). Bigger detectors, such as coaxials, range from 0.8-1.2 keV at 122 keV incident gamma energy to 1.7-2.3 keV at 1333 keV (^{60}Co). In order to obtain the best possible performances in routine application, a detector tuned to the energy range of interest is preferable (see Genicot et al., 2003). For example, for the upgrade of the old partial-body counter installed at IVM, four HPGe detectors model XtRa (see figure 2.6) with an efficiency of at least 80% have been chosen. The useful energy range is from 10 keV to 2.5 MeV, being the detectors built around coaxial crystals with a very thin entrance window. These detectors are suited to low-energy (e.g. ^{241}Am , ^{210}Pb) as well as to high-energy emitters (^{60}Co , ^{40}K) and the energy resolution is suitable to the use in a partial-body and whole-body counter: 0.8-2.5 keV over the 20 keV to 2 MeV range.

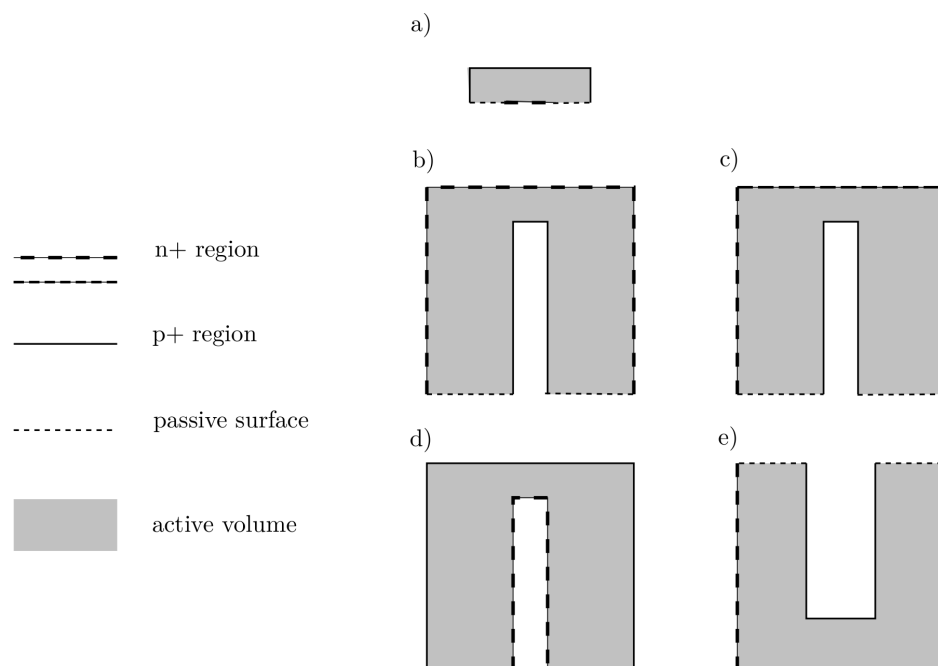


Figure 2.6: Different available geometries for germanium crystals offered by Canberra Industries Inc (2010b). Starting from the top, a) planar detector; b) coaxial detector; c) XtRa detector (a coaxial with the front contact mechanically removed, marked with a different line type); d) reversed coaxial detector; e) well detector.

Chapter 3

Metrology

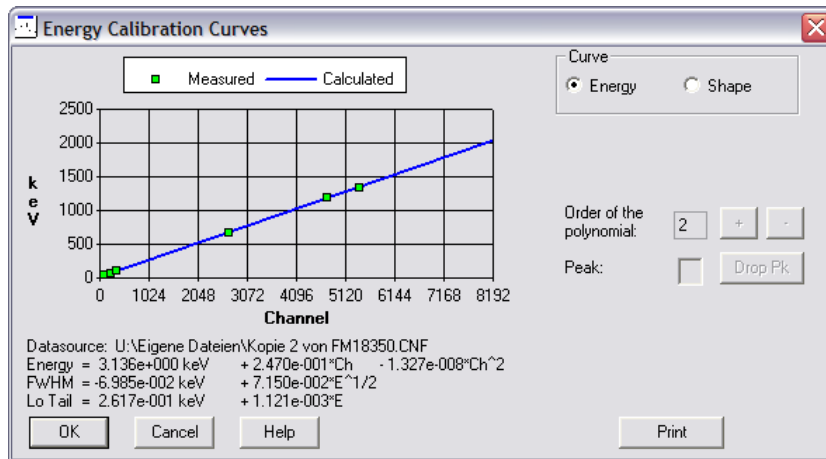
This chapter discusses the different aspects of in-vivo measurements, from the analysis of the spectrum to the calibration of the instruments for energy and efficiency and to the identification of the nuclides. In this chapter only theory concerning high-resolution spectrometry will be discussed, i.e. measurements with HPGe detectors. The order of the topics discussed follows the order of the calculations run in routine measurements.

3.1 Basic Calibrations: Energy and Shape

The energy calibration procedure associates energies to channel numbers, a step required to identify peaks and, consequently, nuclides. In order to make full use of the detector resolution and to correctly estimate shapes and areas, it is necessary theoretically to have at least three or four measurement points (channels) per peak: a Gaussian curve is defined by three parameters (amplitude, σ and coordinate of the centre or ‘centroid’), but the number of counts per channel is a statistical quantity affected by noise and additional points would reduce the uncertainties and ease the fitting of overlapping peaks. A decrease of the channel width produces however a proportional decrease of the count rate per channel and statistical fluctuations and resulting uncertainties become significant. In the case of broad-energy germanium detectors with resolution ranging from 0.7 keV at low energies (20 keV) to

Table 3.1: List of commonly used sources. All energies are taken from DDEP.

Source	Energy (keV)	Source	Energy (keV)
^{241}Am	59.5	Annihilation	511.0
^{109}Cd	88.0	^{88}Y	898.0
^{57}Co	122.0	^{60}Co	1173.2
^{212}Pb	238.6	^{22}Na	1274.6
^{203}Hg	279.2	^{60}Co	1332.5
^{131}I	364.5	^{40}K	1460.8
^{137}Cs	661.6	^{88}Y	1836.1
^{54}Mn	834.8	^{208}Tl	2614.7

**Figure 3.1:** Energy calibration curve of one of the HPGe installed at IVM. The figure is taken from the software *Genie-2K* (Canberra Industries, Inc, 2006b).

2.5 keV in the upper range of the spectrum (2-2.5 MeV), an usual channel width is 0.25 keV if count rates are expected to be small.

In order to define reference points in the spectrum, radioactive sources with well defined gamma lines are necessary (see table 3.1 for a list of some commonly used sources). The use of different sources is useful to model non-linearities of the energy response of the detector, but in case of a germanium detector the effect is very small and only few sources are required. For example, in figure 3.1 is shown the calibration curve of a new detector and the quadratic term of the energy calibration is 10^7 times smaller than the linear term: a linear calibration with two or three sources would be enough.

Another step useful to optimise the peak search algorithms and required for the calculation of the limit of detection (see sections 3.2 and 3.5) is the peak shape calibration. The goal of the process is to give the software knowledge about the resolution of the instrument and of the deviation of the measured peaks from theoretical Gaussian shape. The calibration is performed at the same time of the energy calibration and produces different parameters, for example the resolution (peak width) and the magnitude of the low-energy tail as function of incoming gamma energy.

The resolution of the instrument is approximated with a quadratic curve using the following formula:

$$FWHM = a + b\sqrt{E + cE^2} \quad (3.1)$$

where

$FWHM$ is the resolution of the instrument (FWHM), defined in keV and equivalent to 2.355 times the parameter σ of the Gaussian curve;

a is expressed in keV and is an offset value;

b is the coefficient of the second term;

E is the energy of the incoming gamma ray;

c is a correction term applied to the square of the incoming gamma energy.

The formula is written in the form used by the software MCNP/X (see section 3.3.3) but it can be used with good results also by leaving the parameter c out, as the software *Genie-2K* (Canberra Industries, Inc, 2006b) does.

3.2 Peak Search and Area Calculation

Different algorithms are available for the localisation of the peaks in the spectrum, with the second derivative method being a commonly used one. It detects peaks by selecting regions of the spectrum with an high negative curvature, suggesting the presence of the peak. The algorithm may produce false positives originated by background oscillations, therefore a threshold value is set to exclude small peaks. Additional checks can be performed by the search algorithm: for example, the software *Genie-2K* uses a modified

version of SAMPO80 (see Canberra Industries, Inc, 2006a; Markku et al., 1981) where calibration data (i.e. peak width and magnitude of the low tail as function of energy) are used to reduce the false positives.

After the identification of the candidate centroids (centres of the candidate peaks), the net area of each peak has to be calculated and the candidate discarded if the value is zero or negative. The calculation of the net area in the region of interest (“ROI”) consists in the calculation of the integral below the peak minus the local background. The local background cannot be calculated exactly, only estimated, and different methods are possible:

- linear interpolation using the number of counts measured in single regions on the two sides of the ROI;
- approximation using higher order polynomials using multiple regions defined on each side of the ROI;
- estimation using higher energy peaks and a knowledge of the Compton scattering originated by them.

The last method is practical with lower-resolution detectors and is used in the partial-body counter at KIT (see Mohr and Breustedt, 2007), but it is not of interest with high-resolution measurements, since it would require as many calculations as the number of higher energy peaks, each calculation contributing to the final uncertainty. In the case of spectra from germanium detectors, the estimation of the local background using the counts on the sides of the ROI is more straightforward and accurate.

The linear approximation is the simplest and is calculated with the following formula:

$$B = \frac{a_1 A_2 + a_2 A_1}{a_1 a_2} \frac{b}{2} \quad (3.2)$$

where

B is the local background in the ROI;

a_n are the widths of the regions used to estimate the background (left and right side);

A_n are the sum of the counts in the regions used to estimate the background;

b is the width in channels of the ROI.

In case the two regions on the sides are chosen with the same width $a = a_1 =$

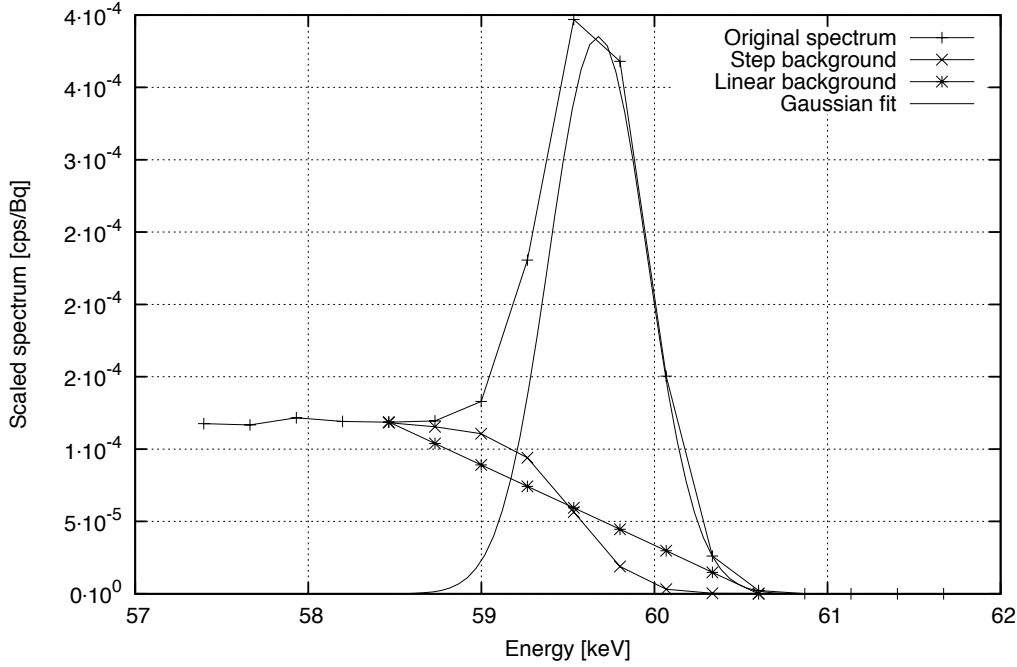


Figure 3.2: Example of a peak and two possible approximations to calculate the local background. The Gaussian fit of the peak with the background subtracted with the step formula is also provided.

a_2 , the formula simplifies to:

$$B = \frac{b}{2a} (A_1 + A_2) \quad (3.3)$$

A graphical representation of a peak generated numerically and opportunely modified to show the effects of the background on the final shape is shown in figure 3.2. Only the fit obtained after subtraction of the step background is plotted.

Peaks in the low-energy region of the spectrum may have the Compton edge falling within the ROI itself, making the average counts per channel in the two sides significantly different. Another method used to calculate the local background with more precision in this situation is the ‘step’ algorithm, implemented in *Genie-2K* (see Canberra Industries, Inc, 2006a, chap. 3) for

the case with $a = a_1 = a_2$. The formula used is the following:

$$B = \sum_{i=1}^b \left(\frac{A_1}{b} + \frac{A_2 - A_1}{a(B + N)} \sum_{j=1}^i y_j \right) \quad (3.4)$$

where

a is the width of each of the two regions used to estimate the background;

$B + N$ is the total number of counts in the ROI;

y_i is the number of counts in the channel i of the ROI.

Figure 3.2 shows also the step approximation.

3.3 Efficiency Calibration Methods

The detection efficiency is a function of the incoming gamma energy, of the position of the source relative to the detector and of the materials interposed between source and detector. The detection efficiency is required to obtain estimates of the activity contained in the subjects being measured:

$$A = \frac{N_i}{t \cdot y(E_i) \eta(E_i)} \quad (3.5)$$

where

A is the activity (supposed to be constant during the counting time) of the nuclide being considered;

N_i is the net number of counts in the ROI i , after local background subtraction;

t is the effective counting time of the measurement, obtained by the real counting time minus the dead time introduced by the counting circuitry;

$y(E_i)$ is the yield in photons of energy E_i (the energy of the centre of the peak i) per decay of the nuclide being considered;

$\eta(E_i)$ is the detection efficiency as function of E_i .

Different methods to calculate the parameter $\eta(E)$ are available: one uses actual measurements, another one uses computer simulations. Since both produce discrete efficiency values, calculated or measured for specific energy points, a method to interpolate them is required.

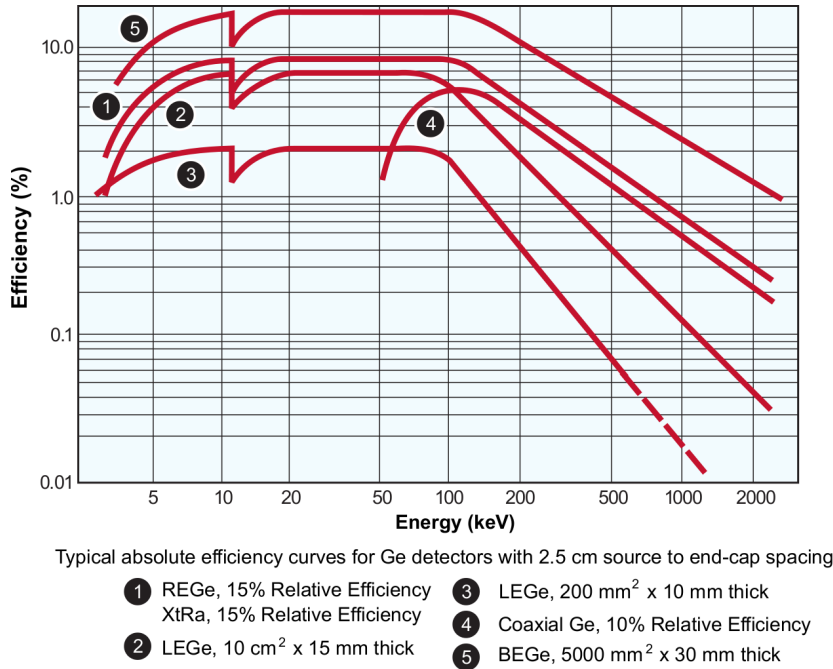


Figure 3.3: Different efficiency curves for different germanium detectors (see Canberra Industries Inc, 2010b).

3.3.1 Interpolation of the Efficiency Values

The efficiency curve for germanium detectors is not a simple decaying exponential, as a simple absorber would produce, because each detector has additional but inactive absorbers interposed between the sensitive volume and the external source: air (it plays a role at lower energies), detector casing (aluminium, beryllium or carbon epoxy just to cite the most commonly used), detector support (often made of copper but placed only on some surfaces of the crystal), dead layer (in front of the crystal for the electrical contact). In addition, some crystal shapes such as the coaxial one make the detection efficiency particularly sensitive to the direction and position of the incoming gamma rays. For example, high-energy gamma rays impinging the front side on its axis (see figure 2.6) can penetrate the first layer of material and reach the inner hole, thus producing lower number of counts than an equivalent ray impinging the crystal off-axis. Efficiency curves for some standard germanium detectors are shown in figure 3.3.

The efficiency values are obtained only for few energies: the energy lines emitted by the calibrated reference sources or the energy values input in the simulation parameters (see section 3.3.3). A method to interpolate them is required for every other peak of the spectrum. Depending on the required accuracy and on the distance between given points, two available alternatives are the linear interpolation and the dual-curve interpolation.

The linear interpolation uses different segments to approximate the efficiency curve over the whole spectrum, being the measured points the vertices of the curve. The method is accurate enough for practical uses only if the points available are in opportune quantity and appropriately spaced, in order to better reproduce the curve where it deviates more from a straight line. Efficiency curves with long flat regions are also best reproduced with a series of linear interpolations, since higher order curves would not be able to accurately model the straight segments.

The formula used models a straight line in log-log coordinates:

$$\ln \eta(E) = \sum_{i=0}^N a_i \left(\ln \frac{E}{E_{\text{ref}}} \right)^i \quad (3.6)$$

where

η is the efficiency calculated at the energy E ;

N is the order of the approximation used, 1 in this case of a linear interpolation;

a_i are the fitted parameters, different for each region of the piecewise curve;

E_{ref} is a reference energy used for the calculation of the a_i values.

A dual-curve interpolation is an approximation where the whole spectrum is divided in two regions, each of them reproduced with an higher order polynomial (usually up to the 5th degree).

$$\ln \eta(E) = \begin{cases} \sum_{i=0}^{N_a} a_i \left(\ln \frac{E}{E_{\text{ref},a}} \right)^i & \text{if } E \leq E_s, \\ \sum_{i=0}^{N_b} b_i \left(\ln \frac{E}{E_{\text{ref},b}} \right)^i & \text{if } E > E_s. \end{cases} \quad (3.7)$$

where E_s is the energy used to separate the lower-energy and the higher-energy

parts of the interpolation curve and the energy reference has been considered independently for the two ranges ($E_{\text{ref,a}}, E_{\text{ref,b}}$). All the other parameters are the same as in equation 3.6.

When only calibrated sources are available, a dual curve may be the best choice, while the linear interpolation of the values is more suited to numerical calibrations, where the user can input as many energies as desired.

3.3.2 Physical Phantoms

The goal of a phantom for in-vivo monitoring is to reproduce the behaviour of the human body when interacting with ionising radiation. As consequence, phantoms are modelled following the shape of the human body and built using ‘tissue equivalent’ materials, whose density and atomic composition closely match the values of the human tissues. For example, being the human body constituted mainly of water, soft tissues can be reproduced using polymers (plastics) such as polyethylene if a realistic behaviour is required, or even with simple plastic bottles filled with water if only high-energy photons are of interest (see the description of the physical phantoms in the following paragraphs).

Phantoms can either be physical or computational, the former being ready to be used in the counting system but expensive and available only with some radioactive sources, the latter being more customisable for the goal of each simulation, but requiring more time for the initial set-up of the simulation environment (each key component has to be validated to guarantee that also the results are valid).

The efficiency calibration with physical phantoms is performed in four steps:

1. loading of the phantom with the desired organ containing the desired nuclide;
2. placing the phantom and the detector(s) in the actual measurement configuration;
3. performing a measurement long enough to collect a suitable amount of counts in the peak(s) of interest;

4. calculating the efficiency value for selected energies using formula 3.5.

One disadvantage of the procedure is the need of an exemplar of each organ/source combination: only the most important combinations are therefore chosen. Another disadvantage of the method is the fixed physical properties of the materials: if tests with different densities or shapes of the organs are desired, a physical phantom is of little use. Some of the most commonly used phantoms are listed in the following paragraphs (for more details, see ICRU48).

LLNL Torso Phantom The Lawrence Livermore National Laboratory (“LLNL”) torso phantom is the reproduction of the torso of a human male 76 kg heavy and 177 cm tall. It was developed in the ’80s (see Griffith et al., 1986) and the In-vivo Messlabor (In-vivo monitoring laboratory, “IVM”) at KIT owns one since 1985. It contains exchangeable organs (liver and lungs loaded with radionuclides are available at KIT) made of foamed or solid polyurethane. It is suited to low-energy measurements since the different parts of the torso (ribs, bones, soft tissues) correctly model the behaviour of human tissues down to the X-ray region around 20 keV. Overlays with different material compositions are available to reproduce also the different chest wall thickness (from 12.8 mm to 35.8 mm) and the different muscle/fat ratio of the subjects. See figure 3.4 for a graphical representation.

Fission Products Phantom The fission product phantom is another anthropometric phantom suitable to low-energy measurements. It has organs with holes for pins in order to simulate not only a uniform radioactive contamination of the organs but also a localised deposition of radionuclides. The phantom includes neck and head, the complete torso and stub legs with articulated hips, in order to position the phantom also in sitting configuration.

Head Phantoms Different anthropomorphic head phantoms are available. The IVM at KIT owns three of them: one loaded with ^{210}Pb on the inner surface of the cranial bone and one loaded on the outer surface of the cranial bone. An additional phantom loaded with ^{241}Am on the inner skull surface is

available. The phantoms with ^{210}Pb use wax to simulate soft tissues, while the phantom loaded with ^{241}Am uses foamed polymers (see Schwabenland, 2010).

Knee Phantom This phantom is the reproduction of the middle part of the leg of a man. The bones are interchangeable and it is used with bone-seeking nuclides such as ^{241}Am and ^{210}Pb . The phantom is shown in figure 3.5.

IGOR Phantom The IGOR phantom is sometimes referred as ‘Olga’ or ‘Irina’ phantom (see IGOR; Kovtun et al., 2000) and is made of polyethylene cuboids with holes for the placement of radioactive rods. This phantom reproduces only the middle- and high-energy scattering properties of the body and is used for example with ^{133}Ba , ^{137}Cs , ^{60}Co , ^{40}K . The cuboids can be arranged in different configurations to simulate different body sizes, from 10.6 kg to 95.2 kg. For a graphical representation, see figure 3.6.

Bottle Phantom This phantom was proposed by Prof. Dr. Schmier¹ and is built using 1 litre and 2 litre polyethylene bottles filled with a radioactive solution. The bottles can be arranged in different configurations to simulate different body sizes. The IVM at KIT uses a phantom with a ^{40}K solution, but the phantom is suited also to other high-energy emitters such as ^{137}Cs or ^{60}Co . The phantom in its 70 kg configuration is shown in figure 3.7.

3.3.3 Monte Carlo Simulations

Monte Carlo (“MC”) codes for radiation transport are a class of software able to reproduce the physics of the interactions of radiation with matter to obtain, for example, calibration data without the need of performing real measurements. An advantage of such codes is the time required to produce the results: given the significant increase in computing power of the last years, simulations can be performed faster than real measurements, especially if the source used in the measurements is not very intense.

¹Unfortunately, no official publication is available on the topic.



Figure 3.4: The LLNL phantom partly disassembled.

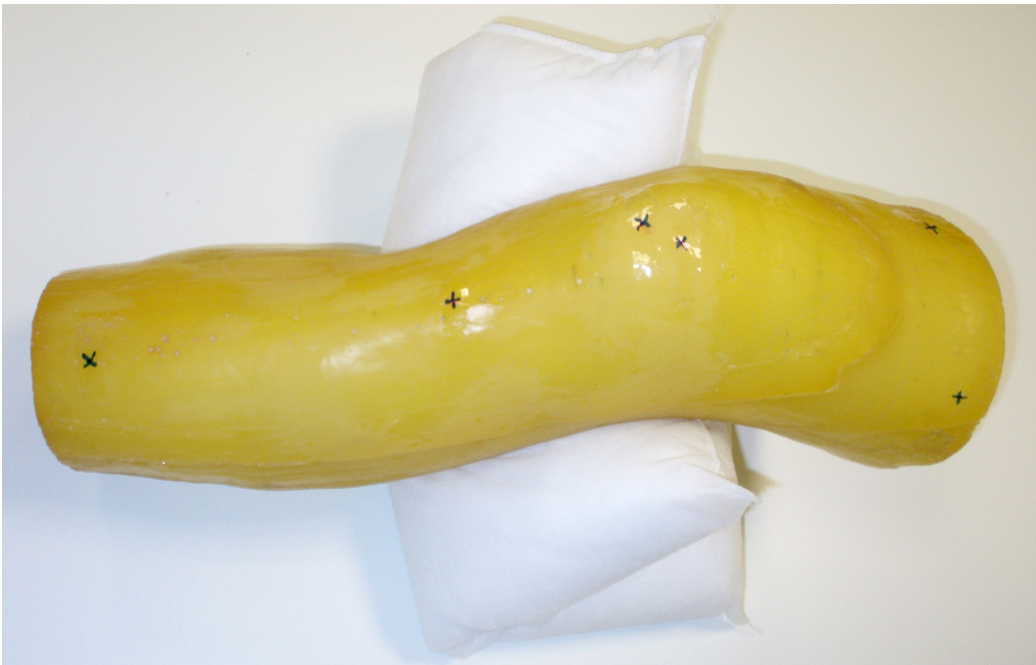


Figure 3.5: Knee phantom during a measurement in the PBC chamber at IVM.



Figure 3.6: IGOR phantom built in the 70 kg configuration in the WBC room at IVM.



Figure 3.7: Bottle phantom built in the WBC room at IVM with the bottle of the neck replaced by a cylinder loaded with iodine for the intercomparison exercise of 2009.

Different MC codes are available for the purpose, the most commonly used being MCNP5/X (Pelowitz, 2005; X-5 Monte Carlo Team, 2008), EGS4/nrc (Kawrakow et al., 2003; Nelson and Rogers, 1985), PENELOPE (Salvat et al., 2006) and Geant4 (Allison et al., 2006). Among them, MCNPX has the simplest language for the definition of geometries, therefore it was chosen for this study. Different MCNPX versions (2.5.0, 2.6.0, 2.7 beta) have been used to perform the simulations of this study, but a standard set of tests was performed after each upgrade to ensure the quality of the results.

The most important part in a simulation is, from the user perspective, the collection of the results. MCNPX uses ‘tallies’ of different kinds to extract useful data from the Monte Carlo engine. Among them the F8 tally is the most useful when simulating HPGe detectors, since it outputs the energy deposited in user-defined regions of space (typically the germanium crystal) and can produce realistic spectra by using energy bins and by broadening the spectra according to user defined parameters. To obtain the energy deposited, the MC code emits one particle (photon or electron) at a time from the defined source and follows its life and the life of its daughters (secondary electrons and photons) until either the complete absorption, the decrease of the particle energy below a threshold or the exit of the particle from the specified geometry. Every time a particle enters or exits the volume of interest, the energy of the particle is tracked and the tally records the difference between the values at the entrance and at the exit.

An important feature of the F8 tally is the ability to simulate multi-channel analysers to obtain spectra theoretically comparable to the measured ones. The user has only to choose the spectrum energy limits and the number of channels to obtain uniformly spaced bins. It is theoretically possible to simulate non uniform bin widths by specifying the width of each of them, but, as previously shown, typical HPGe do not require such precision (see figure 3.1). Another useful feature of the F8 tally is the ‘Gaussian energy broadening’ parameter, used to simulate the peak broadening experienced in real detectors. The formula used for the broadening has been already cited in equation 3.1. Applying the broadening directly during the MC simulation is useful when the parameter are already known with good precision, but it

makes impossible to change them at a later time. A Microsoft Excel (see Microsoft Corporation, 2011) macro has been developed and used to apply different broadening values to unbroadened spectra.

As already briefly mentioned, MNCPX and many other MC codes simulate one particle at time, from its generation to the complete absorption of all daughters. The results of the simulations can be compared to real spectra only under the assumption that interactions in a real detector happen in the same way, one particle at time. This is not true, since the time required by the detector to collect the charge freed by a first interaction may be longer than the time between two interactions, resulting in a summing effect (usually called ‘pile-up’) where the energy collected in a single electrical impulse has been originated by multiple incoming photons. To describe the source of the issue with different words, MC codes are only able to simulate infinitely fast detectors.

The observed effect of pile-up on the spectra is both the generation of new non-existent peaks in correspondence to the sum of the energies of the most prominent ones, if the two photons are closely spaced in time, and a uniform increase of the continuum background, if the time difference between the arrival of the photons increases and the summation is partial. Figure 3.8 shows an example. The magnitude of the discrepancies can however be approximately calculated and taken into account. The value can also be used to choose radioactive sources of proper intensity to obtain efficiency calibrations free from pile-up. The calculation of the discrepancies as function of count rate follows.

The decay of a radioactive species follows the Poisson distribution, expressed as:

$$f(k; \lambda) = \frac{\lambda^k e^{-\lambda}}{k!} \quad (3.8)$$

where

λ is the expected number of true events during the given time interval;

k is the desired number of events in the same time interval used for λ ;

$f(k; \lambda)$ is the probability to record k events in the time interval.

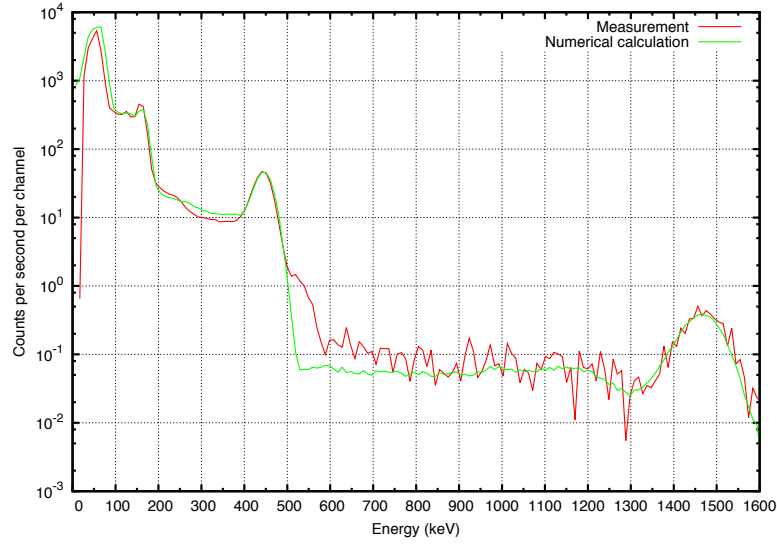


Figure 3.8: Spectrum presenting pile-up due to high counting rate from a ^{201}Tl and ^{202}Tl contamination in a subject. The pile-up in the region at 500-600 keV is originated by the gamma line at 440 keV plus X-rays of 70-80 keV. Spectrum obtained in the WBC at IVM.

The probability to experience a time interval free of pulses is:

$$f(0; \lambda) = e^{-\lambda} = e^{-nt} \quad (3.9)$$

where

n is the rate of real events per second;

t is the time required to acquire an impulse expressed in seconds.

The resulting rate of pile-up impulses is:

$$r_{pu} = m(1 - e^{-nt}) \quad (3.10)$$

where

r_{pu} is the rate of impulses affected by pile-up;

m is the rate of recorded events.

As first approximation for low counting rates, $e^{-nt} \approx 1 - nt$ and $m \approx n(1 - nt)$

where n is the rate of real events, resulting in:

$$r_{pu} \approx n(1 - nt)nt \approx n^2t \quad (3.11)$$

The rate of pile-up events is therefore proportional to the dead time of the instrument (5-10 μ s for germanium detectors) and to the square of the count rate (see Knoll, 2000, chap. 17).

Concerning WBC and PBC measurements, pile-up is usually not of interest because the expected count rate is low, resulting in a dead time lower than 1%. The issue of pile-up may appear only during calibrations with strong sources and it has to be avoided in order to produce correct calibration data.

MC simulations replicate – statistically – the interactions of particles with matter, therefore the resulting spectra should show the same statistical counting fluctuations recorded in spectra obtained with real measurements, as long as

$$n_p(E) = n_{MC}(E) \quad (3.12)$$

where

$n_p(E)$ is the number of particles emitted from the source with energy E ;

$n_{MC}(E)$ is the number of particles simulated with initial energy E .

As reference, a simulation with a 3 GHz desktop computer can track over 20 000 source particles per second, being therefore equivalent to a real source in the 10^4 Bq range, depending on the total emission probability of the selected nuclide. MC codes can be however run in parallel using multiple processors, meaning that a normal computer can often be faster than real measurements. In addition, MC codes often use techniques to reduce the variance of the results and improve the quality of the results while keeping the number of source particles constant (e.g. Kawrakow and Fippel, 2000; X-5 Monte Carlo Team, 2008).

3.3.4 Numerical Phantoms

Numerical phantoms are models of the human body, or of its parts, suited to the use with MC codes. They are defined using different methods (e.g. math-

emational surfaces, voxel volumes) and they represent human shapes with different degrees of realism. Since the definition of individual phantoms down to the internal organs is a process still too complex for routine measurements, numerical phantoms are built around ‘reference’ humans, just like physical phantoms.

The different classes of numerical phantoms are now discussed.

Stylised or Mathematical Models Mathematical models approximate the human body by using basic geometric shapes, such as spheres, boxes, ellipsoids, and cylinders. Actual volumes (organs) are defined as boolean intersections of the surfaces defined in the geometry and the control over the size and weight of each of them is exerted by modifying the parameters of each surface.

This class of models has the simplicity as primary advantage, meaning that calculations are fast and the memory requirements modest. These advantages were of particular importance in the past when these models were developed (see Snyder et al., 1969), but nowadays they are no more of primary concern: the approximation of the shapes is rough (see figure 3.9) and more realistic models are preferred. Some models are however still being refined (Akkurt and Eckerman, 2007).

Voxel Models Voxel models use a different approach to reproduce the shape of the human body: instead of surfaces defined by equations, all volumes are represented as sum of small cubes (the volumetric equivalent of the pixel found in images, hence “voxel”). This method replaces higher order surfaces with a set of simple planes. The memory requirements increase significantly, since a single model can have millions of volumes and hundreds of surfaces, but the resulting geometry can reproduce also small details and organs of the body. For example, a model made of $1 \times 1 \times 1 \text{ mm}^3$ voxels can model even blood vessels (see figure 3.10).

Voxel models cannot be built completely by hand, since the number of

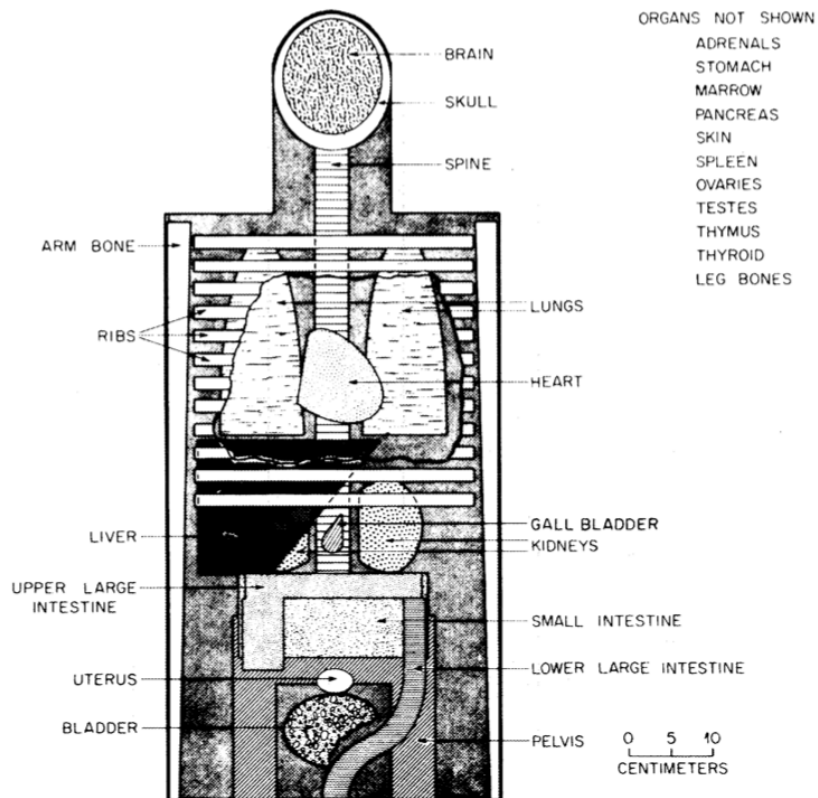


Figure 3.9: Example of a stylised phantom (Snyder et al., 1969).

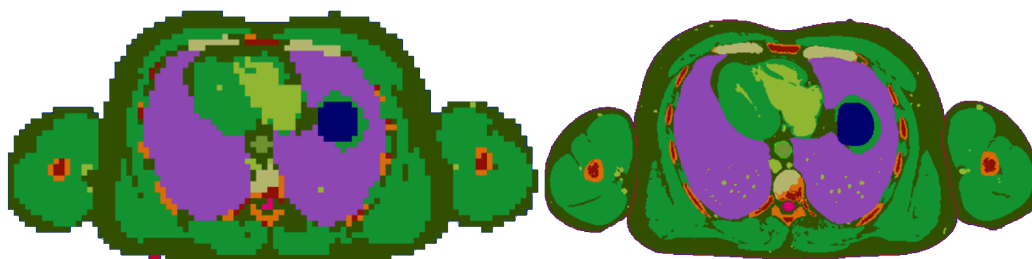


Figure 3.10: Example of a section of the torso of the MEETMan model in two different resolutions (6 mm per slice and 1 mm per slice). The second one shows a significantly higher amount of small scale structures, for example blood vessels and bronchi.

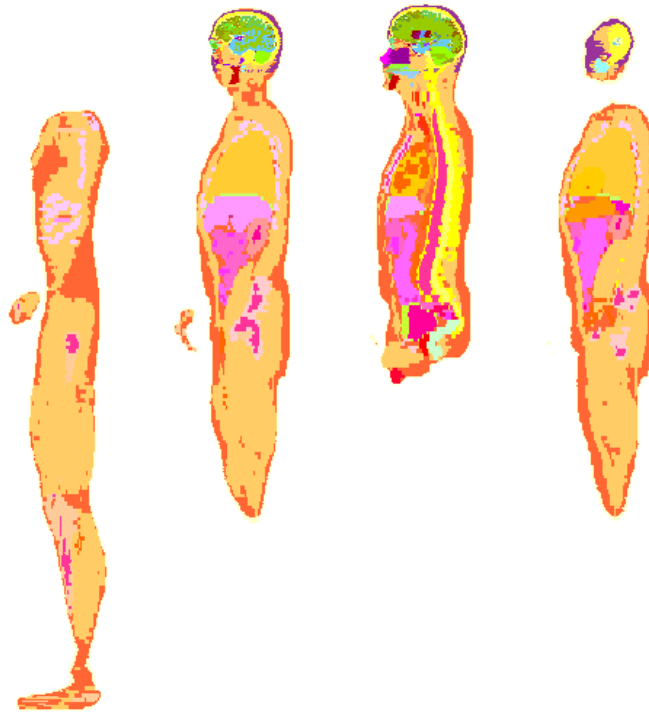


Figure 3.11: Sections of the Zubal model with arms down.

elements is usually over one thousand, hence the use of CT² or MRT³ data from real subjects as starting point. These data can be modified to alter the size and shape of the different organs (see ICRP110), or simply segmented to isolate the different materials and organs, procedure used to produce voxel models of physical phantoms (see Schwabenland, 2010). Modifications of the voxel models are possible by using graphical tools that represent different materials with different colours of an image, one slice at time.

Different voxel phantoms are available at KIT: some are generated from MRT scans of the physical phantoms available at KIT (Hegenbart et al., 2009; Schwabenland, 2010); MEETMan, a model based on the Visible Man Dataset (Sachse et al., 2000) in resolutions from 1 mm ($3.79 \cdot 10^8$ voxels) to 6 mm ($1.7 \cdot 10^6$ voxels); a model of the Zubal phantom (Zubal, 2009), shown in figure 3.11).

²Computer tomography

³Magnetic resonance tomography

Table 3.2: Pros and cons of human model types for radiation transport problems.

Parameter	Stylised model	Voxel model	BREP model
modifiability	good	poor	good
realistic anatomy	poor	good	variable
memory consumption	low	high	high

Adapting the size of a voxel phantom to the measures of a subject can be difficult and time consuming, especially if the relative size of the organs has to be changed (most notably, the thickness of the fat layer under the skin).

Boundary Representative (“BREP”) Models This class of models uses surfaces defined with different methods (e.g. polygons and NURBS⁴) to give the user more freedom in the definition of the shape of the organs. This kind of surfaces uses data from CT and MRT as starting point and CAD⁵ software to post-process them. A BREP model developed by Xu et al. (2008) was used by Hegenbart et al. (2008) to study the effect of cup size over the counting efficiency for radionuclides dispersed in lungs of females.

A downside of BREP models is the need of a ‘voxelisation’ process to convert them into geometries MC codes can use. The process can be however performed at the resolution required by the specific task and by the smallest details present in the model.

A summary with advantages and disadvantages of the different numerical phantoms is shown in table 3.2.

3.3.5 Sources of Error in Efficiency Calibrations

Efficiency calibrations, both numerical and physical, are affected by different kinds of errors. These errors translate into errors in the calibration parameters and in the final estimation of the activity contained in the subject being measured.

⁴Non-Uniform Rational B-Splines

⁵Computer aided design

The first most important source of error, affecting all kinds of phantoms, is the different shape of the calibration phantom compared to the actual subject being measured. This deviation is particularly of interest and different techniques are available to lessen it. First of all, phantoms are modelled around ‘reference’ subjects, assumed to be representative of specific parts of the population. For example, a phantom for Asian workers has been developed at the Japan Atomic Energy Research Institute (“JAERI”) and the resulting counting efficiencies for natural uranium in lungs differ as much as 18% when compared to the LLNL phantom (see Kramer et al., 1998).

Apart from the structure of the phantom and size of the organs, the subjects present also different CWT. Physical phantoms, such as the LLNL phantom, provide layers of additional tissue-equivalent absorber (different equivalent muscle/fat ratios are available) to be placed on top of the chest, between detector and original phantom. This provides a correction to increase the accuracy of the calibration. It was shown, however, that the thickness reported not always corresponds to the effective thickness value (see Gün, 2010) and some correction factors should be applied.

Concerning this very issue of CWT, its value is still required to interpolate the efficiency values obtained with the absorbing layers, but the real thickness is seldom measured, since the procedure requires an ultrasonic apparatus and more time than routine measurements allow. An empirical formula has been introduced at KIT (Doerfel et al., 2006) for this purpose:

$$CWT = 4.57 \frac{M}{H} + 0.44 \quad (3.13)$$

where

CWT is the chest wall thickness in centimetres;

M is the mass of the subject in kilograms;

H is the height of the subject in centimetres.

The formula has been developed by Fry and Sumerling (1980) and Dean (1973) using ultrasound measurements of the CWT, the height and the weight of real subjects, but it remains an approximation and hence a source of errors.

Concerning the chest, the movements of the subject produce additional

discrepancies between calibration and measurement, especially of the lungs, because the chest moves due to breathing and both the distance chest-detector and the shape of the lungs change.

An issue of some physical phantoms is the lack of ^{40}K in the materials used to build the phantom. This is an advantage if the exact counting rate has to be estimated, but the calculation of the minimum detectable activity (“MDA”, see next section) becomes impossible, being it dependent on the continuum background in the ROI. Numerical phantoms are not affected by this problem since introducing a uniform distribution of ^{40}K in the model or only in parts of it (e.g. muscles, brain) is trivial. The solution to this issue, when operating with physical phantoms, is the measurement of subjects without contamination and the calculation of the MDA using the local background.

Numerical calibrations are affected by two additional problems: incomplete or inaccurate translation of the law of physics in the MC transport code and inaccuracies in the modelling of the detector. These issues arise from the different approximations assumed by the developers of the different MC codes and on the cross sections used by such codes to model the interaction of the particles. Furthermore, the codes have an high number of parameters the user can customise and this introduces additional (human) errors. The model of the detector can also be incomplete and inaccurate, resulting in discrepancies between numerical and experimental detection efficiencies. The problem is of particular importance in the region below 60 keV, where even small details like the thickness of the dead layer of the crystal and of the entrance window can affect significantly the calculated efficiencies (see Elanique et al., 2011; Hegenbart et al., 2009).

Different intercomparison exercises have been performed within Germany and internationally to check the coherence of the results of different laboratories. Some exercises verify the proper application of quality assurance routines to the measurements and the correctness of the calibration data used, other exercises check the results produced by different MC codes and the importance of human errors in their interpretation (see Gómez-Ros et al., 2008). The IVM at KIT takes part routinely with success to such exercises, one of the steps required to keep the certification of quality.

3.4 Nuclide Identification

The identification of radionuclides in high-resolution spectra is not trivial, since there is a potentially high number of lines and nuclides to consider. In addition, unless the efficiency calibration is perfectly tuned to the sample and to the position of the sources in the sample (a condition rarely satisfied) the relative intensity of the lines will not match their emission probabilities, thus introducing uncertainties.

A method based on an iterative search of the best matches is not suitable to cases where many lines are involved, so the SAMPO80 algorithm was developed. It uses different steps to evaluate the lines found in the spectrum, to select the potentially matching nuclides and to take into account interferences between different nuclides. The algorithm would require an extensive discussion and will not be described in detail down to the equations used, only the main steps are explained. The complete description of the original algorithm can be found in Markku et al. (1981) and the modified version used in *Genie-2K* is described in Canberra Industries, Inc (2006a).

The first step performed by the software consists in selecting from a user-defined library all nuclides that present an emission line compatible with a peak found in the spectrum. An user-defined energy tolerance is used for this step, typically 1 keV for a correctly calibrated detector. Each nuclide is associated to a weight that is reduced according to the discrepancies between energy lines listed in the library and corresponding peaks found in the spectrum. The MDA (see next section) can also be taken into account to exclude from the calculation of the weights all the peaks that are not expected to be detectable. The weights are later corrected for the half-life of the radionuclide, to remove those that are expected to be decayed significantly from the time of the sample collection to the time of the measurement. The weight is finally compared with a user-defined threshold and discarded if necessary.

The first phase produces an identification matrix with the activities of each peak calculated independently for each compatible nuclide. These values are corrected for different factors such as the build-up of activity during the

exposition of filters and then the results are passed to a final correction step. The goal of this final step is the correct allocation of activity to different nuclides having common energy lines ('interfering nuclides'). A weighted mean of the activities of the different nuclides is used for this goal.

3.5 Limits of detection

The limits of detection are an estimation of the smallest signal that can be reliably detected (critical level, L_C) and of the smallest signal that can be reliably quantified (detection limit, L_D).

During the detection of peaks, two questions may arise: one *a posteriori*, consisting in deciding whether the detected peak is real (as opposed to being a fluctuation of the background), and one *a priori*, consisting in deciding which is the minimum signal that would represent a real quantity. Failing to discard a peak originated by a background fluctuation consists in an error of the first kind and its associated probability is α , while failing to mark a real signal as peak is defined as error of the second kind and its associated probability is β . The quantities $1 - \alpha$ and $1 - \beta$ are the confidence levels for errors of the first and second kind. These limits are shown graphically in figure 3.12, with two curves, representing the probability of detecting a signal with the intensity indicated by the abscissa when the real value is zero for case (a) and L_D for case (b). The curves show that the most probable signal read in the measurement is always the real value, but there is a probability α to detect a signal higher than L_C even in absence of a real quantity and there is a probability β of detecting a signal smaller than L_C (and therefore discard it) even if the real quantity is L_D .

The values of the critical level and of the detection limit can be calculated using different methods, for example with the one from Currie (Currie, 1968) as the software *Genie-2K* does (Canberra Industries, Inc, 2006a, chap. 3). Since the complete demonstration is available in the literature, only the final formulae are reported.

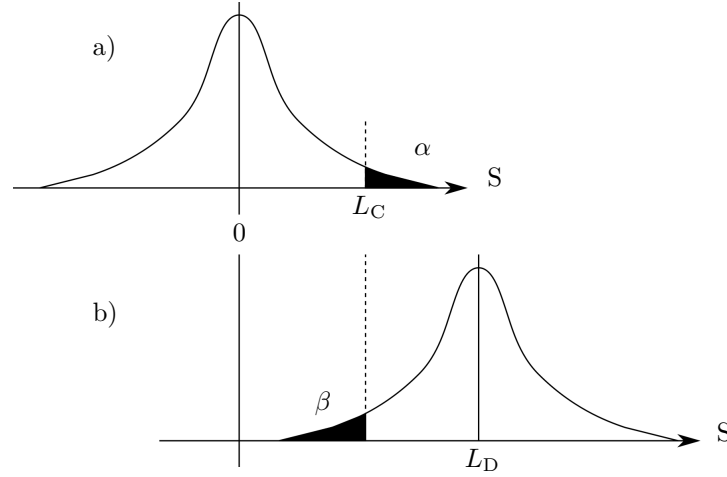


Figure 3.12: Errors of the first (a) and second (b) kind shown graphically. The probabilities to make errors are marked with black areas.

When using the Currie method, *Genie-2K* defines:

$$L_C = k_{1-\alpha}\sigma_0 \quad (3.14)$$

and

$$L_D = k_{1-\alpha}k_{1-\beta} + (k_{1-\alpha} + k_{1-\beta})\sigma_0 \quad (3.15)$$

where $k_{1-\alpha}$ and $k_{1-\beta}$ are the abscissae of the normal (Gaussian) distribution corresponding to probability levels of respectively $1 - \alpha$ and $1 - \beta$ (the confidence levels). Note that a 50% decision error would produce $L_C = L_D = 0$. The value σ_0 is the variance of the background in the region of interest and, in the case of a linear background estimation, is defined as:

$$\begin{aligned} \sigma_0 &= \sqrt{\mu_B + \mu_I + \sigma_B^2 + \sigma_I^2} \\ &= \sqrt{B + \frac{T_S}{T_B}I + \left(\frac{N}{2n}\right)^2 (B_1 + B_2) + \left(\frac{T_S}{T_B}\right)^2 \sigma_I^2} \end{aligned} \quad (3.16)$$

where

μ_B is the real value of the local background, unknown and therefore approximated with B ;

μ_I is the real value of the background interference (the area of the same

peak, measured in the background spectrum, generated therefore by the environment and not by the measured person/object), unknown and approximated with I ;

σ_B^2 is the variance of the background;

σ_I^2 is the variance of the background interference;

T_S is the live time of the sample measurement;

T_B is the live time of the background measurement;

N is the count of channels in the ROI;

n is the count of channels located on each side of the ROI and used to calculate the background;

B_i is the number of counts on each region used to calculate the background.

The equation shows that higher resolution detectors are able to attain a lower value of σ_0 , being the value N lower.

Once the L_D value has been defined, the final MDA is calculated as

$$MDA = \frac{L_D}{T_S \cdot \eta \cdot y \cdot K_d} \quad (3.17)$$

where

η is the detection efficiency for the selected energy;

y is the emission probability of the selected gamma energy;

K_d is a correction factor to take into account the decay of the radionuclide during accumulation, counting and storing time.

The latest ISO specifications in matter of limits of detection use another approach, based on Bayesian statistics. A complete discussion of the formulae used falls outside the scope of this work, for more information see ISO.

Chapter 4

Application to Existing Devices

The main topic of this chapter is the definition of MC models of the detectors chosen for this study and their validation. The different techniques used to define the different revisions of the models are described.

4.1 The Facilities and the Detectors

4.1.1 Partial Body Counter

The IVM at KIT is equipped with two counting chambers: the PBC counting room and the WBC counting room. The first one is 4.2 m long, 2.25 m wide and 2.25 m high and made of 15 cm thick steel walls, with an additional graded-Z lining on the inner surface: 3 mm lead, 1.5 mm tin, 0.5 mm copper. The chamber is equipped with a door made of the same materials. The air is filtered and continuously changed to keep the background contribution as low as possible. As result, a measurement of the residual background radiation showed a reduction of the total number of impulses by a factor of about 110 compared to a measurement performed in a normal office room.

In the PBC chamber originally three detector systems were installed: one based on four HPGe detectors and, based on two phoswich detectors (with the option to add a third one for higher efficiency) and a compact phoswich sonde to perform localised measurements. The germanium detectors consisted each one of two crystals operated in anti-coincidence mode, used liquid nitrogen

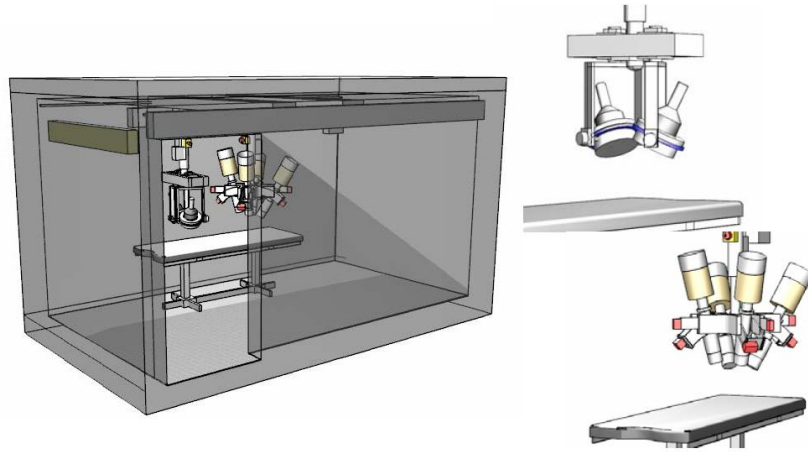


Figure 4.1: Sketches from the PBC chamber at IVM generated by data from a laser scanner. The left drawing gives an insight into the chamber with the stretcher and two detector systems. The door (in front) is not shown. The upper right drawing shows the phoswich detector pair and its rack. The lower right drawing represents the old HPGe-detector system.

for cooling and were arranged in a ring configuration, as shown in figure 4.1. This system had different limitations: the degrees of freedom of the system were limited and the handles of difficult operation, the system was used only during specific measurements when the higher resolution was preferred to the lower detection efficiency compared to the phoswiches, the use of liquid nitrogen in a closed room was potentially dangerous. The new HPGe system replaces these four detectors.

The second system shown in figure 4.1 is built around two phoswich detectors (see section 2.2.1 for a description of this kind of detector). While the diameter of the crystals (20 cm) translates into an high intrinsic efficiency, the resolution of these detectors is too coarse and makes the identification of multiple nuclides in the same spectrum difficult or impossible. Figure 4.2 shows the resolution as function of incoming energy: the curve has been obtained with different measurements, since most of the peaks used would be overlapping with each other. This system will be kept in the PBC because of the detection efficiency and used to identify the cases to be measured again with the new HPGe system.

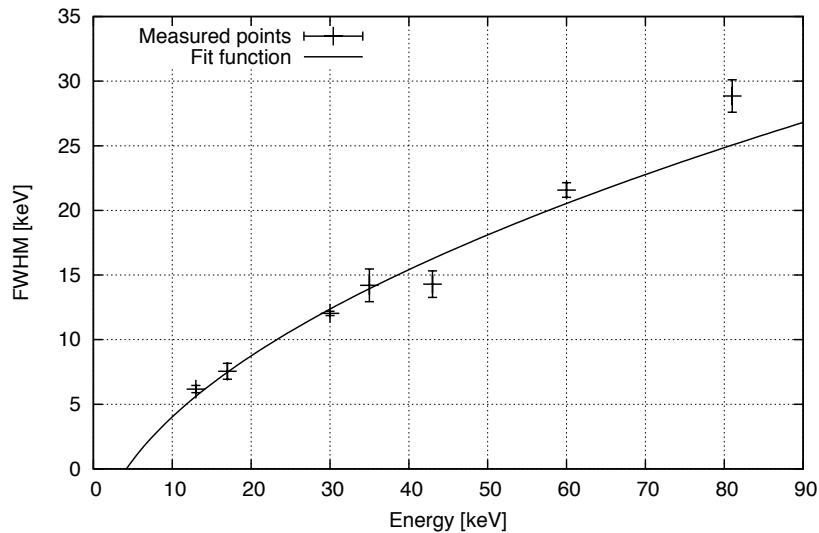


Figure 4.2: Resolution in the low-energy range of the spectrum for a phoswich detector installed in the PBC at IVM. The points have been obtained with separate measurement. As comparison, an HPGc detector has a resolution ranging from 0.5 to 2 keV.

The duration of standard PBC measurements is 2 000 s for lungs and liver and the best MDAs attainable range are 10-20 Bq ^{241}Am in lungs or liver for the standard LLNL phantom without additional overlays.

4.1.2 Whole Body Counter

The second counting room of the IVM is used for whole-body measurements and is 2.29 m long, 1.82 m wide and 2.1 m high (see figure 4.3). Instead of a door, the room is equipped with a labyrinth entrance. The walls are made of 15 cm thick steel (25 cm for the floor) lined with 0.96 cm lead. The room is equipped with scintillation detectors, more specifically four NaI(Tl) crystals 20 cm wide and 10 cm thick. The detectors are arranged in a fixed configuration able to attain a detection efficiency almost independent from the position and size of the subject: for example, a shift of the phantom of 10 cm along the head-feet axis produces an increase of efficiency by 3% (see Sessler, 2007).

Measurements in the WBC at IVM are set on a standard duration of 300 s

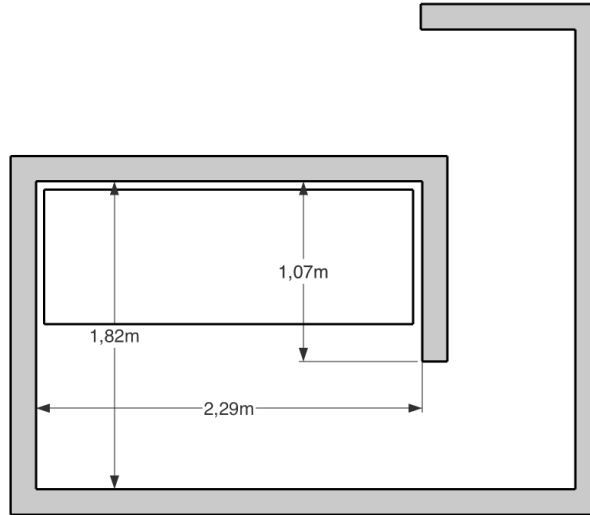


Figure 4.3: Sketch of the WBC room at IVM.

for routine and on 1800 s for reference measurements. The MDAs attainable during routine measurements for the reference 70 kg subject are 300 Bq ^{40}K , 55 Bq ^{60}Co and 59 Bq ^{137}Cs .

4.1.3 HPGe Detectors

Given the will to upgrade either the WBC or the PBC to introduce the use of HPGe detectors in whole-body measurements, a proper set of detectors had to be chosen. Among the different alternatives, the model XtRa (a p-type coaxial HPGe detector) manufactured by Canberra has been considered the most suited to the goals (see figure 4.4). The main characteristics of the detectors are:

- relative efficiency for ^{60}Co higher than 80%, to detect high-energy emitters efficiently;
- efficiency range extended to the low energies to detect low-energy emitters such as ^{241}Am (about 59.5 keV for the main emission line) or ^{210}Pb (46 keV). The XtRa detectors can be used down to 15-30 keV thanks to the thin carbon-epoxy entrance window (0.6 mm) and dead layer of the crystal (0.3-0.4 μm according to the specifications);



Figure 4.4: Photo of an Xtra detector mounted on a temporary mechanics.

- cooling with an electrical compressor instead of liquid nitrogen: the detectors are no more noiseless, but the cooling requires only electrical power to function properly. The electrical power absorbed ranges from 100 W to 160 W and there is no risk of nitrogen leak or need to refill the nitrogen tank. The electrical compressor and the vibrations produce a broadening of the peaks but this is considered in the specifications;
- resolution ranging from 1.1 keV at 122 keV to 2.1 keV at 1332 keV.

The specifications of the first detector supplied by Canberra are listed in table 4.1 and a simplified technical drawing is reported in figure 4.5.

Two optional features have been chosen for these detectors: a thin neck between detector head and compressor to be able to fit an additional shield against backscattering radiation, and a detailed characterisation in the factory of one of the detectors. The resulting data can be used with *Genie-2K* to calculate the detection efficiency for simple sample geometries.

Concerning the electronics required for the processing of the impulses, four Canberra DSA-1000 (Canberra Industries Inc, 2011) have been selected.

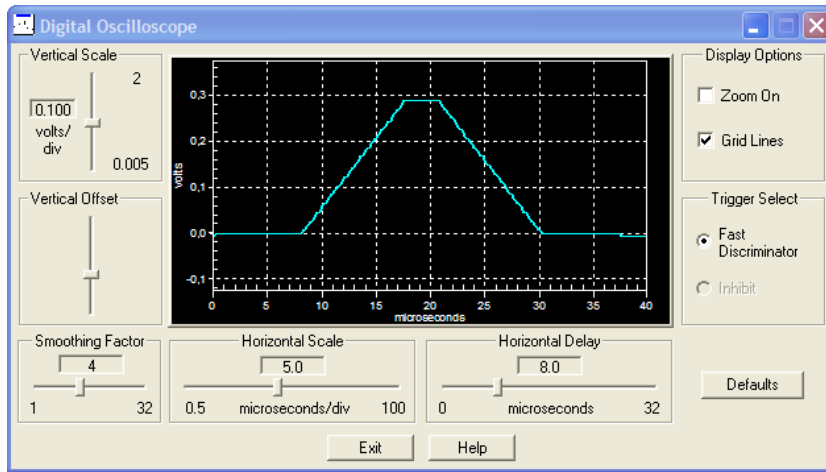


Figure 4.6: Image of a real filter shape, as taken from the digital oscilloscope included in the software of the DSA-1000 module.

These devices include in a small form factor all the circuits required to amplify, digitise and process the impulses originated in the detector. The high voltage for the operation of the crystal is also supplied by the DSA-1000 devices. The connection to the host computer is USB and all the settings are accessible from the software *Genie-2K*, no manual settings are available on the device itself. A digital oscilloscope is integrated in the circuitry to help the user correctly tune the settings. Being the device completely digital after the first amplifier, a real Gaussian shaping of the signals is not possible but it has to be approximated with a digital filter. Two parameters are available for its tuning: rise time and flat top (see figure 4.6 for a sample filter shape). The former sets symmetrically the rise time and fall time of the digital filter response and affects the noise filtering efficacy. The latter value changes the flat top part of the digital filter to match the detector charge time collection time, with bigger crystals requiring higher values. Together, they also influence the time required for the processing of the impulses and the resulting dead time of the instrument. From the lowest values to the highest, the total time for the filter ranges from $0.8 \mu\text{s}$ to $79 \mu\text{s}$ (Canberra Industries, Inc, 2005).

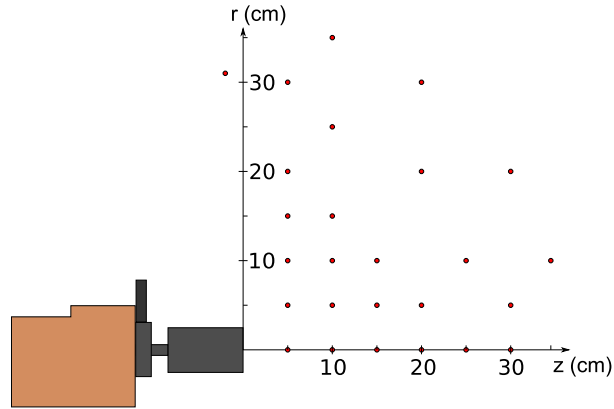


Figure 4.7: Scheme of the points used to map the experimental detection efficiencies around the detector head. The measurements have been performed only on the plane shown in the figure.

4.2 Characterisation of the Detectors

Since the calibration data from Canberra are specific to each detector and since they can be used only with a proprietary software, not suited to simulations of phantoms, an in-house characterisation has been performed for each detector and a MCNPX model has been developed and validated.

Different methods are available in the literature for the production of a virtual model of a germanium detector, but the most accurate such as the one reported by Schläger (2007) require significant amounts of human resources (about 2 years of in the case of Schläger, where only the idle time of the detectors could be used), therefore a simpler and iterative process has been preferred.

4.2.1 First Revision and Parametric Optimisation

The specifications of each detector have been used as starting point to produce a first MCNPX model. At the same time, a series of measurement with point sources (^{241}Am , ^{137}Cs , ^{60}Co) placed in an different positions in front of the detector (see figure 4.7) was used to map the real detection efficiencies.

The corners of the detector casing were mapped with more points because the external geometry of the detector (figure 4.4) was significantly different

from the technical drawing supplied by Canberra (figure 4.5) and significant discrepancies were expected.

Performing measurements in a three-dimensional matrix around the detector head would have required more than one hundred measurements, therefore a smaller series of measurements was carried out at a constant radius around the axis of the crystal, changing only the angle around it. These tests proved the good axial symmetry of the detection efficiencies and the following measurements were performed only on a vertical plane.

The results obtained from the measurements and compared with the MCNPX simulations and with the activity estimates produced with *Genie-2K* are reported in figure 4.8. Ratios lower than one indicate an overestimation of the detection efficiency. The magnitude of the errors is calculated from the combined effect of uncertainties in the positioning of the sources, in the activity of the sources and in the calibration data from ISOCS (where applicable).

The ISOCS values present a better agreement with the expected values, within uncertainties in all cases except a few with ^{241}Am . The MCNPX calibration data are more variable, showing an overall overestimation of the detection efficiencies except for some points distant from the detector. This could have been caused by positioning errors of the sources. More interesting is the systematic deviation of the expected efficiencies for the low-energy source near the detector case, with more than 15% difference in two cases. Possible causes of the deviations could be the different geometry of the aluminium corners of the case, a different dead layer thickness and a different radius of the crystal compared to the specifications.

Trying to optimise the model to obtain a better match but lacking more detailed informations about the inner structure (the manufacturer was not willing to provide more details than figure 4.5), a parametric optimisation was tested. The following parameters have been varied:

- diameter of the crystal (-10% to -5%): it affects the front surface area and therefore the efficiency at low energies (below 80 keV) but also the crystal volume and the efficiency for higher energies;
- density of the copper holder and of the aluminium casing (-20% to

- +20%, equivalent to an equal change of thickness of these materials): the change would affect the absorption of photons reaching the crystal from the sides;
- density of the crystal (−20% to +20%): this additional change has been tested since it would affect only the high energies efficiencies without affecting the photons penetrating only few millimetres before complete absorption;
 - the dead layer in front of the crystal (−33% to +200%): this would affect specifically only the very low energies, since their penetration depth is comparable to its thickness;
 - diameter of the hole within the crystal (−30% to +30%): the total volume of the crystal is affected.

Different simulations with only one change from the reference model have been performed and the results evaluated. Except for the change of the dead layer thickness, that brought no visible effects, all the other changes produced changes dependent on the energy and position of the source (see figure 4.9 for an example). Among them, the change able to best improve the overall results was a reduction of the crystal diameter by 3.5%. The change, while improving the overall results (see figure 4.10), worsened the accuracy of measurement points placed off-axis near the front of the detector surface: these cases are characterised by a significant fraction of photons reaching the crystal from the sides and the model was still unable to reproduce these interactions. Since a better modelling of the corners of the detector was not possible and since the radioactive sources used during real measurements are expected to be in front of the detector and not significantly off-axis, the change was still considered as positive and used for the subsequent simulations. A complete description of the procedure followed for this parametric optimisation is available on Marzocchi et al. (2009).

4.2.2 Scan and Improvement of the Settings

A further improvement of the model was performed later: within the frame of a ‘Studienarbeit 2’ and of a bachelor thesis, a student performed additional

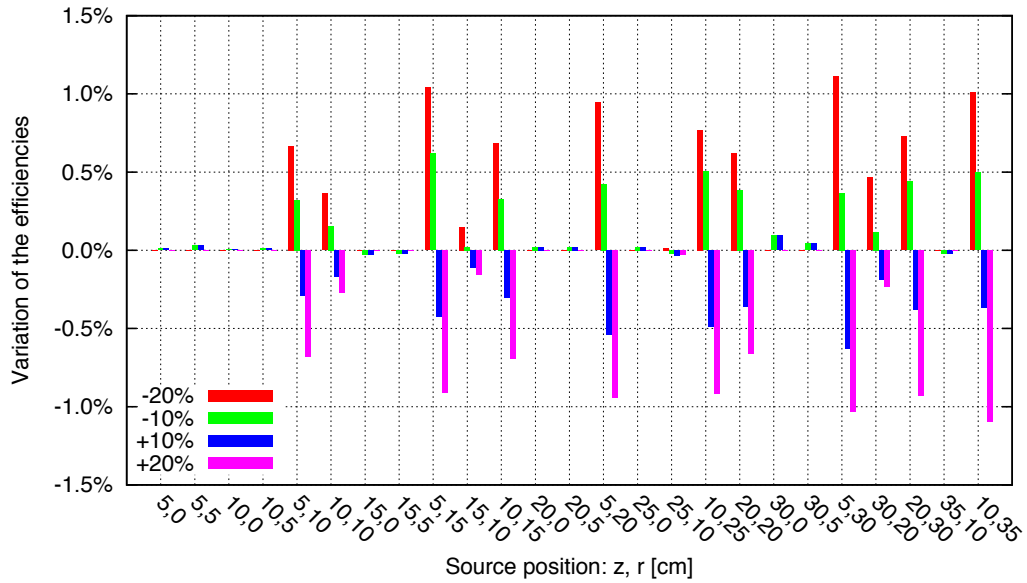


Figure 4.9: Example of the changes in efficiency obtained with a modification of the aluminium density and a ^{137}Cs source.

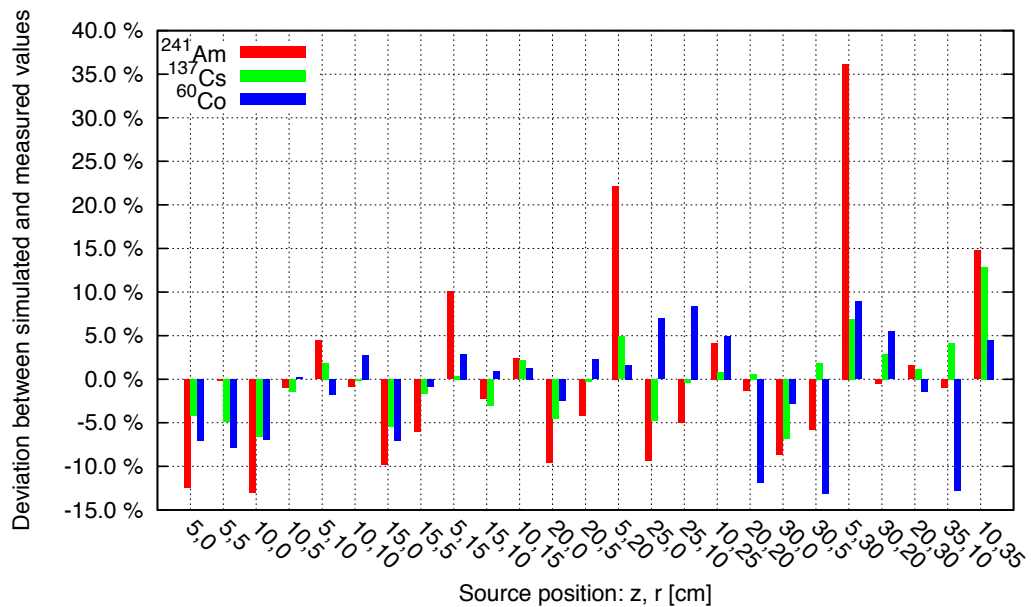


Figure 4.10: The final deviations of the activity calculated with MCNPX compared to the reference values.

Table 4.2: Summary of the crystal dimensions obtained with the different scans of the front side. Uncertainties have not been calculated by the student but can be estimated at about 2 mm.

Diameter	Detector 1	Detector 2	Detector 3	Detector 4
Expected (mm)	75	78	75	75.5
Measured (mm)	75.0	81.8	72.6	75.8
Difference (mm)	0	3.8	-2.4	0.3

measurements on different detectors, trying to improve the knowledge of the inner structure and the performances (i.e. the resolution) of the instrument. This value is of particular importance because, as already shown in equation 3.16, the limit of detection decreases for detectors with lower FWHM.

The first step of the work consisted in performing measurements with collimated sources (see figure 4.11) along the side and the front of the detectors. A rail was used to improve the precision of the movements (see figure 4.12). The count rate recorded for each measurement point is affected by the thickness of the components placed between source and crystal (see figure 4.13) and the resulting curve, plotted in figure 4.14, was used to correct the size and the position of crystal and crystal holder in the MCNPX models. As additional change, a modified corner for the casing of the detector was implemented in MCNPX (see figure 4.15). A summary of the changes applied to the sizes of the crystal is reported in table 4.2, for further data on these measurements see Gerblich (2009); Knebel and Mohr (2010).

The second part of the student's work consisted in the optimisation of the 'rise time' and 'flat top' settings for each detector. According to past experiences (see Sangster, 2007), these settings affect the shape (width) of the peaks continuously: the FWHM can be considered as a three-dimensional surface, dependent on the two settings. The surface and the coordinates of its minimum are however dependent on the energy of the photons, thus forcing the user to make choices about the energy range to optimise.

Mapping the whole three-dimensional surface was not feasible, since it would have required at least 50 measurements per detector, and an iterative

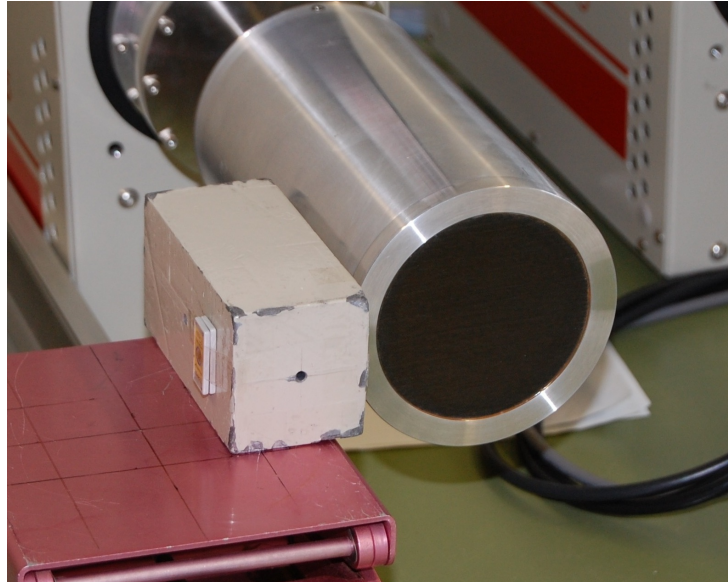


Figure 4.11: The system used to perform scan of the detector. A rail used to move accurately the source (on the table on the left of the detector) and a platform (pink) is used to accurately change the height of the collimator. The size of the collimator is $5 \times 5 \times 10$ cm and the diameter of the holes is 2 mm.

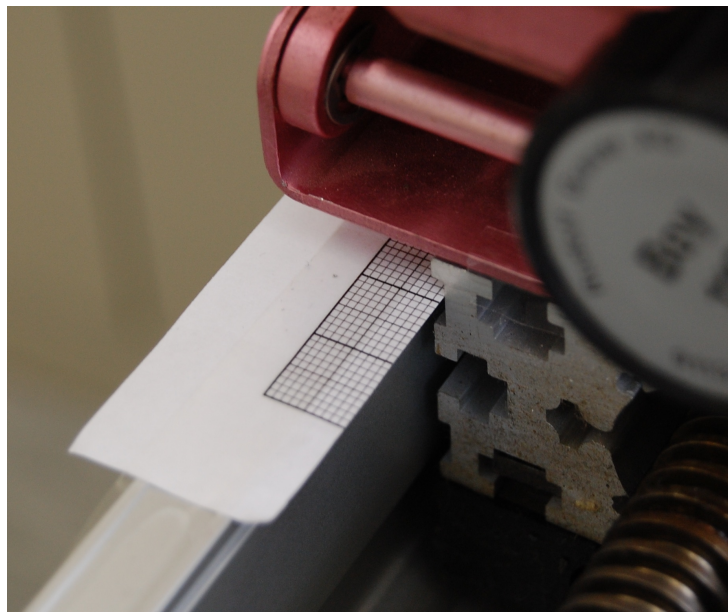


Figure 4.12: Detail of the millimetre paper used to track the movement of the rail. The precision is about one millimetre and is comparable to the degree of collimation of the source.

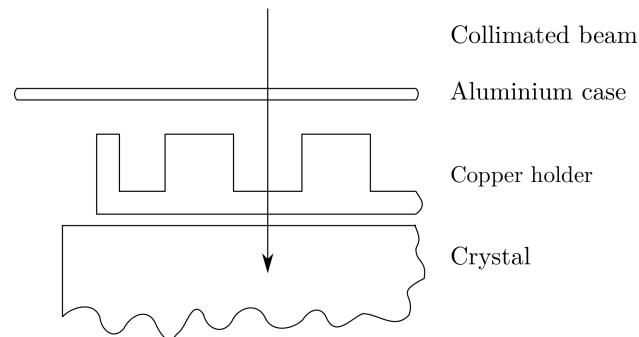


Figure 4.13: Simplified scheme of the elements found during the lateral scans of the detectors.

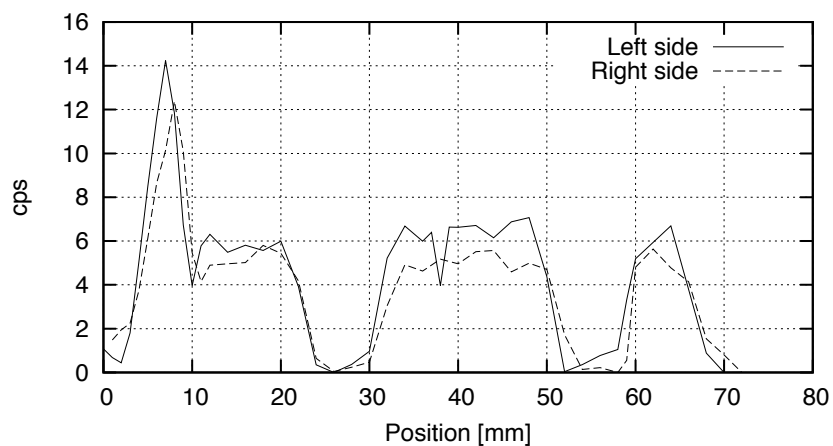


Figure 4.14: Curves resulting from the lateral scans of one detector.

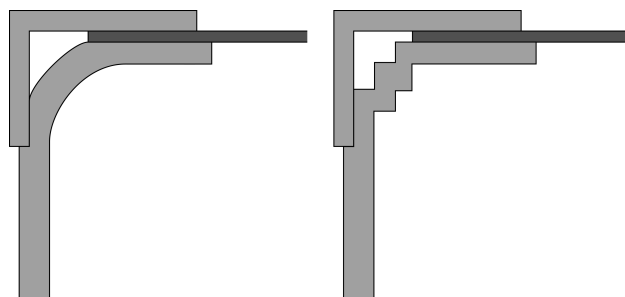


Figure 4.15: Updated model (left) of the corners of the detector case and model simplified (right) to make it compatible with MCNPX.

approach has been chosen. As first step, the flat top was set to its minimum and only the rise time was changed. The same procedure was performed with the parameters inverted and the two resulting best values were combined to obtain a first estimate of the optimal settings (the graphs are plotted in figure 4.16 and 4.17). Further measurements have been performed around this point to improve the settings and the best resolution has been reached. The curves representing the final resolution of the detectors are plotted in figure 4.18.

Among the different detectors, only two of them present performances compatible with the expected values, but no evident causes of the problem were found. However, less than six months later, detector 3 had been brought to factory due to a failing FET¹ and detector 1 suffered a problem with a partial loss of vacuum. Detector 4 has not yet been checked but it is also expected a loss of vacuum, just as detector 1 already experienced. The loss of vacuum makes the compressor run faster to compensate; this produces more vibrations and as consequence a widening of the peaks.

4.2.3 Radiographies and Estimation of the Dead Layer

The model of detector 3 (the one presenting the best resolution) was improved by using radiographies as a tool to measure the position and size of the internal components of the crystal casing. Additionally, a series of measurements with low-energy emitters helped to improve the model of the same detector by adapting the dead layer thickness to the measured value, significantly different from the value reported in the specifications.

The radiographies were performed at the St. Vincentius-Klinikum in Karlsruhe. The detector was placed lying on one side on a stretcher below a X-ray tube and the sensitive film was placed below the stretcher, as for thorax radiographies. The electronics of the preamplifier was shielded using lead. The distance source-stretcher was 1.2 m, in order to obtain images not significantly deformed by the spread of the rays.

¹Field effect transistor, used to perform a first amplification of the signal generated in the germanium crystal.

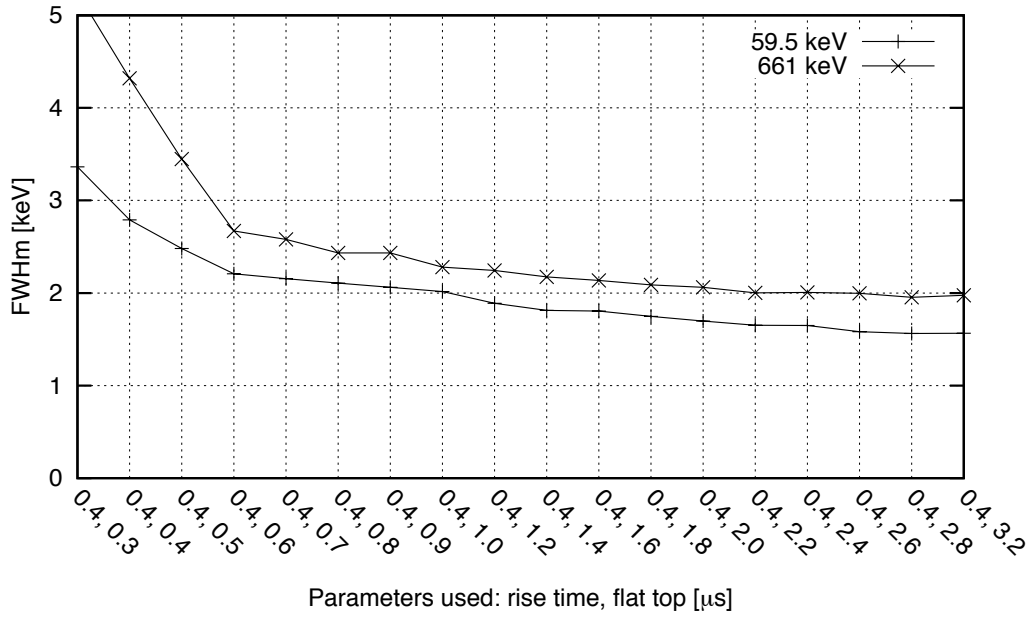


Figure 4.16: FWHM of a detector as function of different flat top values.

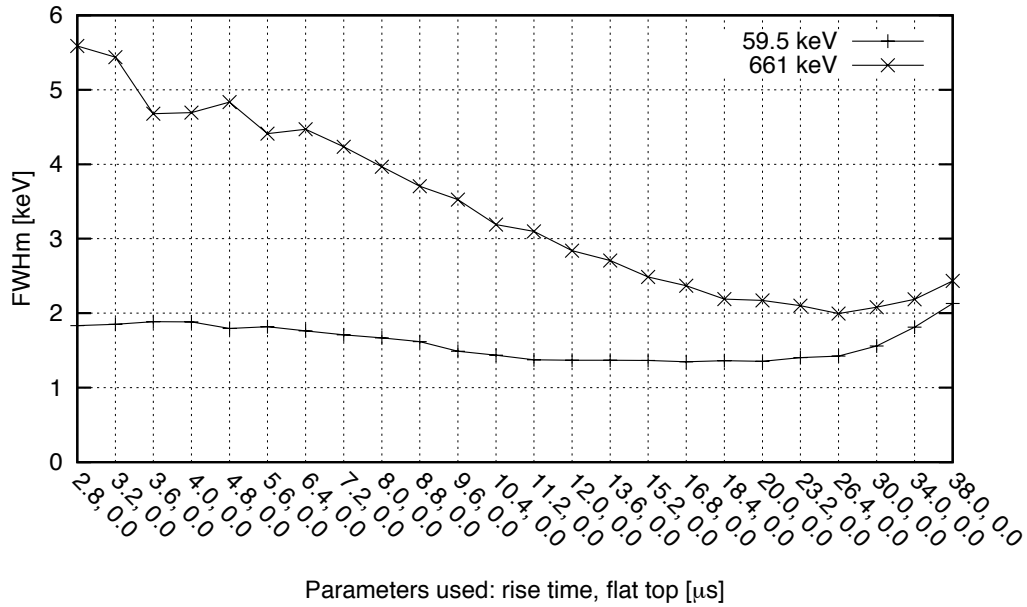


Figure 4.17: FWHM of a detector as function of different rise time values.

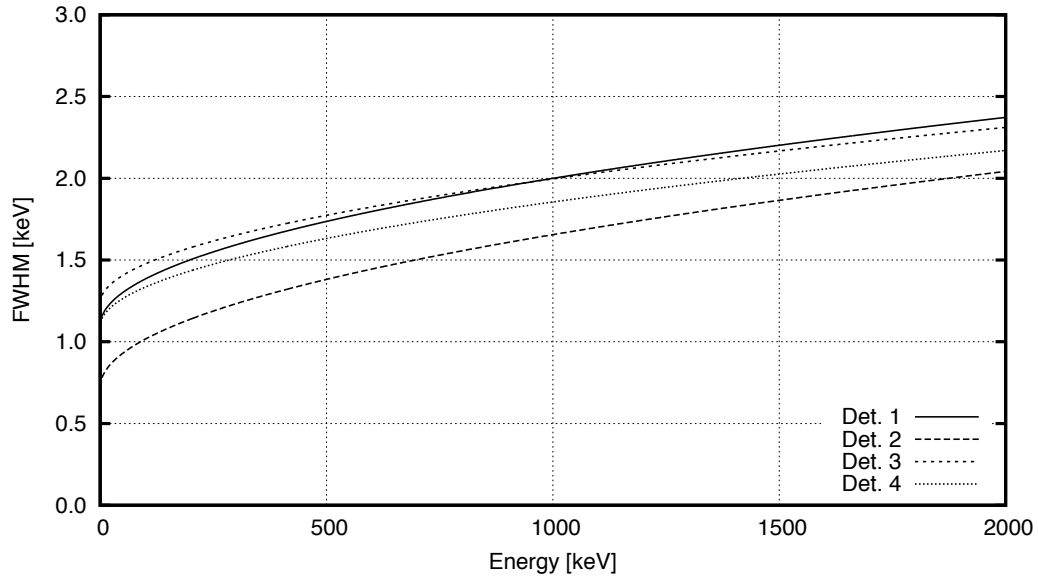


Figure 4.18: FWHM of the different detectors after the optimisation.

Using the light guides provided by the instrumentation, a first image was obtained with the rays aligned to the carbon-epoxy window. Using this first image, the distance between crystal and entrance window was calculated and the detector consequently shifted to have the X-ray beam aligned with the front of the crystal. The attempt was successful and all the following pictures have been taken with this configuration. Different settings have been tried until a good contrast between crystal and metallic components was obtained, but the X-rays were still unable to penetrate the crystal and show the inner hole. An example of the radiographies is shown in figure 4.19.

The different radiographies show a crystal tilted 1.2° toward the bottom of the aluminium case, probably due to its weight, and a distance between crystal and entrance window higher than expected: 7 mm instead of 5 mm. The dimensions of the crystal are however perfectly matched to the specifications. The MCNPX model was modified accordingly.

Concerning the thickness of the dead layer, an approach using collimated point sources has been chosen. Each source (^{241}Am and ^{137}Cs) was placed inside a tungsten collimator producing a rectangular beam 5.5° and 1.6° wide. The source was placed off-axis to avoid influences by the inner hole. The

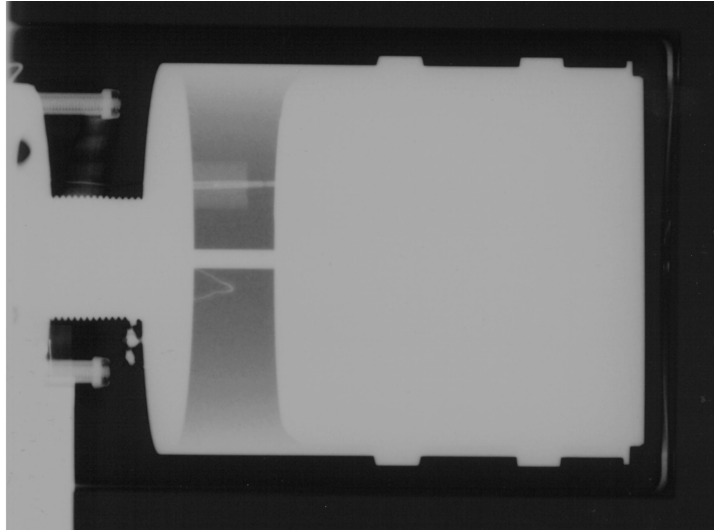


Figure 4.19: Radiography obtained with 125 keV, 1.2 mAs exposure.

resulting spectra have been processed with *Genie-2K* and, after a manual check to ensure the quality of the fits especially in the low-energy region of the spectrum (below 25 keV), the net peak area calculated. Parametric simulations with different dead layer thickness have been performed with MCNPX and the best fit chosen as final value: $7.5 \mu\text{m}$, about 20 times higher than $0.4 \mu\text{m}$ quoted by the manufacturer. All the details on the experience are given in Elanique et al. (2011). Another measurement has been performed on the same detector after changing the position of the beam: it is reported in the literature that the dead layer thickness could be inhomogeneous. The results show detection efficiencies 2-10% higher, suggesting a thinner dead layer and the need of further measurements to obtain an average value for the whole surface and to mitigate the effects of thin- and thick-spots.

4.3 Validation of the results

The different versions of the models of the detectors have been validated with different methods. The first test performed, not counting the measurements with point sources already described, consisted in measuring a subject contaminated with ^{241}Am in the bones and comparing the estimates with the

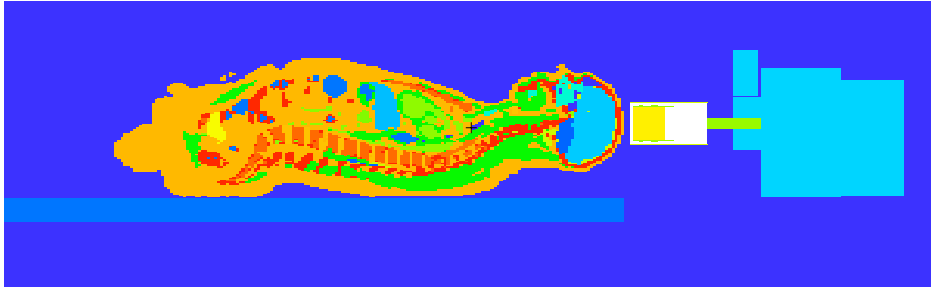


Figure 4.20: Scheme of the configuration used for the measurement of the subject with the germanium detector. The phoswich detectors are not shown and the phantom used is MEETMan.

value obtained with other detectors. Another test consisted in measuring an IGOR phantom (see section 3.3.2 for a description of the phantom) loaded with known amounts of radionuclides and the last test consisted in comparing a measurement of a LLNL torso phantom with simulations.

4.3.1 Contaminated Subject

The first test of the quality of the detector model was performed by measuring a subject contaminated with a large amount of ^{241}Pu and with its decay product, ^{241}Am , a bone-seeker nuclide. The results of the measurements were compared with the estimates obtained with phoswich detectors.

The subject has been measured with phoswich detectors around the head (sides and back), leaving space for one of the germanium detectors on the top side on axis with the body. Figure 4.20 shows the configuration and the phantom used for the numerical calibration.

Two different kinds of calibration have been performed: numerical and physical. The former used the MEETMan phantom with the bones loaded homogeneously with ^{241}Am , the latter used a head phantom loaded only on the inner surface of the skull. The resulting efficiency was scaled to the fraction of bone mass present in the head (19%), calculated using the MEETMan phantom. A summary of the efficiencies and of the calculated activities is listed in table 4.3. The efficiency data and their uncertainties are not available for the phoswich system, since the value was obtained with a mix of numerical

Table 4.3: Results of the measurement of a subject contaminated with ^{241}Am . Uncertainties in percent quoted at 1σ are reported between parentheses. The efficiencies report only the MC statistical uncertainties, no value is available for the differences between simulated and measured bodies.

	Efficiency	Activity (Bq)	Ratio to reference
Phoswich	—	1135 (20)	1
Physical calibration	$4.66 \cdot 10^{-4}$ (4.5)	532 (6.1)	0.47 (21)
Numerical calibration	$2.67 \cdot 10^{-4}$ (2.3)	928 (4.8)	0.82 (21)

simulations, physical calibrations and also previous measurements of the same subject. As standard value, the uncertainties are fixed at 20%.

The results show a significant discrepancy between the physical and numerical calibrations. Possible explanations are a different distribution of the radionuclide (inner surface of the skull for the physical phantom, homogeneous for the numerical phantom) and a different bone thickness and density (MEETMan is based on a subject bigger than the average man). The final activity estimates show a better match for the numerical calibration, with less than 20% deviation from the reference value. The discrepancy can be explained by the structure of the head phantom (see figure 4.21), presenting more inactive material on one side and therefore decreasing the expected efficiency. Further details, including calculations about the potassium content of the subject, are available on Marzocchi and Breustedt (2009).

A new evaluation of the measurements may be performed in the future, since a voxel model of the reference woman is now available and could better reproduce the different bone structure of the subject.

Being the model of the detector the first revision and the discrepancies mostly due to differences in the structure of the phantoms, the results were considered acceptable and the model used for further simulations, without the urgent need of a new characterisation.

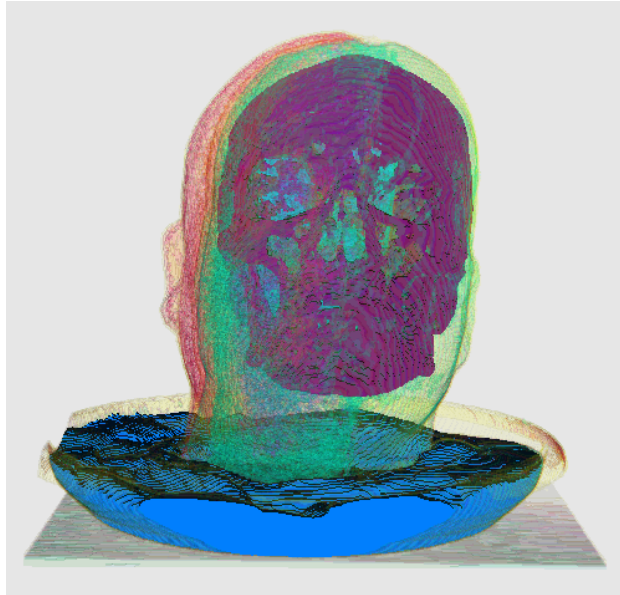


Figure 4.21: View of the inners of the head phantom used for the calibration (Schwabensland, 2010). One side presents more inactive tissue, thus lowering the measurement efficiency.

4.3.2 Intercomparison Exercise 2008

The Intercomparison exercise is a yearly test of the capabilities of different WBC facilities spread around Germany. The exercise is required in order to comply with German regulations and the DIN EN ISO/IEC 17025:2005 rules. As part of the exercise, the laboratories must provide an estimate of the activity of an IGOR phantom loaded with an unknown amount of radionuclides as if it were a normal routine measurement. In 2008, in addition to the detectors of the WBC at IVM, two new HPGe were used to obtain independent estimates.

The HPGe detectors were placed one below the hips of the brick phantom and one on the left side of the phantom, as shown in figure 4.22. The position was not optimised but chosen to avoid influences on the spectra recorded by the scintillators and compatible with the mechanics of these detectors. The location of the HPGe detectors was measured with a laser device and later reproduced in the MCNPX simulations. The evaluation of the results has been performed with the software *Genie-2K*, after manually entering the

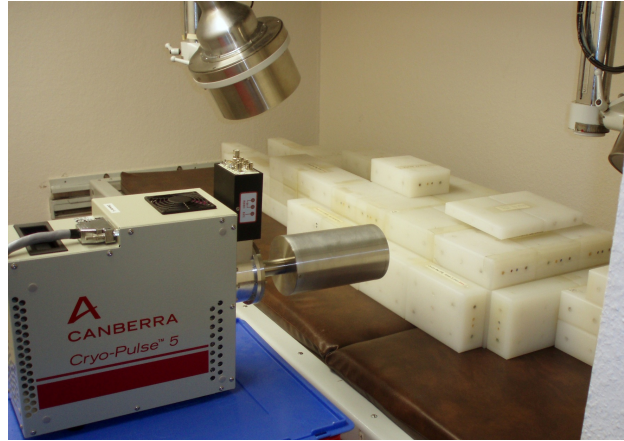


Figure 4.22: Configuration used for the measurements of the P4 phantom during the intercomparison exercise of 2009. The second detector was placed below the hips of the phantom and is not visible in the picture. The plate over the thorax is used to cover an additional rod added for a second series of measurements.

efficiencies obtained numerically with MCNPX.

The results of the exercise show a good agreement between the results of the old NaI system and the reference values, but there is space for improvement in the new system: the values are always underestimated by 10-20% and almost 30% for ^{133}Ba (see figure 4.23). The problem can be linked to different causes: positioning of the detectors, number of detectors, model of the detectors. Concerning the former, the position of the detector on the side of the phantom was measured only at the beginning of the measurement, but not at the end: if the cart used moved by 3 cm during the measurement due to its weight, being the distance between source and crystal about 40 cm, the change in efficiency would be about 15%. Such increase would lower the final error to about 10%. The detector placed below the stretcher in a fixed position could not move and produced better estimates of the activities in the phantom (see table 4.4), but it was unable to detect ^{241}Am placed only in the upper part of the torso.

Concerning the number of detectors, the old system uses four of them arranged in an optimal configuration, able to compensate small shifts of the subject. This was not possible with the HPGe detectors, since only two of them were

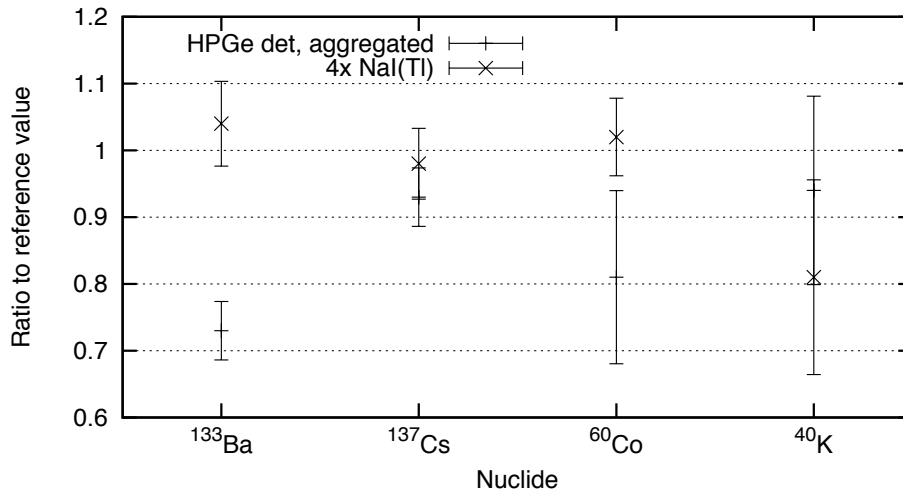


Figure 4.23: Results of the intercomparison exercise with the HPGe detectors aggregated.

Table 4.4: Results of the intercomparison exercise 2008 with phantom P4.

	Det. below Bq	Det. on the side Bq	NaI(Tl) Bq	Official value Bq
Am-241		58 098 (2.6)		18 021 (5.0)
Ba-133	2 185 (7.5)	1 810 (6.4)	2 866 (3.5)	2 736 (5.0)
Cs-137	4 160 (4.6)	4 083 (4.3)	4 354 (2.1)	4 432 (5.0)
Co-60	1 199 (6.6)	946 (6.6)	1 370 (2.8)	1 338 (5.8)
K-40	3 227 (18)	2 051 (22)	2 287 (17)	2 807 (5.0)

available and were arranged in a temporary configuration.

As last source of error, the model used for the detector on the side had not yet been optimised, it was simply built using the standard data supplied by the manufacturer. This could have increased the magnitude of the errors.

Further data on the exercise are available on Urban and Bickel (2009).

4.3.3 Validation of a LLNL Torso Voxel Model

In 2008 the LLNL torso phantom available at IVM was brought to the St. Vincentius-Klinikum in Karlsruhe and scanned with CT. The resulting images were used to produce a voxel model of the phantom, later coarsened

to make it suitable to the available MCNPX version and computer speed: from 3.4 millions voxel, the final size was reduced to 126 thousand voxels (resolution of 2.8125 mm on the transverse plane and 2.4 mm along the length). For the description of the method, see Hegenbart (2009).

The validation of the voxel model was performed using the first HPGe detector supplied by Canberra, being it the only one with a reliable MCNPX model. To make the measurements perfectly reproducible in the simulations, the phantom was laid on the floor of the PBC chamber and some marking were set on it, to correctly reproduce its position within the virtual world. The detector was mounted on a support specially designed for this task and the angle between detector and floor accurately set to 90°.

Different measurements have been performed with active liver and lung lobes. The initial measurement for each of these configurations was performed with the detector aligned to the centre of the markings painted on top of the phantom, but lateral and vertical shifts, raging from -6 cm to +6 cm, have also been tested. The goal was obtaining estimates of the variation in efficiency as result of positioning errors. To reduce this kind of errors to a minimum, an in-house developed laser positioning system was used for the plane parallel to the floor and a flexible string was used to measure the short distance detector-phantom surface (0-6 cm). A sample measurement configuration is shown in figure 4.24 (the real set-up) and in figure 4.25 (the virtual set-up). The measurements used two different nuclides (^{241}Am and ^{239}Pu) and different overlays for the phantom.

The numerical and experimental results are in very good agreement, with deviations always within uncertainties and usually lower than 5% for the main ^{241}Am peak (see figure 4.26 for a subset of the results). Even when the ratio channel-by-channel of the whole spectrum is considered (see figure 4.27), the agreement is good: the only deviations requiring further analyses are the lowest-energy range, below 30 keV, and the region around 50 keV. The former is difficult to correctly simulate because the emission probabilities of the X-rays are not known with good precision and there are discrepancies among the different sources. Furthermore, the shape of the X-ray peaks cannot be correctly modelled by MCNPX or by the other most important MC softwares



Figure 4.24: The phantom and the detector used for the experiment.

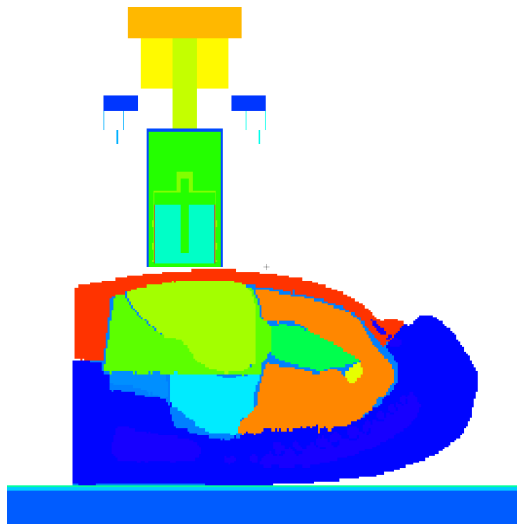


Figure 4.25: Plot of the MCNPX geometry used for the validation of a liver measurement. The different materials are represented with different colours.

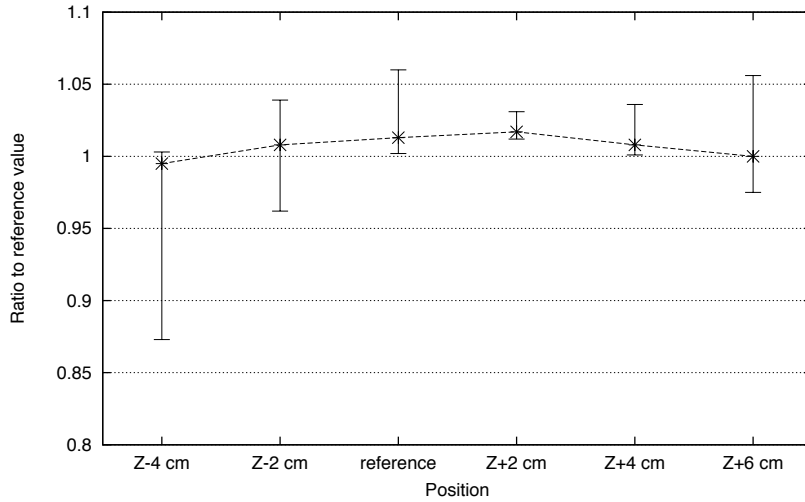


Figure 4.26: Agreement between simulations and measurements for different counting positions around the reference liver configuration without overlays. The errors take into account positioning errors and have been calculated using further simulations with shifts applied to the measured detector position.

Table 4.5: Ratio simulation over measurement for different energy regions of the spectrum obtained with liver, ^{241}Am and no overlays.

Energy region	Ratio
10-47 keV	0.952
47-52 keV	1.033
57-64 keV	1.013

(see Gómez-Ros et al., 2008). The lowest-energy region is also affected by the dead layer thickness, value of difficult estimation. The discrepancy around 50 keV may be originated by the fluorescence peaks of the 59.5 keV main line, located about 10 keV below the main emission line, and will be investigated in the near future. A summary of the agreements in the different regions of the spectrum for the reference liver counting configuration is given in table 4.5.

This analysis took into account mostly the results of measurements with ^{241}Am , since the organs containing ^{239}Pu also contain ^{241}Am due to the in-growth from ^{241}Pu since the initial isotope separation. Using the calibration data obtained with the ^{241}Am organs, an estimate of the amount of con-

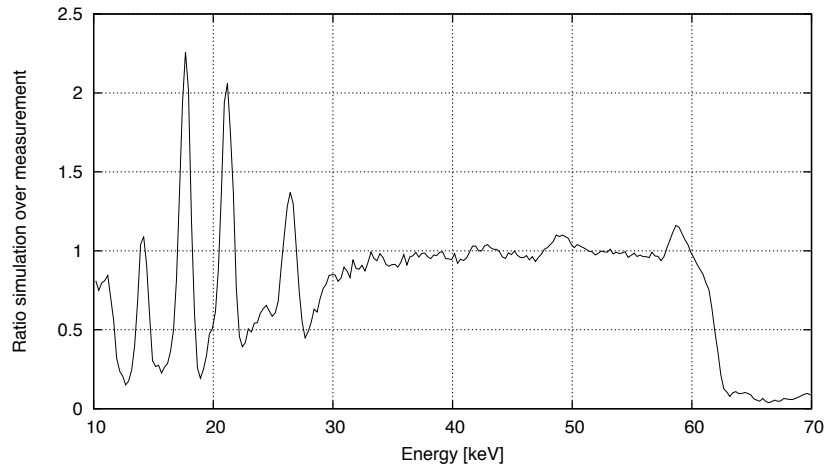


Figure 4.27: Plot of the ratio channel-by-channel simulation over measurement for the spectrum obtained with liver, ^{241}Am and no overlays.

tamination in the ^{239}Pu liver has been performed. The results indicate that the initial plutonium mixture contained 0.013% (atom fraction) ^{241}Pu , value comparable with the capabilities of generic isotope separation processes.

For a more complete description of the experiment, see Hegenbart et al. (2009) and (Urban and Bickel, 2009, pagg. 126-128).

Chapter 5

Setup of an Optimised System

This chapter describes the different application scenarios for the newly acquired system and the methods used to develop the optimal measurement configurations for each one. The development of the mechanics to handle the detectors and some tests of new system are also discussed.

5.1 Goals

Three scenarios have been planned for the system being developed. The first one consists of WBC routine measurements, using the system as alternative to the current NaI(Tl) detectors. The advantages would be the better nuclide identification and better activity estimation in contamination cases with low-energy emitters or with overlapping lines, like for ^{60}Co : its two main peaks overlap with the ^{40}K peak in spectra from NaI(Tl) detectors and the calculation of the activity is more complicated.

Another scenario is the routine measurement of subjects at risk of incorporation in lungs, as alternative to the current phoswiches. The main advantage would be the better identification of peaks in the low-energy region of the spectrum, since the resolution of the phoswiches is too coarse for the effective separation of the low-energy lines.

An additional measurement scenario includes all the special cases outside the routine, the most important being skull and knee measurements to identify

and quantify bone-seeking nuclides, mixed lungs-liver measurements and thyroid measurements.

The different measurement scenarios present opposite challenges: routine measurements require high detection efficiencies to keep the measuring time short and the throughput of the system (subjects per day) high, but the identification of nuclides distributed in the whole body also require low dependency of the detection efficiency from the position of the contaminant, implying higher distances detectors-subject and lower efficiencies. Concerning the counting configurations, WBC measurements can be performed in a fixed configuration common to all subjects, while the detectors during PBC measurements should be placed in a counting configuration dependent on the size of the specific subject: a higher flexibility is required. Since the goals are significantly different, partial-body and whole-body set-ups have been optimised independently and a mechanics able to give enough degrees of freedom was specifically designed for the goal.

Concerning the different counting geometries, some are available in the literature (see ICRU69), but only two of them have been selected and investigated further: the stretched configuration and the sitting configuration. The former has been chosen because already in use in the pre-existing WBC and PBC at IVM, the latter because it required less floor surface in the counting room/chamber and it could give more freedom in the positioning of the detectors and attain better performances in some measurement scenarios, most notably the skull set-up. This was especially important in the beginning, before choosing the PBC room as chamber for the new system.

The choice between the two configurations could be made only after an estimate of the performances was available, therefore the first step was the optimisation of the PBC measurements.

5.2 Optimisation of PBC Configurations

The most important partial body measurements performed in the PBC at IVM are bones, liver, lung lobes. The optimisation of each of these configurations involved four steps: set-up of the phantom in the counting configuration;

execution of the simulations to show the photon flux generated by the source; placement of the detectors around the phantom; execution of new simulations and calculation of the MDA.

5.2.1 Set-up of the Modified Phantom

The phantom used for this batch of simulations is MEETMan, since it was the only complete phantom available at IVM in digital form at that time. The stretcher and chair were set-up with the same materials, only the shape differed. More specifically, the stretcher was modelled as simple plate 75 cm wide, 5 cm thick and 2 m long and the support for the chair was made of the same plate rearranged to suit the new shape (see figure 5.1 for a representation). The material used was water but with the density reduced to 0.5 g/cm^3 : this simplified model was meant to reproduce a wide range of possible materials, from light wood to different polymers. The goal was not to obtain an accurate representation of the attenuation of the photons, but only orders of magnitude, since the actual stretcher had not yet bought.

The adaptation of the MEETMan model to the sitting configuration was performed partly manually partly with the aid of the software Voxel2MCNP (see Hegenbart, 2009). This software was first used to cut the original phantom into three volumes: torso and upper part of the hips, lower hips and upper part of the legs, lower part of the legs and feet. The exact cutting planes have been chosen to represent a real sitting set-up: head of the femur, middle of the knee. A first revision, shown in figure 5.1, used the voxel volumes without overlapping regions, thus leaving air in between and changing the total phantom length. Later an improved version was produced with the three voxel regions partially overlapping (see figure 5.2). No significant difference have been found in the results, therefore the initial simulations in chair configuration were kept and not performed again.

The software Voxel2MCNP was used also to optimise the volumes to remove excess air voxels and to produce MCNPX input files. These were not suited to be used as-is, because MCNPX does not accept sources in the hidden part of the overlapping volumes. The source definitions have been

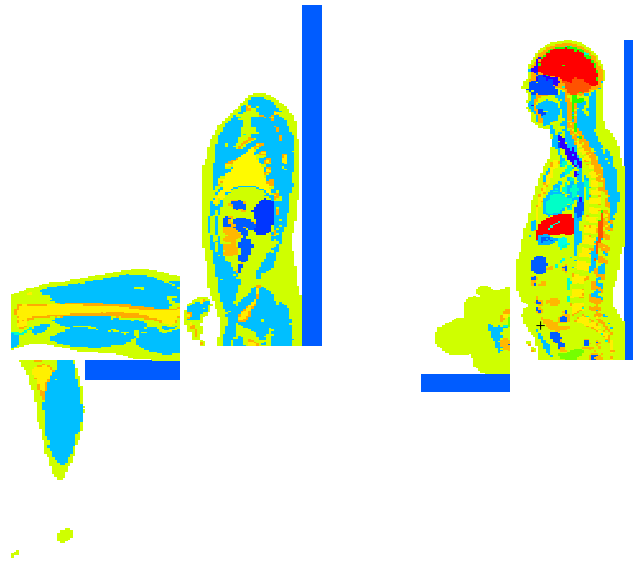


Figure 5.1: Two sections, through spine and left leg, of the MEETMan phantom in sitting configuration, first revision with air between the voxel volumes. The support of the phantom and the air inside the phantom are plotted with dark blue, the different organs with other colours. The floor is reproduced with a thin green line.

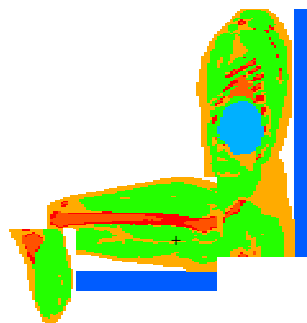


Figure 5.2: Section through the left leg of the MEETMan phantom in sitting configuration, second revision with overlapping voxel volumes.

processed with script written in Perl (The Perl Foundation, 2008) and the sources from the hidden voxels were removed. The change influenced the number of source voxels, but the relative weights of the different volumes were kept constant, to keep the original distribution of particles in the different body parts.

The simulations were set-up with sources only in the organ of interest (initially bones, liver, lung lobes) and with a ‘mesh tally’ in the space around the phantom. The mesh tallies are a method to extract different values (e.g. photon flux, deposited energy) from regions of space within the simulated geometry. They produce a three-dimensional matrix of values, one per element of the mesh. In this specific case, the mesh tallies tracked the photon flux, integrated over the whole solid angle and over the energy range of interest: the results are scalars. The photon flux was chosen because it is directly related to the efficiency. The output files generated by MCNPX were later converted with a Perl script to VTK format (Kitware Inc., 2003) and processed with Paraview (Kitware Inc., 2008-09).

The results of the simulations, however, could not be used as-is, since they consisted in matrices of photon fluxes. To make the definition of the optimal position easier, a visual representation of the fluxes was desired. First of all, a model of the phantom was introduced in Paraview, then the data of the mesh tallies were processed with a ‘contour’ filter (Schroeder et al., 2006). This filter takes as input matrices of scalar values and produces iso-surfaces corresponding to the scalar values chosen by the user.

5.2.2 The Configurations

The data generated by MCNPX do not contain information about the direction of flight of the photons, but the issue was not considered important, since the better the detector position (nearer to the source), the more perpendicular the photons are. A factor that plays a more important role in this genre of optimisation is the energy of the photons emitted from the source and tracked by the mesh tally: the lower the energy, the more pronounced are the lobe of the iso-flux surfaces and the stronger the dependence of the optimal position

from the characteristics of the source. To be able to optimise the detector as good as possible, ^{241}Am (59.5 keV) was used as source.

Bones The results for the sources placed in the bones are shown in figures 5.3 and 5.4. The sitting configuration exhibit some artefacts below the torso block and in front of the knees: since the inners of the voxel model are exposed without covering tissues, the photon fluxes are higher and the iso-surfaces deformed, farther from the body. The stretched configuration does not present the issue.

Two possible counting positions are the skull and the tibia. The latter can however be safely discarded: the flux is apparently high, but the tibia could be covered by varying amounts of fat, depending on the constitution of the subject being measured, making the calibration dependent on at least one additional parameter. In addition, the placement of detectors near the tibia would be difficult: the detectors should be positioned outwards, meaning that the two compressors would collide with each other: the space available between the legs is scarce. The most important factor is however the shape of the bone: it is too thin to cover the whole surface of the detector, thus wasting part of it. An hypothetical detector long and thin would be better suited, but a coaxial as the ones available at IVM are suited to measure large surface emitters, covering the whole entrance window. The skull was therefore chosen for the optimisation.

The optimisation was performed manually, since no suitable algorithm has been found. The regions where the iso-flux surfaces are the farthest from the surface of the phantom were preferred and each detector was placed perpendicular to them, to reduce the effective thickness of the entrance window and to offer the biggest possible surface to the photons. Five positions have been tested: four on the sides, one on top of the skull, but not all of them at the same time, since the possible placements of the detectors depend on the geometry of the room. More specifically, the sitting configuration made impossible or significantly difficult the placement of a detector on axis with the torso (on top of the head there is no space in the counting chambers), only the detectors around the skull have been used. The stretched configuration

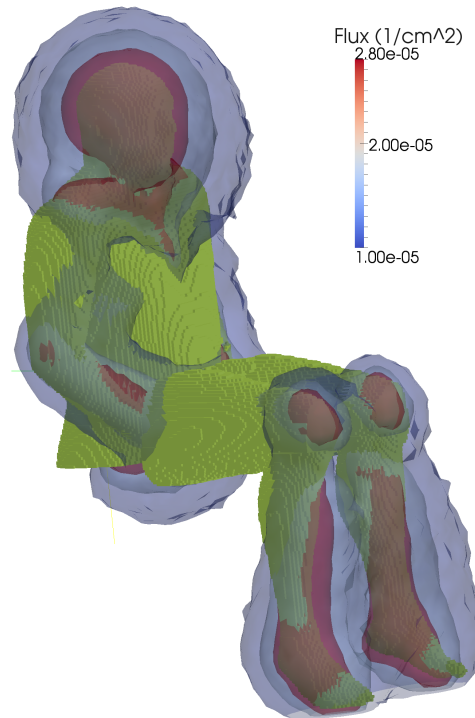


Figure 5.3: Iso-surfaces originated by a ^{241}Am source placed in bones. Sitting configuration.

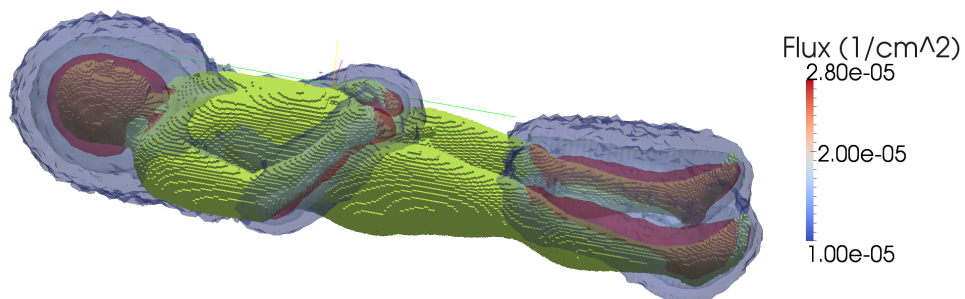


Figure 5.4: Iso-surfaces originated by a ^{241}Am source placed in bones. Stretched configuration.

makes the placement of detectors arranged as a ring difficult due to the mechanics, that should be able to rotate the detectors with many degrees of freedom and at the same time keep the detectors near the floor: only a detector on axis with the head and one below the head have been taken into account. The configuration used for skull measurements is shown in figure 5.5 and the configuration used for the stretcher is shown in figure 5.6.

Liver The optimisation of the counting configuration was performed similarly. The resulting iso-flux surfaces for the sitting configuration are shown in figure 5.7, the surfaces for the stretched configuration are the same (they are not affected by the lower part of the body) and are not plotted.

The difference between the two configurations resides again in the compatibility of the detector positions with the counting rooms. The iso-flux surfaces show that two detectors should be placed in front of the liver: one directly in front of it and one in the front-side. Placing a third detector on the side of the subject would be desirable, but it is preferable to avoid uncomfortable positions for the people being measured: the arm would need to be kept over the detector or somewhere else for over 30 minutes. This option was therefore discarded and will be considered only for special cases. In addition to the two detectors in front of the subject, the other two can be placed behind the organ to collect some additional photons, despite the flux being reduced by at least a factor of two. The final configuration for the sitting set-up is shown in figure 5.8 on the left. The stretched configuration, given the restrictions in the mechanics, could not accept four detectors, therefore a compromise was found. One detector was placed on top of the liver, in close contact with it, the other one was placed behind the back, in a position equivalent to the third detector of the sitting configuration. The resulting set-up is shown in figure 5.8 on the right.

Lungs The detectors XtRa with electric cooling are bulky and can be placed one near the other only side by side. As result, the placement of more than two detectors in front of the subject is not possible, even if it were the best option to measure the lungs: the highest photon flux is available near the

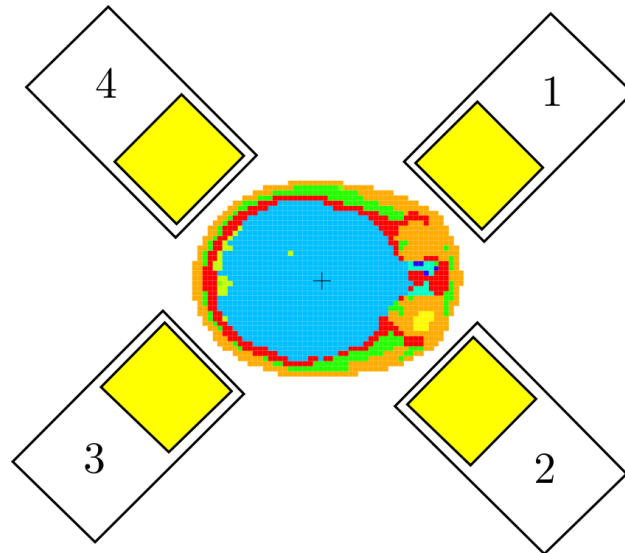


Figure 5.5: Arrangement of the detectors for bones measurements, sitting configuration. The number are used only for reference.

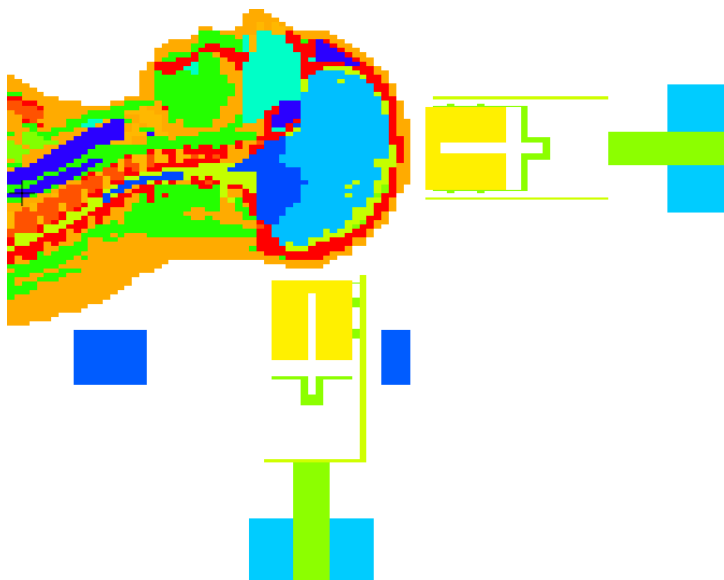


Figure 5.6: Arrangement of the detectors for bones measurements, stretched configuration.

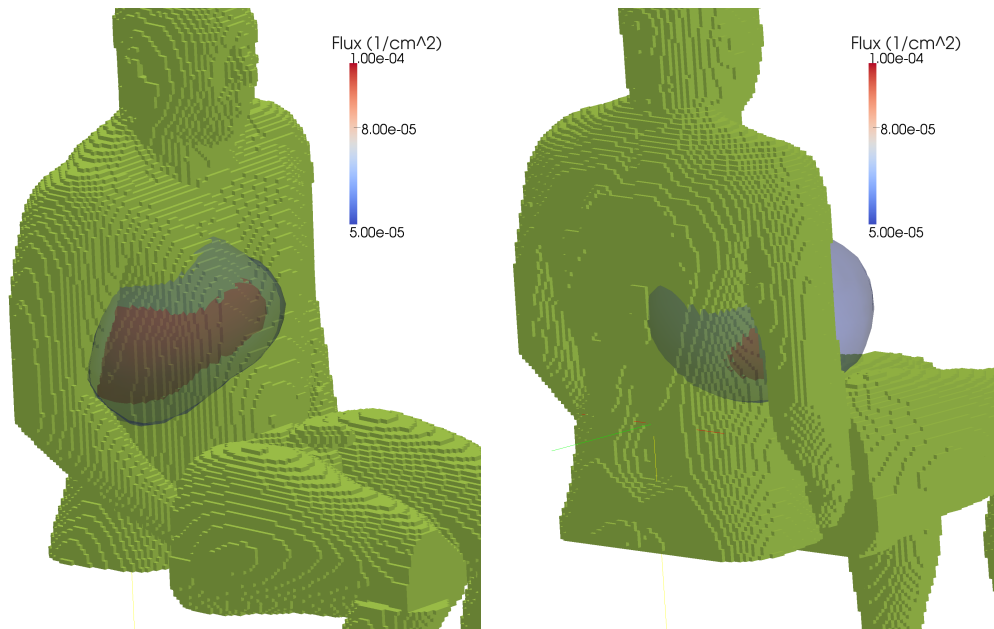


Figure 5.7: Iso-flux surfaces obtained for a ^{241}Am source in liver.

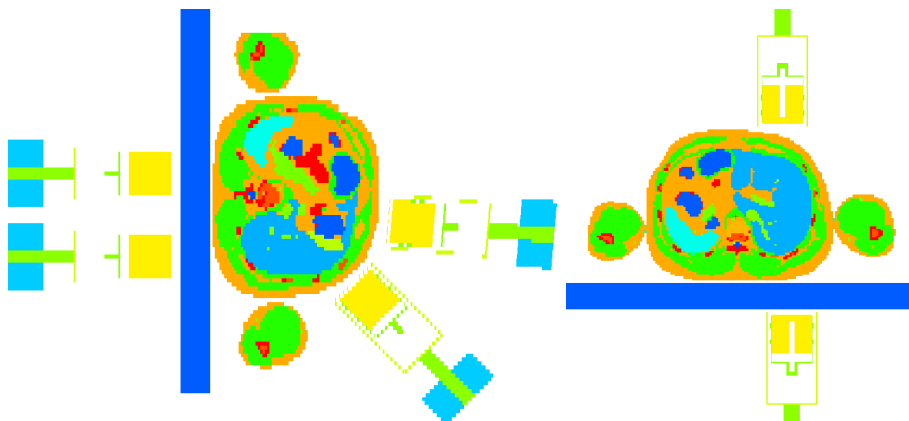


Figure 5.8: Arrangement of the detectors for liver measurements. Sitting configuration on the left, stretched configuration on the right.

chest, as shown in figure 5.9.

The definition of the position of the detectors was the same for the two configurations, with two detectors over the chest perpendicular to the surface and two detectors behind the torso, facing the lungs. Figure 5.10 shows two of them.

5.3 Choice of the Counting Configuration

5.3.1 The Resulting MDAs

The MDA attainable in each measurement configuration was used as criterion to evaluate the efficacy of the set-ups. Since the system was not yet available, the MDAs were calculated on simulated spectra using the formula provided by international standards (ISO).

A measured spectrum contains contribution from different sources: the ^{40}K peak and its Compton scattering background visible at lower energies; the contaminant nuclide (goal of the measurement); the natural background in the room. The calculation of the MDAs was performed in this case using four spectra:

- three simulated spectra to represent realistically the Compton background: the organs with the highest potassium content and nearest to the detectors (liver, brain and muscles) were taken into account. The relative activity distribution was chosen according to the real potassium content reported in the literature (ICRP89): 3% brain, 4.5% liver, remaining fraction in muscles (the other organs have been neglected);
- one spectrum obtained from a real background measurement in the PBC chamber.

The spectra generated by the nuclide of interest were used only for the calculation of the detection efficiencies (one of the parameters required by the formula). Concerning the values assumed for the calculations, the measurement time was 2000 s (i.e. standard measurement time in the current PBC) and the ^{40}K content of the subject was chosen to be 4000 Bq, according to ICRP23. The ROI for ^{241}Am was 17 channels wide and the background

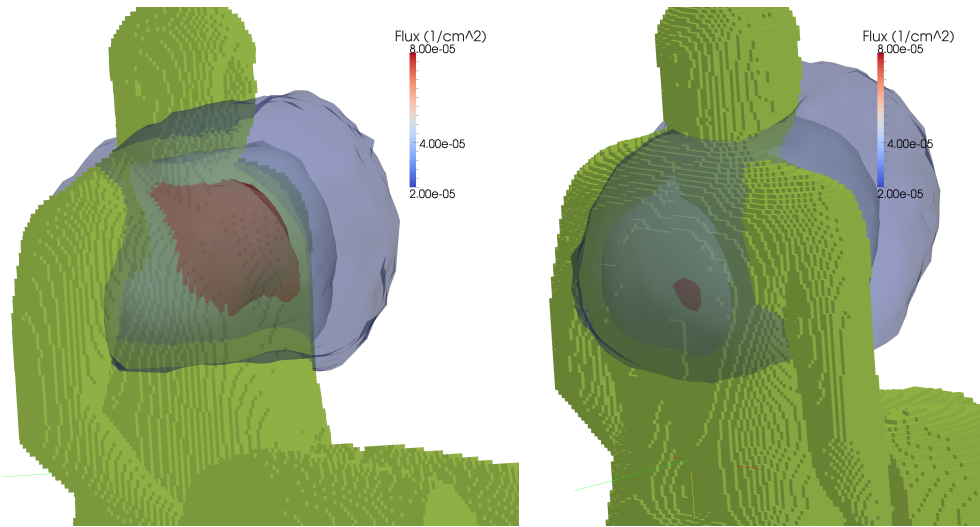


Figure 5.9: Iso-flux surfaces obtained for a ^{241}Am source in lungs.

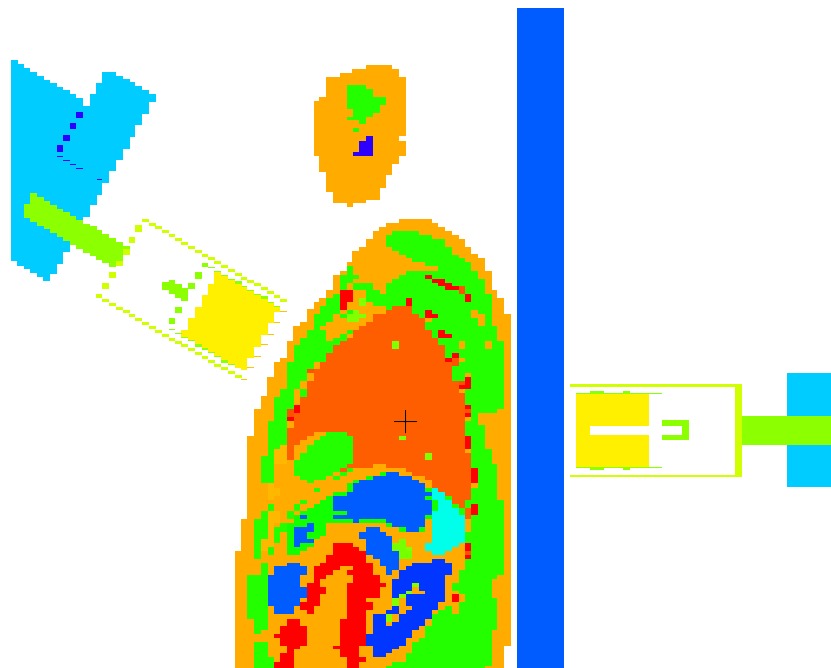


Figure 5.10: Arrangement of the detectors for lungs measurements, detail of the torso. Section through the left lung.

Table 5.1: Comparison of simulated MDA values attainable for measurements of the skull with different detector arrangements. Errors can be estimated as 10%.

Set-up	Detector	MDA (Bq)
Sitting	Det. 1	70
	Det. 2	75
	Det. 3	64
	Det. 4	60
Stretched	on axis	80
	behind skull	76

regions were 8 channels wide. The MDAs are considered with a standard 10% uncertainty, since the different contributes to the final error are not reliably calculated. Just to cite some of them, small errors in the positioning of the detectors in the different positions of the phantom produce variations in the computed efficiency up to 5%, the estimation of the background counts originated by ^{40}K is always reproducible with good precision, but the shape of the phantom will never be found in real measurement, since each person is unique, and the discrepancy could easily affect the number of background counts up to 10%. As result, 10% has been used as standard uncertainty for the final MDA estimates.

Bones The results of the simulation for the skull configuration are summarised in table 5.1. The detectors arranged as a ring around the skull (sitting configuration) produce the lowest MDA for every detector, but the values are well within the uncertainties: the detection efficiency in case of low-energy emitters depends mainly on the surface and solid angle exposed to the detector, which is in this geometry nearly independent on the subjects' size and weight. The Compton scattering originated by muscles in the upper part of the torso also seems not important, since the solid angle covered by it in relation to the detectors is small. The brain, being directly in front of the detectors, is the most important source of ^{40}K photons and of spurious background.

Table 5.2: Comparison of simulated MDA values attainable for measurements of the liver with different detector arrangements. Errors can be estimated as 10%.

Set-up	Detector	MDA (Bq)
Sitting	Front	15
	Front-right	26
	Back	85
	Back-centre	230
Stretched	Front	20
	Back	105

Liver The MDAs attainable are listed in table 5.2. The detectors in the sitting set-up assume a ring arrangement: front, front-right, back, back-centre and the attainable MDAs change progressively from 15 Bq to 230 Bq. This effect can be explained by two contributions. The first one is the varying thickness of the tissues interposed between source and detector: the torso wall is thicker behind. The second contribution is the different solid angle covered by the liver in relation to the detectors: almost constant for the first three, significantly smaller for the detector near the spine. The simulations of the stretched configuration produce comparable values, slightly better for the detector placed in front of the liver, slightly worse for the detector behind. The explanation involves the cross-counting efficiency of the detector for ^{40}K sources in the muscles: an higher counting efficiency produces also an higher Compton background in the low-energy region of the spectra. The cross-counting efficiency for the torso is comparable in the two configurations, but the counting efficiency for ^{40}K sources in the legs is different: in the sitting configuration the detectors behind the torso are shielded by body of the subject, the detectors in front of the liver are near to the legs and directly exposed.

Lungs The calculated MDAs are listed in table 5.3. The values are perfectly equivalent for the two configurations, since the influence of the lower part of the body is negligible in comparison to the contribution of the organs and muscles of the torso itself.

Table 5.3: Comparison of simulated MDA values attainable for measurements of the lungs with different detector arrangements. Errors can be estimated as 10%.

Set-up	Detector	MDA (Bq)
Sitting	Front	7
	Front	5
	Back	21
	Back	21
Stretched	Front	7
	Front	6
	Back	21
	Back	21

5.3.2 The Choice of the System

The simulations using MCNPX and the calculations using the latest standards showed comparable MDAs for the sitting and stretched set-ups, with the liver being the only exception: the detectors in front of the body are at slight advantage in the stretched set-up, but the detector directly behind the organ is at much stronger advantage in the sitting set-up, as already explained. Globally, the differences are not significant enough to select one of the two configurations.

The mechanics that would be required to attain the best performances and the space required to position the detectors is however more important: if the subject is kept sitting, the positioning of the detectors behind the torso and around the head in different positions is feasible, while a stretched configuration would not leave below the subject enough space to be able to easily reposition the detectors. In addition, some measurement configurations would be limited and not all the detectors could be put to use. The sitting configuration was therefore chosen. Previous results, using a different formula and some more constrained detector set-up for the stretched configuration, are also available in Marzocchi et al. (2010a), but the conclusion is the same reported here: the stretcher offers more freedom and better results for the detectors placed in front of the subject.

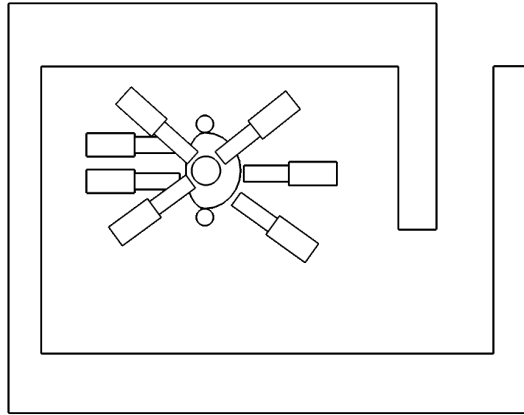


Figure 5.11: Sketch of the space occupied by a minimal system compared to the size of the WBC room.

Concerning the placement of the new system, both the PBC chamber and the WBC room have been evaluated. The WBC room has a major advantage over the PBC chamber: it has no door to open and close for every measurement. Partial body measurements last 2000 seconds and the 30 seconds required to open and close the door play no role, but the new system is meant to be used also for WBC applications, where the counting time is currently 300 seconds. The increased time required per measurement would lower the throughput of the laboratory. The WBC room, however, is small and it could have been used only if the number of degrees of freedom of the system were kept low (vertical and horizontal translation, one rotation), but this would hinder its capabilities. Figure 5.11 shows a sketch of the room: the risk of hitting the walls is high, the subject would probably feel oppressed and the operators would have difficulties in placing the detectors safely and easily in the correct position for each measurement.

The PBC chamber could be used for the new system, being it significantly wider and longer (see section 4.1.1), but the current stretcher leaves not much space free in the room. Two options have been considered: completely replace the current stretcher or move it toward the door to leave more space free at the closed end of the chamber. The first option (see figure 5.12) would require a new hybrid chair, able to be used also as stretcher: the mechanics of the

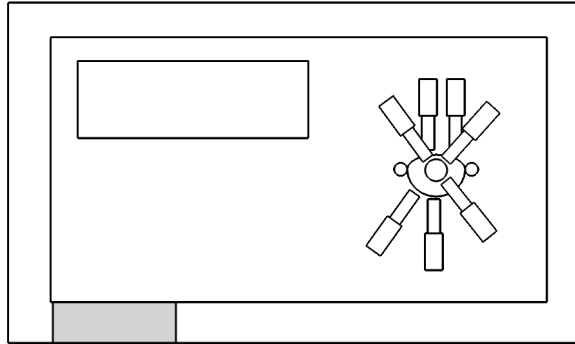


Figure 5.12: Sketch of the space occupied by a minimal system compared to the size of the PBC room.

phoswiches requires a subject lying horizontal. The second option, however, would affect the design of the mechanics almost as if it were installed in the WBC room: the space is constrained and the space around the system limited. As final decision, the complete redesign of the room and the installation of a hybrid stretcher/chair was decided.

Different stretchers and chairs are available in the catalogues, with the wellness stretchers and the dental chairs being the most common. The former can be used as flat stretcher, but not in chair configuration, the opposite for the latter: they do not reach the flat set-up. In this case both were acceptable, since the phoswiches do not need a perfectly flat stretcher. Two models were found in the catalogue from Cosmoderm: Veda, a wellness stretcher, and a dental chair (Cosmoderm Reichert GmbH, 2011). Both are shown in figure 5.13. The two products have an important difference: the back of the support for the torso is made of metal in the dental chair and of wood in the wellness stretcher. The use of metal would reduce significantly the transmission of the photons and would introduce additional scattering, thus worsening the MDAs. The Veda stretcher was therefore chosen for the final set-up also thanks to some additional features: there is an hole in the back of the torso part that could be used to position a detector near to the skin; the support for the legs can be moved independently and lifted to obtain an arc configuration (optimal for WBC measurements) or left flat to reduce the Compton scattering contribution of the legs during PBC measurements.

5.4 Definition of the Mechanical Set-Up

The stretcher is made of four parts: independent and reclinable support for the torso; fixed support for the hips; two supports for the legs, operated together. A detailed drawing of the new stretcher is shown in figure 5.14, where the configuration completely reclined is reported.

The degrees of freedom required by each detector are five: three translations along the three axes and two rotations, the first around a vertical axis and the second around an horizontal axis, both perpendicular to the crystal. A rotation around the axis of the crystal is not required.

The specific ranges of movements/rotation were defined according to the configurations previously developed, adapted to the reclined stretcher (see figures 5.15, 5.16, 5.17). The system is expected to be able to suit at least the 99 percent man and woman (with height as parameter), therefore the data reported in Tilley (2002) were used to define the capabilities of the mechanical system. The expected sizes of the subjects and the degrees of freedom for each detector are listed in table 5.4 and table 5.5, both referred to the dimensions shown in figure 5.18.

The definition of the details of the mechanics was redacted in close collaboration with the KIT-Sicherheitsmanagement department (“KSM”, safety department), being the development of the mechanics outside the goal of this work. Given the weight of the detectors (about 25 kg each) and the number of degrees of freedom, the task is also not trivial.

Among the different alternatives, the best suited to the PBC chamber is shown in figure 5.19. The Veda stretcher is placed in the middle of the room and is used also for the phoswich detectors, being the old stretcher dismantled, two of the new HPGe detectors are hanging from the rails already available on the ceiling, two detectors are mounted on carts and can be moved freely in the room. Main characteristics of the new system are:

- common design of the rotating head where the detectors are mounted: carts and hubs differ only in the system used to move them in the room;
- rotation of the detector around the centre of gravity: the detectors feel weightless;



Figure 5.13: The alternatives taken into account for the final choice of the stretcher/chair, courtesy of Cosmoderm (Cosmoderm Reichert GmbH, 2011).

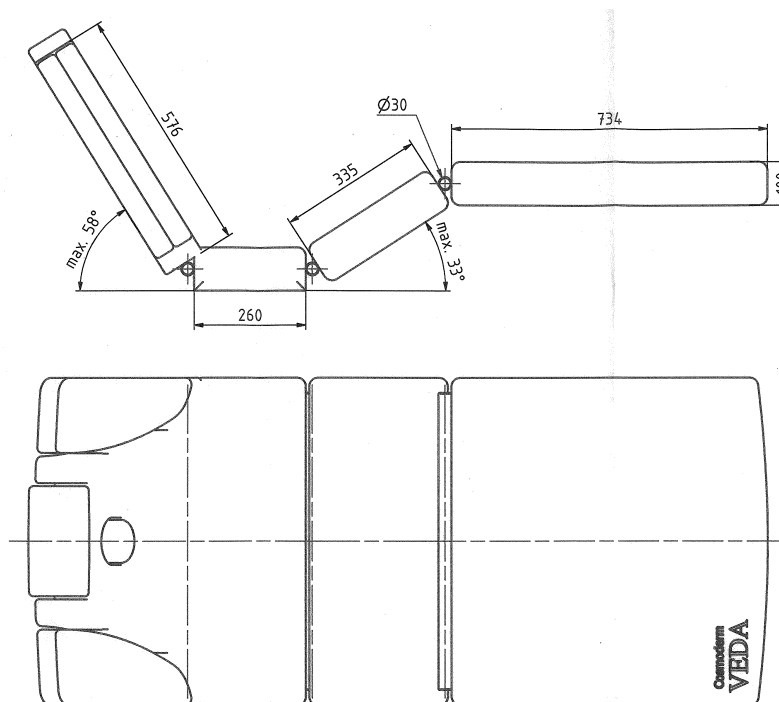


Figure 5.14: Drawing of the Cosmoderm Veda wellness stretcher, sizes in millimetres, courtesy of Cosmoderm (Cosmoderm Reichert GmbH, 2011).

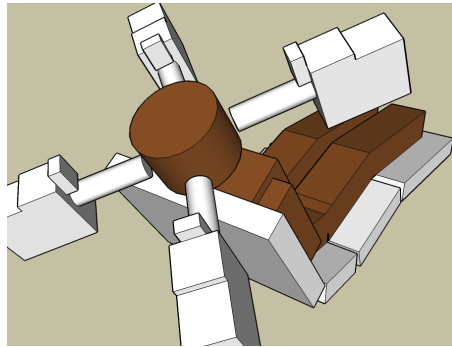


Figure 5.15: Configurations for measurements of the skull.

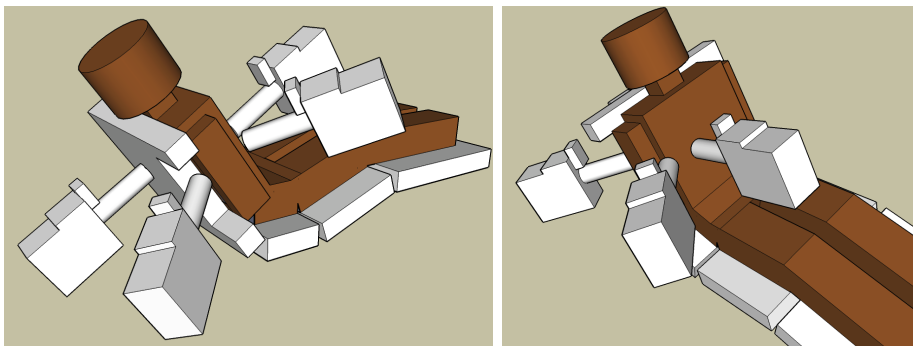


Figure 5.16: Configurations for measurements of the liver.

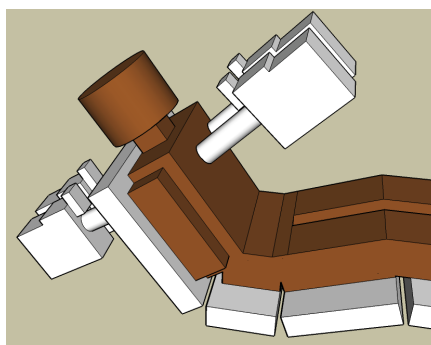


Figure 5.17: Configurations for measurements of the lungs.

Table 5.4: Characteristic sizes of subjects, as taken from Tilley (2002). The gender was neglected and each value chosen independently. Dimensions are reported in figure 5.18.

	1 %ile (wo)man (mm)	99 %ile (wo)man (mm)
Hips-sitting surface (a)	60	100
Hips-shoulders (b)	400	521
Hips-top of head (c)	700	900
Head-sitting surface (e)	540	820
Chest width at the liver (f)	200	350
Chest total depth	190	320
Abdomen total depth	191	350
Head-knees (d)	—	740
Total width at knees	230	340

Table 5.5: Degrees of freedom of the detectors, referred to figure 5.18. Positions refers to the centre of the entrance window. The angles are measured on a vertical plane and referred to the horizontal plane. The rotation around the vertical axis is 360° for all detectors.

Detector	X Axis (mm)	Y Axis (mm)	Z Axis (mm)	Angles
Front left	-350/200	500/830	-580/660	$-30^\circ/-80^\circ$
Front right	-100/350	500/830	-580/660	$-30^\circ/-80^\circ$
Rear left	-200/200	0/830	-650/0	$0^\circ/35^\circ$
Rear right	0/200	0/830	-650/0	$0^\circ/35^\circ$

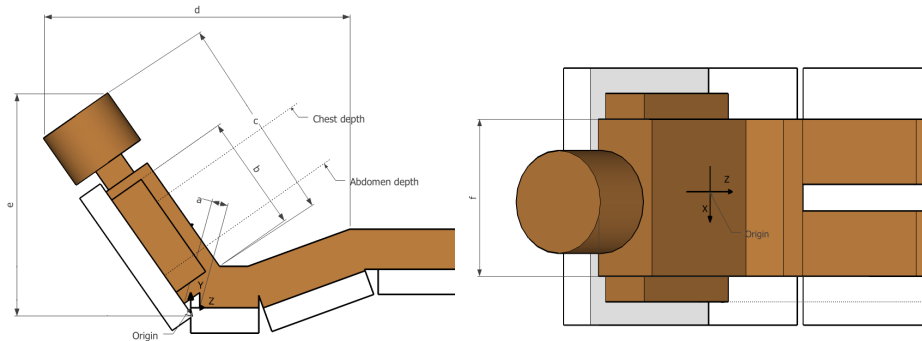


Figure 5.18: Sketch of a subject with dimensions used in table 5.4.

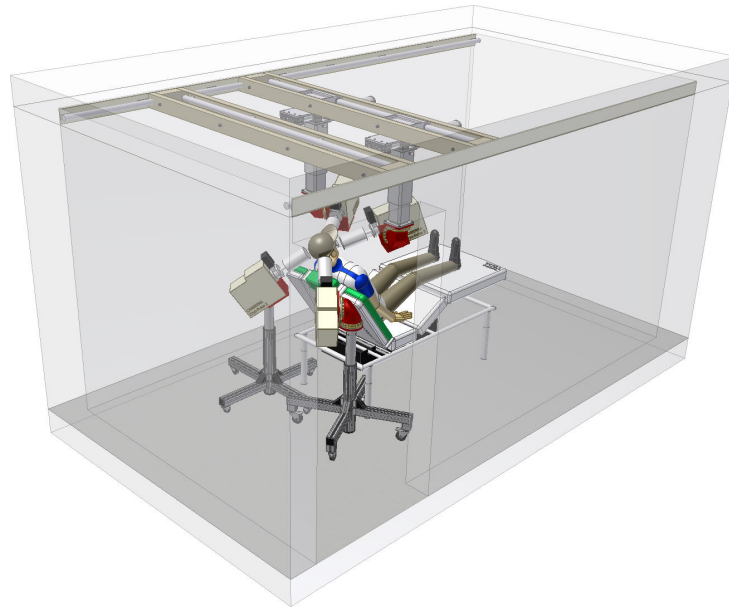


Figure 5.19: Drawing of the new PBC/WBC chamber. The old phoswich system is kept but not shown.

- offset for the hanging detectors: they share the same rail of the ceiling but they can be offset up to about 40 cm along the head-feet direction of the subject; the lateral shift is independent;
- electrical operation of the height of the hubs/carts, manual movement of the detectors in the other directions;
- electronic sensors to read the angles and the heights, to be able to reproduce the measurements in the simulations; the automatic detection of the position in the room of the hubs/carts is not yet possible;
- brakes for the rotating head to keep the desired position during the measurement.

A detail of an hub is shown in figure 5.20.

Before assembling the final system, a simplified portal was installed in a separate room (see figure 5.21) and used to perform tests with different phantoms and subjects. It showed the need for a modification of the WBC configuration, as discussed in the next section, and of a modification of the stretcher: the hole in the reclinable part had to be enlarged to make space for the detector head.

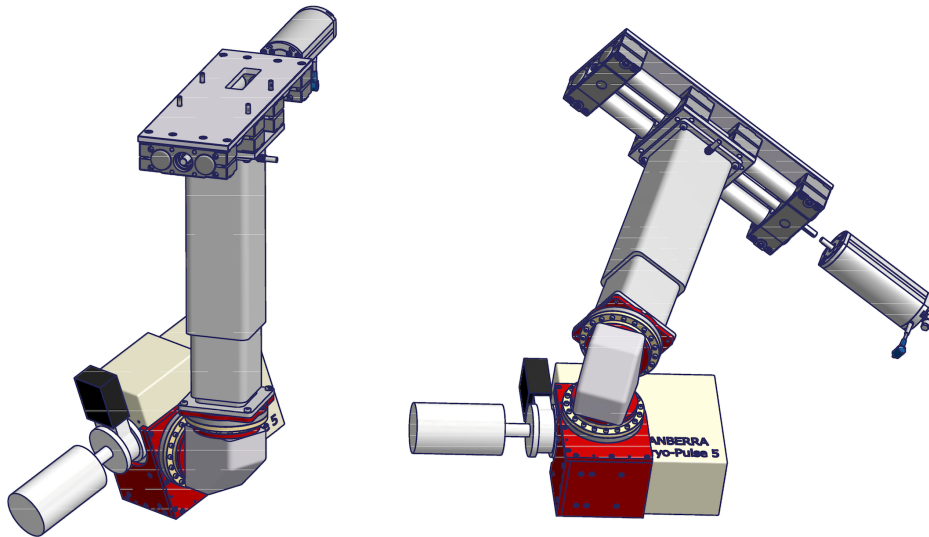


Figure 5.20: Scheme of the support for the detectors hanging from the ceiling.

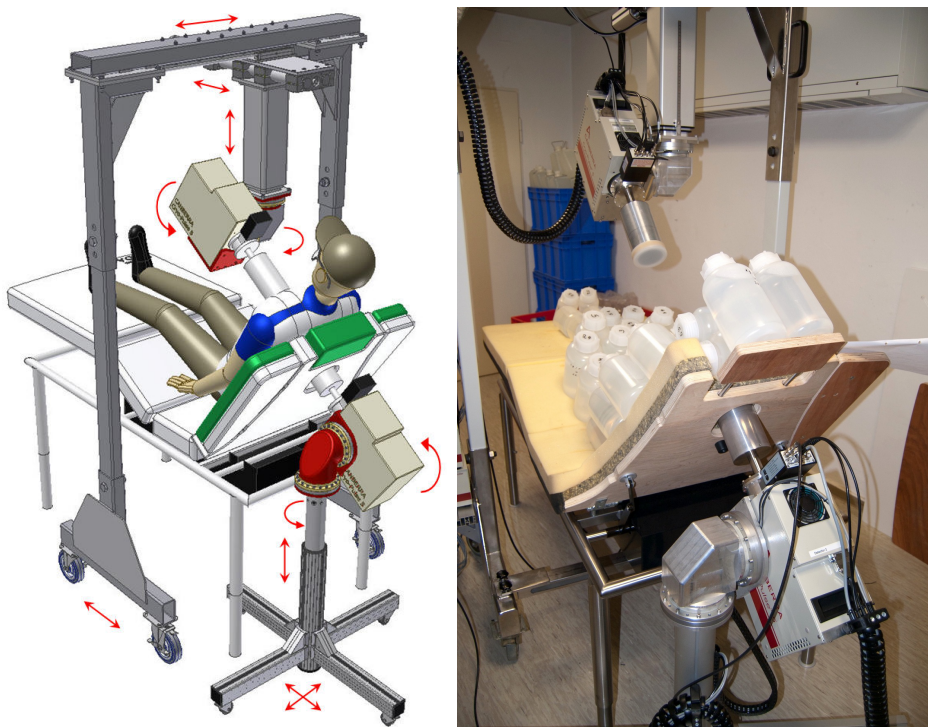


Figure 5.21: On the left, scheme of the portal. The degrees of freedom are marked with red arrows. On the right, photo of the portal during a measurement of the bottle phantom, adapted to the reclined configuration and lying on a prototype of the stretcher.

The system in its final configuration is shown in figure 5.22 and 5.23.

5.5 Optimisation of a WBC Configuration

As already discussed elsewhere, WBC measurements have multiple goals: the main goal is the detection of the smallest possible amount of radionuclides, just as the PBC measurements, the second goal is the achievement of a homogeneous detection efficiency independently from the distribution of the contaminant in the subject, to produce a correct estimation of the activity. The first goal can be reached with detectors placed near the subject, the second goal with detectors placed farther from the subject. If the subject assumes an arc configuration, the second goal is easier to attain and the detectors should be placed near the focal point of the arc.

Given the different and multiple goals, the optimisation of the WBC configuration could not be performed using the same method described for the PBC set-ups, therefore the method has been modified.

5.5.1 Method

The basic data used for the optimisation of the WBC set-up are obtained with the same procedure used for the previous step: further simulations have been performed and the photon fluxes collected with mesh tallies. The approach was not changed because it gives the opportunity to collect in a single simulation fluxes in many different points of space around the phantom. By processing this data, a significative speed-up compared to the execution of different simulations is always achieved. To make the simulations perfectly comparable, the grid used for the mesh tallies has been kept constant among all the simulations. Its size was $142 \times 172 \times 312$ cm and each cell defined as a cube with edges 2 cm long. Further increasing the density of the grid would have only worsened the statistics per cell without bringing advantages to the final results.

Given the availability of new voxel phantoms from the Helmholtz Zentrum München, simulations have not been limited to MEETMan but performed



Figure 5.22: Detector mounted on a hub in its final configuration.



Figure 5.23: Final system, ready for measurements. The second detector on a cart is not shown.

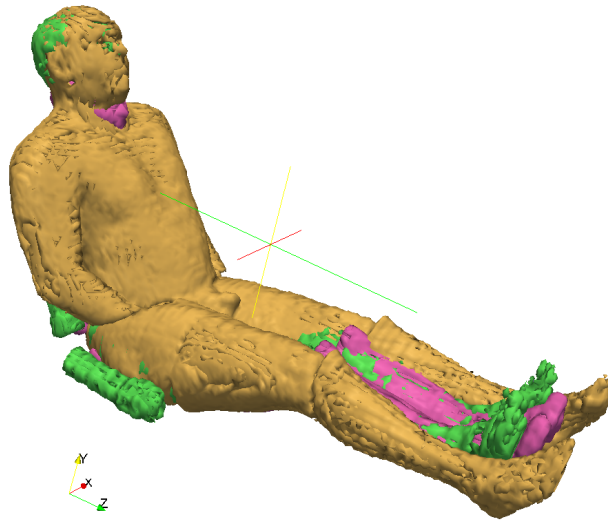


Figure 5.24: Phantoms MEETMan (orange), Godwin (green), Klara (pink) configured for the reclined stretcher. The Klara phantom is smaller and its nose is visible below the chin of the other two phantoms. The surfaces shown represent the fat and skin layers of the models (the outermost layers).

also with a female (60 kg) and a male (70 kg) models, similar in shape and size to the reference subjects (see Zankl et al., 2005). All the three models have been adapted to the reclined configuration planned for the new system (previously shown in figure 5.14) and the overlapping regions removed, as described in section 5.2.1. The removal of the air gaps was required to keep the total length of the modified phantoms equal to the originals and to avoid a deformation of the resulting iso-flux surfaces. Figure 5.24, showing the three phantoms overlapping with each other, is useful for the comparison of the relative sizes and shapes.

Different simulations were performed with each phantom, each simulation with a mono-energetic source in one specific organ. The organs used for the simulations were brain, bones, gastrointestinal-tract (“GIT”), liver, lung lobes, muscles, thyroid. Except for the thyroid, simulated only with a 364 keV source, all the other organs were simulated with different energies, each one corresponding to one possible contaminant: 60 keV (^{241}Am , tested even if it is not redistributed in the whole body), 661 keV (^{137}Cs), 811 keV (^{58}Co),

1173 keV and 1332 keV (^{60}Co), 1460 keV (^{40}K).

The results of the mesh tallies were post-processed with Perl scripts and two new quantities were calculated. More specifically, selected simulations (e.g. all the ones with the source in a specific organ) were grouped and passed to the scripts. The scripts would take the corresponding cells of the different simulations and calculate (after proper weighting according to the masses of the organs) the average flux among them and its standard deviation, normalised to the previously calculated average flux (hence normalised standard deviation, “NSD”). The NSD in some cells can therefore be higher than one, since the intensity of the flux varies significantly as consequence of the specific source and geometries used. The formulas used for the calculations are:

$$\bar{F}(x) = \frac{\sum_i F(x_i)}{n} \quad (5.1)$$

$$NSD(x) = \sqrt{\frac{\sum_i (F(x_i) - \bar{F}(x))^2}{n}} \quad (5.2)$$

where

i refers to the input mesh;

x refers to the coordinates of a specific cell in the grid;

$F(x_i)$ is the photon flux in cell x of the input grid i ;

n is the number of input meshes.

The NSD data represent the variation in the photon flux connected to a change in the source and/or phantom geometry (for example, position of the source and the shape of the subject). Its value and the average flux are calculated independently cell by cell: mixing the values within the same mesh tally would be useless for this study.

The resulting set of average fluxes and NSDs were processed again with Perl script to obtain the distribution of their values and also converted in VTK format to be visualised graphically with Paraview.

5.5.2 Distributions of Standard Deviations

Before defining the final configuration, some conclusions can already be obtained from the values of the NSDs. For this step, the cumulative values of the NSD distributions are required:

$$V_f(k) = j : \frac{\int_0^j N(NSD) dNSD}{M} = k \quad (5.3)$$

where ‘:’ means ‘such as’ and

k is the fraction of the total mesh tally volume;

j is a NSD value;

$N(NSD)$ is the distribution of standard deviations within the elements of the grid;

M is the total number of elements (cells) of the grid.

In other words, $V_f(k) = j$ means that the ‘best’ fraction k of the mesh tally volume implies a NSD up to j . Increasing the desired fraction of volume increases monotonically the corresponding NSD that has to be accepted.

A first possibility is to keep the data for different energies separated and to merge some or all the other variables (phantoms, source organs). The cumulative values of the NSD distribution are reported in figure 5.25. The data show that the $V_f(0.125)$ for 60 keV, 661 keV, 1460 keV are respectively 23%, 15%, 12%. It is important to remember that the regions of the grid with the smallest NSD are the ones farthest from the subject, because the source from afar can be approximated as point and the angular distance between different sources decreases. If low standard deviations are desired, only a small fraction of space within acceptable distance from the subject would be available for the detectors. If a larger fraction of the mesh tally volume has to be made available for the detectors, the NSDs would increase, for example $V_f(0.25)$ corresponds to respectively 30%, 20% and 16%. Such a volume would still be completely situated in front of the subject: the lowest NSDs calculated behind the phantoms are 46%, 28% and 22%.

The data reported refer to the results for the three phantoms merged together, therefore they reflect the quite common case where the calibration

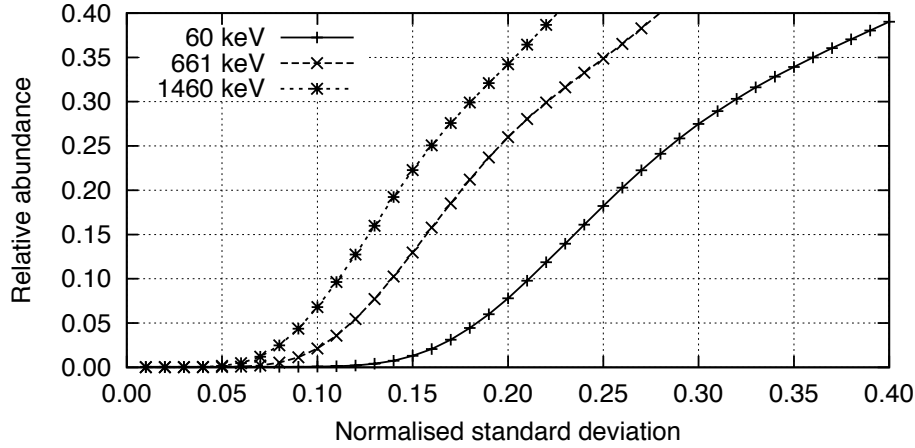


Figure 5.25: Integrated and normalised distribution of the NSD values in the volumes of the mesh tally. The data of the three phantoms were merged. The sources were placed in liver, lungs and GIT.

data are independent from the shape of the subjects. If different specific calibrations and detector configurations are available, the NSDs become significantly lower: the variation of the detection efficiencies are no more dependent on the subject, only on the position of the source among the different organs. For example, the $V_f(0.25)$ values for the Godwin phantom are respectively 13%, 10% and 8%.

This first example simply proves that low-energies are not detected reliably with WBC systems, because the detection efficiencies are strongly dependent on the position (not to mention the losses in air) and that calibrations adapted to the different body shapes and sizes help significantly to increase the accuracy of the activity estimations.

If only an high-energy emitter (such as ^{40}K , 1460 keV) is taken into account and all the different organs are merged, while keeping the phantoms independent, another result is obtained. Figure 5.26 shows the resulting curves. The curves are similar to each other, since high-energy photons interact little with matter, and one common calibration and detector configuration are enough for all the phantoms. Nevertheless, the results for Godwin and Klara are almost identical, only MEETMan differs visibly. This can be explained by the simultaneous contribution of two factors: body size (MEETMan is

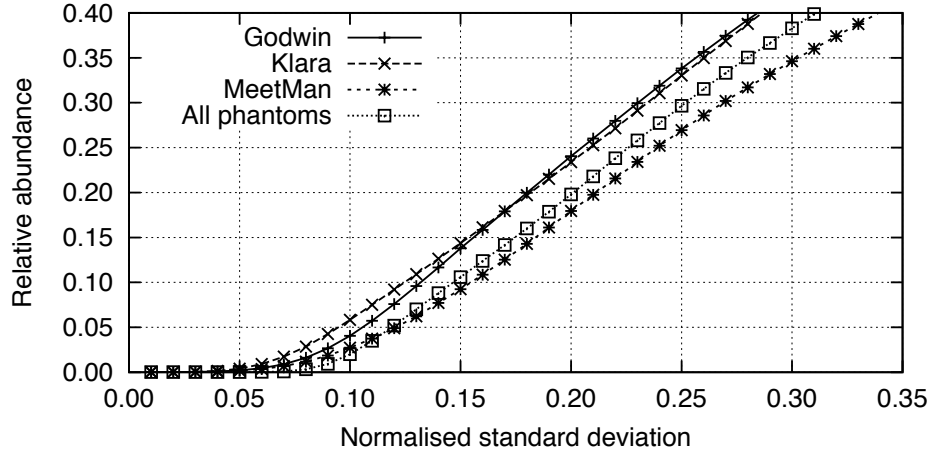


Figure 5.26: Normalised distribution of the NSD values when a 1460 keV source is located in different organs.

taller) and amount of fat and muscle tissues, resulting in a weight about 40% higher than Godwin and 65% higher than Klara.

To summarise the results, this second test confirms the need of different calibration data for subjects of different sizes, but shows that the shape (man/woman) is not important in the measurement of high-energy emitters in WBC configurations. Further information on the topic is available on Marzocchi et al. (2010b).

5.5.3 Definition of the WBC Detectors Set-Up

The definition of the WBC set-up was performed independently for the different detectors, since each one was given a specific task. The iso-NSD and iso-flux surfaces were plotted and compared. In some cases, as for the thyroid discussed below, the surfaces were simple and the task easy, in some other cases, as for whole-body contaminants, the simple observation of these two values was not enough and a formula has been applied to the flux and RSD data to produce a new quantity. The formula used is:

$$C = a \cdot NSD + b \cdot \log f \quad (5.4)$$

where a and b are parameters chosen manually and f is a photon flux. In other words, the formula weights the two contributes (linearly the NSD and logarithmically the flux) to produce a composite value C better able to suggest an optimal compromise for the position of the detectors. Other formulas without logarithm or with other mathematical operations were tested, but this one was considered the most suited to the task: linear weighting of the NSD seems adequate and the attenuation of photons in absorbers follows a decaying exponential trend. Concerning the parameters a and b used, their ratio shifted and deformed the resulting iso- C surfaces without deforming them significantly, unless extreme values were chosen: the extremes that can be reached are simple iso-NSD surfaces ($b = 0$) or iso-flux (logarithmically deformed) surfaces ($a = 0$). The values $a = 1$ and $b = 3$ were used for this work.

Thyroid This detector is devoted to the measurement of contaminants in the thyroid with good accuracy and in the upper torso with good efficiency. As standard contaminant, ^{131}I with its line at 364 keV was chosen.

As shown in figure 5.27, the highest detection efficiency is achieved in front of the subject, where the layer of tissue shielding the thyroid is the thinnest. Given the thin absorbing layer interposed between thyroid and air, the NSDs in front of the phantoms are very low and were neglected during this analysis.

The placement of this detector was however heavily constrained by the cart and by the stretcher: the cart must stay on the side of the stretcher and the detectors hanging from the ceiling are used for other goals. In addition, the head of the detector cannot be placed too near the shoulder, since it would collide with tall subjects. As compromise, the detector was placed at about 45° from the middle plane of the subject: distant enough from the shoulder to avoid hitting the 99 percentile man, but as close to the middle plane of the subject as possible. The front of the detector is placed tangent to the surface corresponding to a flux of 10^{-4} cm^{-2} . The expected NSD at the same point is 15%.

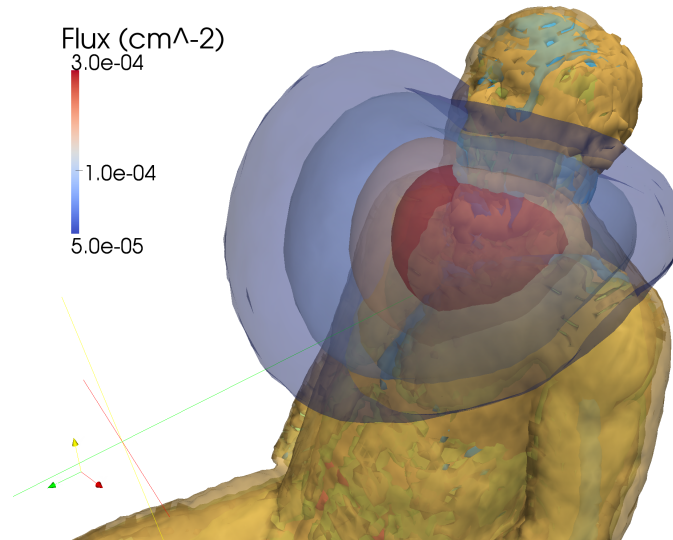


Figure 5.27: Iso-flux surfaces for the 364 keV energy line emitted by ^{131}I in the thyroid.

High-Efficiency for the Torso The second detector was devoted to the detection of the smallest possible amount of contaminants in the torso, therefore the standard deviation was not important. The detector was placed in the hole of the stretcher behind the back of the subject. Tall subjects have the detector in the lower part of the lungs or between lungs and liver, smaller subjects have the detector placed at the height of the lungs.

Gastrointestinal-Tract The third detector was meant to be able to estimate with good accuracy the activity of intakes through inhalation or ingestion: the target organs are lungs and GIT, plus the liver, an important organ due to biokinetic considerations (ICRP67; ICRP78).

Sources located in the three organs of interest produce the photon fluxes shown in figure 5.28. In the same figure green cubes mark the region of space defined by $NSD \leq 20\%$. As expected, lower-energy photons are more sensitive to the interposed medium and this green region is thinner. The fluxes behave the opposite: the iso-surfaces corresponding to the same values of the fluxes are found farther from the phantoms.

Since the values of NSD and average flux were not enough alone to define

the position, the value C was used (see figure 5.29). By combining flux and NSD, it was possible to align the detector to one of the new surfaces and to fix its position in the front-left part of the phantoms. The reason behind the shift toward the left part of the body can be easily explained: the GIT and the lungs are placed almost symmetrical to the sagittal plane but the liver resides on the right side: the place equidistant from the three organs taken into account is the left part of the body.

The resulting detector position is located in front-left of the subject, at the height of the diaphragm and at about 5 cm distance from the skin of the 99 percentile man. The attainable NSD is about 15% for 661 keV photons and 22% for 60 keV photons. The estimated photon flux is respectively $4 \cdot 10^{-5} \text{ cm}^{-2}$ and $3 \cdot 10^{-5} \text{ cm}^{-2}$. The flux originated from these organs evaluated at the position of the first detector (thyroid) is comparable, but the associated NSD is about double: 35% or more. The detector behind the subject, in close contact, receives a higher photon flux (10^{-4} cm^{-2}) but has an even higher NSD: over 50%.

Whole-Body The fourth detector was meant to be used for the generic detection of radionuclides dispersed in the whole body, including the legs and the muscles (for example, ^{60}Co and ^{137}Cs). In order to position the last detector, all the organs of each phantom were loaded with a 1460 keV source.

The shape of the iso-NSD and iso-flux surfaces indicated that the best position is in front of the subject, where the iso-NSD surfaces are flatter than the iso-flux surfaces. To better visualise the suitable region of space, a plot with the combined value C was generated (see figure 5.30). The optimal position cannot however be used, because the third detector already occupies that region and because it is important to have a detector on the opposite side of the body to compensate for lateral shifts of the subject. The third detector cannot be placed on the right side of the subject for the reasons already explained.

The last detector was therefore initially placed on the right side of the phantom, about symmetrically to the middle point of the first and third detectors. The distance from the subject was kept about the same as the

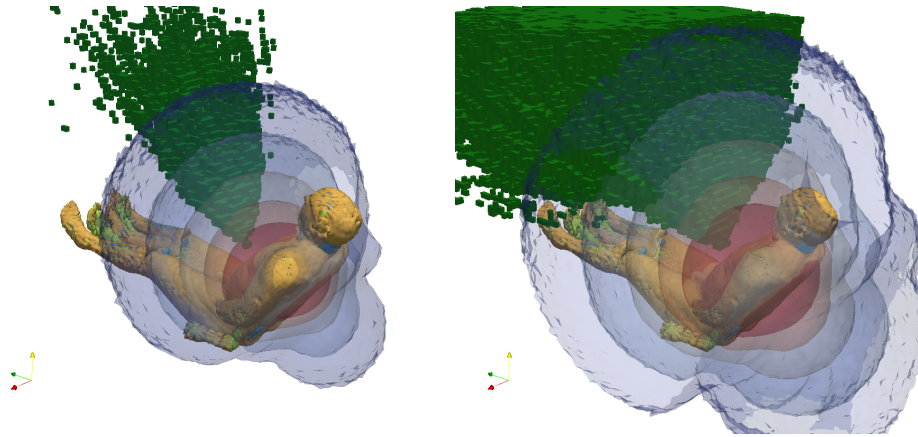


Figure 5.28: Iso-flux surfaces and region of space (green) defined by $NSD \leq 20\%$ when the sources are placed in liver, lungs, GIT. Results for 60 keV sources on the left, for 661 keV sources on the right. The iso-flux surfaces represent the same values in both figures.

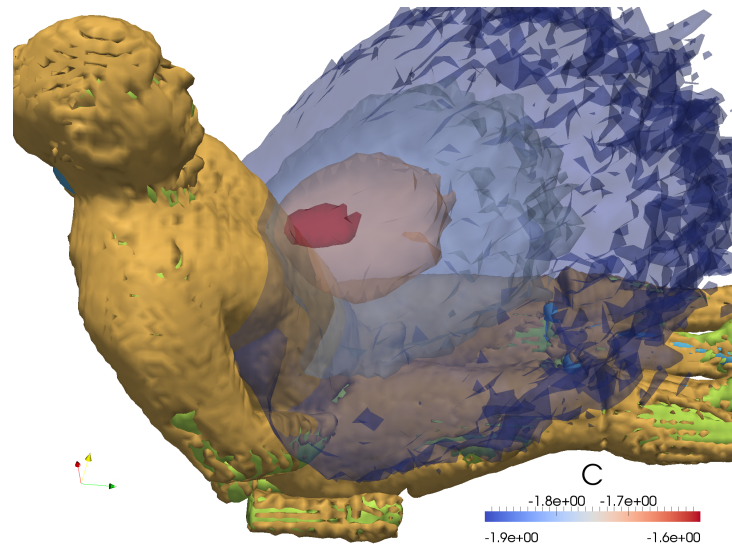


Figure 5.29: Surfaces corresponding to different values of C for 60 keV sources located in lungs, liver, GIT.

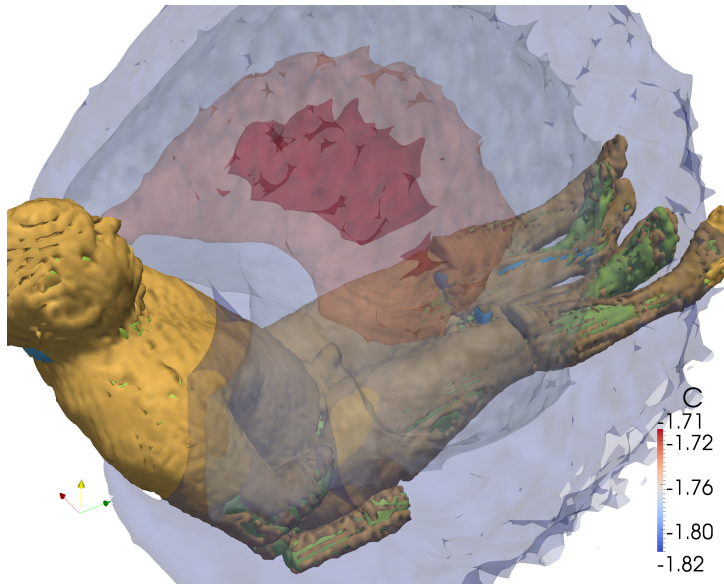


Figure 5.30: Surfaces corresponding to different values of C for 1460 keV sources located in the whole body.

third detector to achieve a similar photon flux, but the associated NSD was found to be too high, about 40%. A limit of 20% was desirable and the detector consequently placed farther away. The position with the highest flux for the given NSD was chosen, but nevertheless the photon flux dropped too much: from $3.5 \cdot 10^{-5} \text{ cm}^{-2}$ to $1.5 \cdot 10^{-5} \text{ cm}^{-2}$. Figure 5.31 shows the two positions and the corresponding iso-NSD surfaces.

To choose the final position, the regions of space with a given NSD threshold were plotted (see figure 5.32). The comparison of the volumes suggested the use of 30% as NSD threshold, instead of 20% and the detectors (third one and fourth one) were shifted accordingly.

Figure 5.33 show the final configuration of the detectors for WBC measurements. The associated photon flux is $2.5 \cdot 10^{-5} \text{ cm}^{-2}$ and the NSD 27%. Similar results are reported on Marzocchi et al. (2010b).

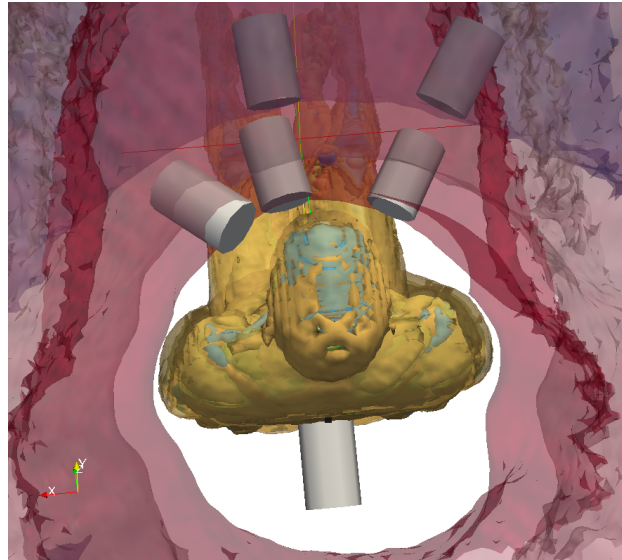


Figure 5.31: Position of the detectors for the first and second iterations and surfaces corresponding to different values of NSD (20%, 30% and 40%) for 1460 keV sources located in the whole body.

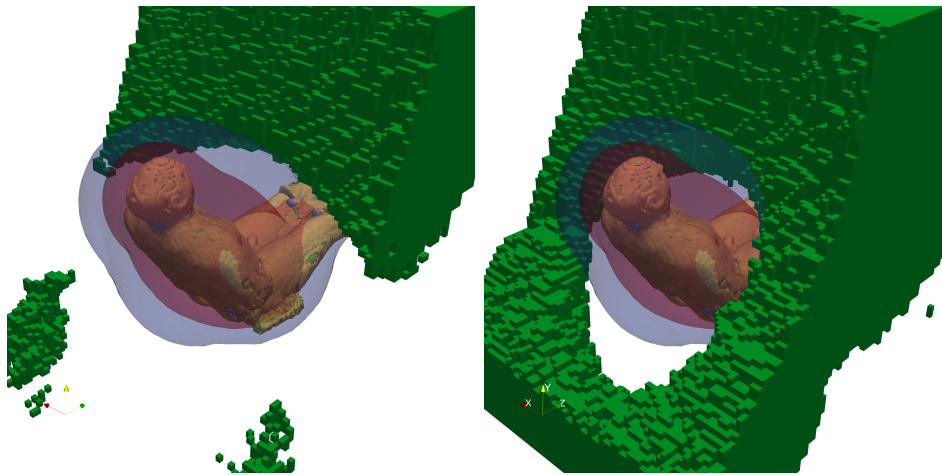


Figure 5.32: Region of space with $NSD \leq 20\%$ (left) or $NSD \leq 30\%$ (right) for 1460 keV sources located in the whole body. The surfaces represent the photon fluxes ($1.8 \cdot 10^{-5} \text{ cm}^{-2}$ and $3.2 \cdot 10^{-5} \text{ cm}^{-2}$) originated by the same sources.

5.6 Calibration of the New System

The new system was assembled and different tests were performed to check its capabilities. Since a detector has been unavailable for the last 5 months, no tests were yet performed with the full system.

Two sets of measurements are here reported: the measurement of a LLNL phantom loaded with different nuclides in lungs and the measurement of two uncontaminated subjects to estimate different MDA values.

5.6.1 Measurements of a LLNL Torso Phantom

The torso phantom available at IVM was used to perform an empirical calibration of the new system.

The phantom was placed on the stretcher in reclined configuration and the three available detectors (two hanging, one on a cart) were arranged in a mixed configuration: two were placed over the lungs, aligned as good as possible with the markings available on the phantom, one was placed in the hole available in the stretcher at the height of the lungs (see figure 5.34). Different sources were tested: ^{241}Am , ^{239}Pu , ^{235}U , ^{237}Np . The position of the detectors and of the phantom was checked after each measurement to make the values perfectly comparable.

The spectra were processed with *Genie-2K*: they were searched for peaks using a 2nd derivative algorithm and the area was calculated. A manual check of the peak fitting was performed to ensure accuracy of the results and to avoid missing peaks in multiplets. The peak areas and the corresponding uncertainties were transferred to Excel for further processing, where each value was scaled according to the emission probability of the energy line that originated it, as taken from DDEP, to calculate the transmission factors.

Among the results, it was found that the measurement of ^{237}Np was unreliable because the activity of the organ was too high and the resulting dead time of the detectors (over 20%) produced visible summation peaks and made the calculation of the efficiencies difficult. The ^{239}Pu measurements are also not reported because they require the correct estimation of the activity of ^{241}Am (originated by the decay of ^{241}Pu impurities) in the organ

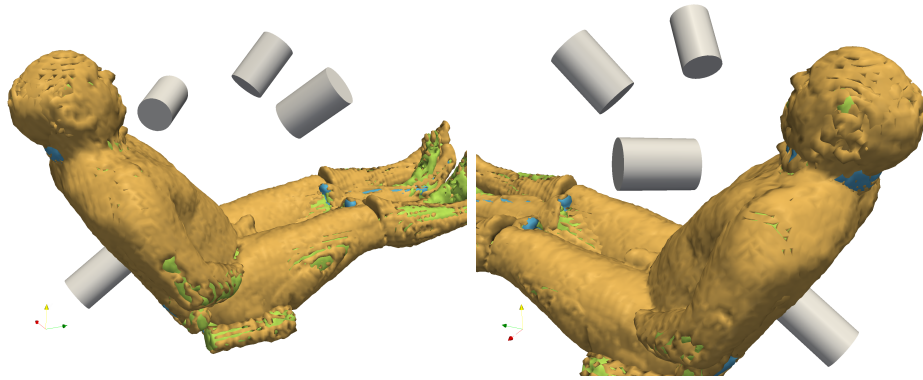


Figure 5.33: Final configuration of the detectors for WBC measurements.

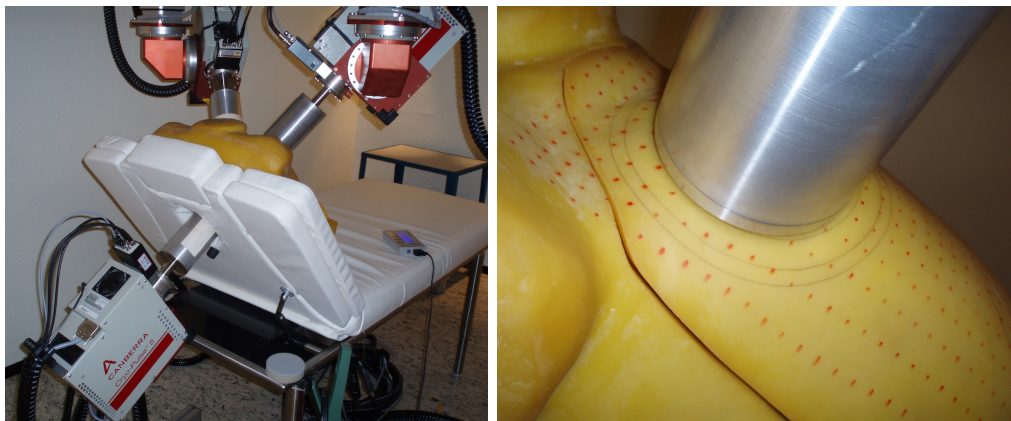


Figure 5.34: Configuration used for the calibration of the system for lung measurements. The picture on the left shows the detectors (from left to right) ‘back’, ‘front-left’, ‘front-right’. The picture on the right shows the detector ‘front-right’ and the alignment with the markings of the phantom.

Table 5.6: Transmission factors measured with the final system for two nuclides. The propagated uncertainties, calculated from the emission probabilities, areas of the peaks and source activities, are not reported because are dominated by the uncertainty on the activity of the source (5%).

Nuclide	Energy (keV)	Det. front-left	Det. front-right	Det. back
^{241}Am	16.1-17.8	$2.71 \cdot 10^{-4}$	$6.68 \cdot 10^{-4}$	$2.65 \cdot 10^{-5}$
	20.1-22.2	$7.93 \cdot 10^{-4}$	$1.84 \cdot 10^{-3}$	$1.55 \cdot 10^{-4}$
	26.3	$2.09 \cdot 10^{-3}$	$4.74 \cdot 10^{-3}$	$7.51 \cdot 10^{-4}$
	59.5	$5.03 \cdot 10^{-3}$	$9.04 \cdot 10^{-3}$	$3.65 \cdot 10^{-3}$
^{235}U	143.8	$4.71 \cdot 10^{-3}$	$7.67 \cdot 10^{-3}$	$3.94 \cdot 10^{-3}$
	163.4	$4.61 \cdot 10^{-3}$	$7.37 \cdot 10^{-3}$	$3.97 \cdot 10^{-3}$
	185.7	$4.48 \cdot 10^{-3}$	$7.17 \cdot 10^{-3}$	$3.88 \cdot 10^{-3}$
	202.1	$4.22 \cdot 10^{-3}$	$6.73 \cdot 10^{-3}$	$3.81 \cdot 10^{-3}$
	205.3	$4.31 \cdot 10^{-3}$	$6.84 \cdot 10^{-3}$	$3.79 \cdot 10^{-3}$

before obtaining correct calibration values. Table 5.6 summarises the results divided per nuclide and figure 5.35 shows the curve of the transmission factors (impulses reaching the crystal per emitted photon from the source).

5.6.2 MDAs for ^{241}Am and ^{235}U

The efficiencies previously calculated and two measurement of uncontaminated subjects were used to estimate the MDA attainable with the new system for ^{241}Am and ^{235}U in lungs.

The MDA was calculated only using the main energy line of each nuclide: 59.5 keV and 185.7 keV, respectively. The subjects chosen are colleagues and have an average amount of ^{40}K per kilogram significantly higher than the reference man: at least 70 Bq/kg, to be compared with the 60 Bq/kg usually recorded at IVM. The total ^{40}K activity ranges from 5 kBq to 7 kBq. The measurements were performed in the reclined configuration and the detectors in front of the lungs were placed in a position corresponding to the previous calibration with the LLNL phantom. The detector behind the back was used once in the hole behind the subject and once near the liver to have a second

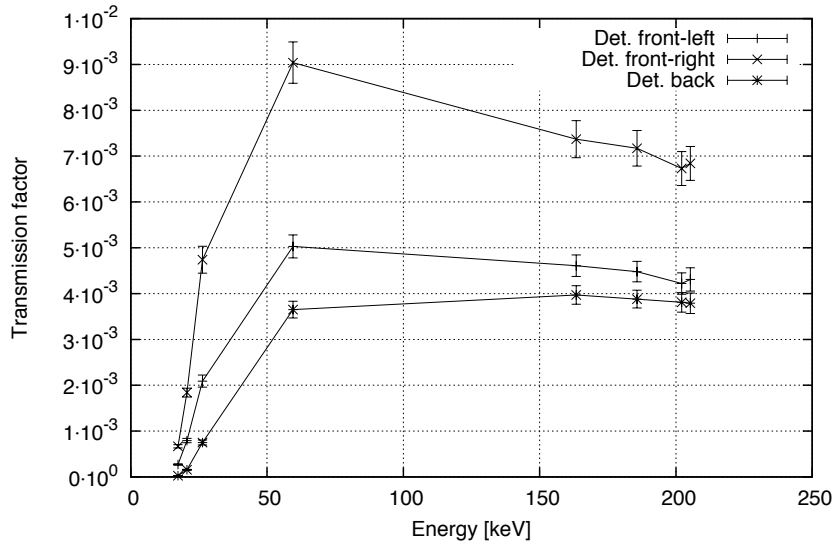


Figure 5.35: Transmission factors for sources in lungs.

value useful for future calculations. The values for the first two detectors are therefore averaged. The measurement time used is 2000 s, the width chosen for the ROIs is 2.5 FWHM and each background region is 1.25 FWHM wide.

Table 5.7 shows the MDA values calculated according to the latest standards (ISO). As expected, the MDAs for the ^{241}Am source are comparable with the values previously calculated with simulations (see section 5.3.1). The higher MDA for the detector over the left lung compared to the value for the other lung is also expected, due to the different mass of the organs and the resulting detection efficiencies.

The MDA for ^{241}Am is not significantly improved by the contribution of the detector behind the back: the number of photons reaching the crystal through the entrance window is limited because the torso wall is thick and the photons impinging on the lateral sides are significantly attenuated by the support of the crystal. As result, the addition of the third detector lowers the MDA by only 0.2 Bq. The values for ^{235}U are different: the addition of the third detector can lower the MDA by about 14% compared to the value obtained for the two detectors on the front. As conclusion, the fourth detector can be safely placed over other organs also during PBC measurements of the lungs, for example near the liver: the different detectors would have

Table 5.7: MDA values calculated for two different nuclides dispersed in the lungs. The uncertainties on the efficiencies (5%) and the uncertainties on the number of background counts ($\sqrt{N-2}$) were used to calculate the uncertainties on the MDA values.

Nuclide	Detector	Efficiency ($\text{Bq}^{-1}\text{s}^{-1}$)	Background	MDA	
				(Bq)	Uncert.
^{241}Am (59.5 keV)	Front-left	$1.81 \cdot 10^{-3}$	75	11.2	13%
	Front-right	$3.25 \cdot 10^{-3}$	90	6.8	12%
	Back	$1.31 \cdot 10^{-3}$	79	15.9	12%
	Both front	$5.05 \cdot 10^{-3}$	165	5.8	9%
	All	$6.36 \cdot 10^{-3}$	244	5.6	7%
^{235}U (185.7 keV)	Front-left	$2.56 \cdot 10^{-3}$	89	9.6	12%
	Front-right	$4.09 \cdot 10^{-3}$	86	5.9	12%
	Back	$2.21 \cdot 10^{-3}$	63	9.5	14%
	Both front	$6.64 \cdot 10^{-3}$	175	5.1	9%
	All	$8.86 \cdot 10^{-3}$	238	4.4	7%

significantly different detection efficiencies for the different source organs and the resulting matrix of direct- and cross-efficiencies could be used to locate contaminations with one single measurement.

Chapter 6

Application to Routine Measurements

This chapter is divided into two parts. In the first one, the goals and concepts behind the software developed to handle the new PBC/WBC HPGe system are described, using the point of view of the user as guide. The algorithms used are described in Appendix A. In the second part of the chapter, the first applications of the new system to routine measurements are described: the measurement of two subjects potentially contaminated with ^{210}Pb and the calibration with an IGOR phantom.

6.1 Software Design

6.1.1 Shortcomings of the Old Platform

The IVM at KIT uses a custom platform to handle both PBC and WBC measurements. The software manages almost all the steps of the routine, from the operation of the detectors to the analysis of the spectrum and the final storage of the data. A database connected to this software stores the spectra of all past measurements and the historical data of the subjects measured with the system.

A fundamental issue of the old database is, however, the lack of flexibility, since the designer of the database, in the early '90s, did not plan the expansion

of the system or the increase of resolution: for example, each spectrum can have only 256 channels. Changing this value is not feasible: the spectra from the four detectors of each system (four NaI(Tl) in the WBC or two phoswiches with two crystals each in the PBC) are joined and the final series of 1024 channels is saved into the database. Implementing the handling of HPGe detectors is impossible, even if ‘tricks’ were to be used: each spectrum from the new system contains 8192 channels.

Further limitations of the old software consist in the routines used for the detection of nuclides: spectra from scintillators have broad peaks and not many of them can be isolated in a given spectrum, therefore a manual iterative approach for the identification is feasible. HPGe detectors are considerably different and can identify even hundreds of peaks per spectrum: for example, the spectra measured with the ^{237}Np lungs contain over 50 peaks each. This is an advantage of the HPGe detectors, especially in non-trivial contamination cases, but an automated identification algorithm is required. The old software could have the new algorithms implemented, but the old database would have had to be changed, since it offered only fields for the input data and final results, but nothing to specify the algorithms.

To overcome the limitations of the old database and to improve and adapt the user-interface to the new analysis routine, a software was developed anew.

6.1.2 Requirements of the New Platform

The old software is divided in different modules: the main one handles the connection to the database and the retrieval of the subjects’ data, the other two modules handle the measurements of the PBC or WBC systems. This division has advantages: the algorithms used for the phoswiches or for the NaI(Tl) scintillators can be different and measurements in the two rooms can be running at the same time.

After consulting the main developer of the current software, it was decided to produce a new module for the old platform, so that the module handling of data of the subjects could be kept. The new one should be able to operate both independently and in association with the old platform and would use a

new database structure to store the different input and output data. The old software will be modified to cooperate with it.

The minimum features required in the new module are the following:

- choice of the detector(s) to use for the measurement: if some of them are unavailable due to repairs, the system must remain operational;
- choice of the measurement configuration and of the analysis routine: the new detector are versatile, different measurement goals are possible (see chapter 5); the software must use different calibration data for each goal and set-up;
- simplified energy calibration routine: both the old systems were operated with analog electronic modules, the new HPGe are set-up and tuned only digitally, making the automation of the process possible;
- based on the configuration routine and on the characteristics of the subject, proper calibration data have to be selected automatically;
- each measurement has to be associated with a specific operator, as required by the quality management (“QM”).

The requirements for the new database are the following:

- ability to store the spectra in the original ‘CAM’ format (specific to Canberra) and in a raw format, better suited to processing with other softwares without *Genie-2K* software ;
- tracking of the results back to the source and vice-versa: to comply with the regulation for QM, the user must be able to later replicate every analysis and obtain the same results, therefore routines names and parameters must be stored in the database;
- expandability of the system: in case of an enhanced system with more detectors or more channels, the database must not need to be redesigned;
- storing of the data (calibration, results) in a format compatible with other software (for example, the database module of the old software).

6.1.3 Structure of the Software and Operation

The software is designed to be as easy as possible for the final user and is arranged around three main windows.

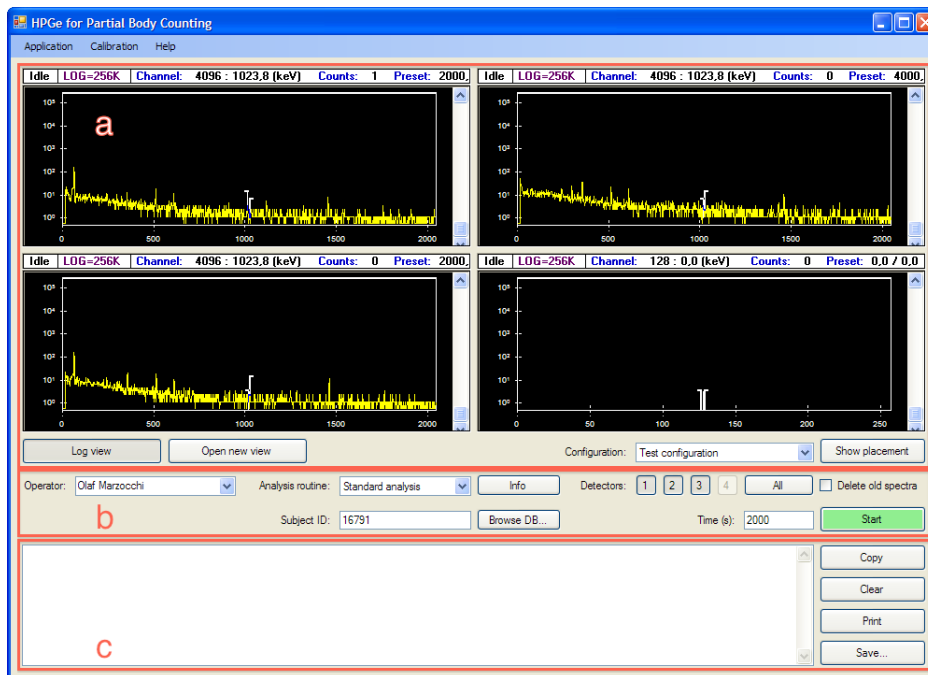


Figure 6.1: Main interface of the new software. Region (a): display information about the spectra and the configuration of the detectors; region (b): set-up of the settings for the measurement; region (c): display of the output.

Main Window The content (see figure 6.1) is divided in three parts: overview, commands, results. The upper part shows the four spectra of the four detectors, just to give an overview of the main peaks. No zoom feature is provided, but it is possible to change the vertical scale from linear to logarithmic. If a more detailed inspection is desired, a new window can be opened with the appropriate button.

The middle part contains the buttons used to set-up and start the measurements: operator (required by the QM), analysis routine used to process the data, identification code of the subject or sample being measured, detector(s) used, duration of the measurement.

The last part of the main window shows selected output of the calculations and log messages useful to keep track of the actions performed by the software. It is also possible to save the output and print it.

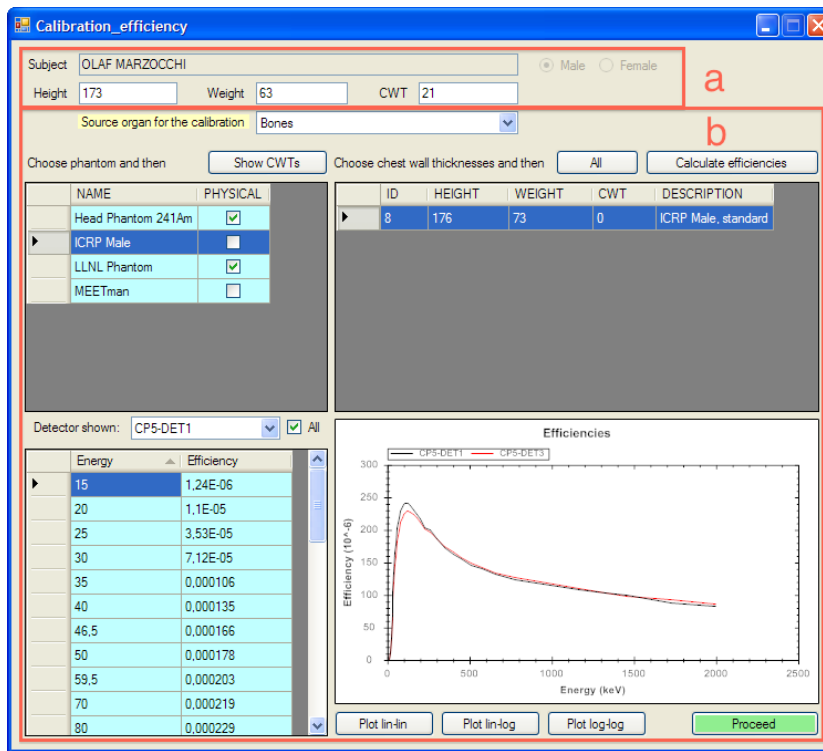


Figure 6.2: Window used for the efficiency calibration in the new software. Region (a): display information about the subject being measured; region (b): information about the phantoms used and final set of calibration point (list and graphical representation).

Efficiency Calibration This window (see figure 6.2) is shown if a measurement is successful and the user chooses to proceed with the analysis (as opposed to only store the spectra). The upper part shows the data about the subject, as taken from the database of the old platform, the remaining part of the window is used to select and generate the calibration curves. In case of the measurement of samples, the fields are empty.

The first table shows the phantoms available in the database and their type: physical or computational. The user selects at least one of them and the correspondent sets of calibration data are shown on the right. This two-step procedure is required because some phantoms may have different calibration sets for different physical parameters such as CWT or size and one single list may grow too big.

Once the user selects the desired calibration sets, the software calculates the final curve using the CWT of the subject to interpolate the available data. Measurements of some organs, such as whole-body, knee or skull, will have only one calibration set because the CWT does not apply and no interpolation will be performed.

The final result is a series of efficiency points, detector-dependent, shown in the graph pane on the lower-right part. The graph can be zoomed and the visualisation scale changed with the use of the mouse. If the user modifies manually the points (e.g. to correct them or to experiment with them), a warning is issued in the upper part of the window: the database cannot store anymore the input data used to obtain the final curve, only the final points are saved in the database.

Energy Calibration The energy calibration is a step rarely performed with the digital electronics used for the new HPGe detectors: the tests showed in two months deviations of less than 1%. The calibration process was however incorporated to simplify the work of the operators. The goal is to obtain spectra with a specific channel width (0.25 keV) by changing the gain of the amplifier. By having constant channel width, the set-up of the MCNPX input files is simplified and the measurements are comparable channel-by-channel with the simulations.

Given the proven linear response of detector and digital electronics, a simplified calibration procedure with only three user-defined peaks was implemented. The user must first optimise the pole-zero settings with an high-energy source to ensure the best shape of the peaks, then place sources in front of the detector (e.g. ^{241}Am , ^{137}Cs and ^{60}Co are recommended) at an appropriate distance to keep the pile-up low and finally start a short measurement. The software determines the position of the three highest peaks in the spectrum and calculates new values for the gain of the amplifier. At the end, the final settings are stored in the database for future reference. Figure 6.3 shows the layout of the different controls.

Various Other minor windows, not shown here, are:

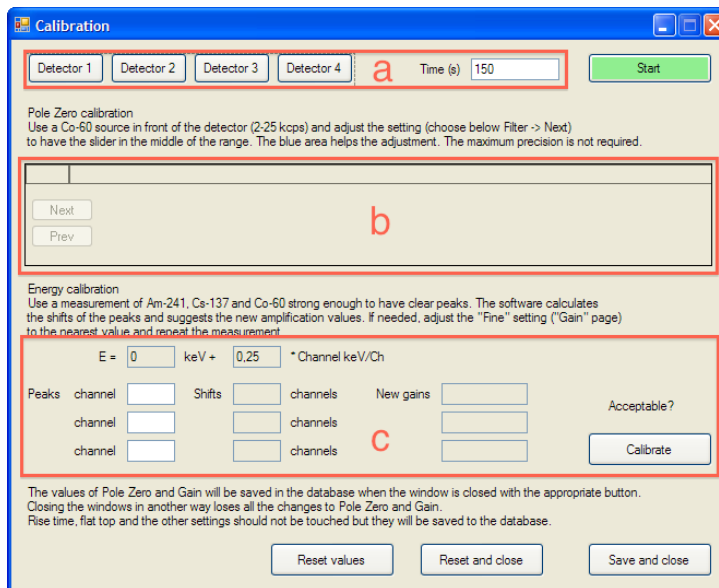


Figure 6.3: Window used for the energy calibration in the new software. Region (a): select detector and measurement time; region (b): panel used to alter the detector settings; region (c): peak position, measured offsets and new values for the gain.

- preferences, where the default values of different parameters can be set;
- end of measurement window, where the user can decide whether to discard the measurement, to save it to the database, or to proceed with the analysis after entering comments and other required information (type of spectrum, goal of the measurement);
- selection of the subject from the database, if the software is used stand-alone. If it operates as module of the pre-existing platform, the identification is obtained automatically;
- selection of previous measurements or analyses to execute them again with different calibration data.

More information about the software is available in appendix A, where some algorithms used in the software are described.

6.2 First Applications of the New System

A real application of the detectors to routine has not yet started: since the building of the new mechanics, one detector has always been unavailable due to repairs and the system was operated for tests with only the two or three remaining detectors. This work describes therefore only two applications of the new system: the measurement of two subjects potentially contaminated with ^{210}Pb in bones and the initial calibration for WBC of the complete system using the IGOR phantom.

6.2.1 Measurement of Potential ^{210}Pb Contaminations

On the 11th of February 2011 two subjects were measured in the PBC chamber at IVM to check if they were contaminated with ^{210}Pb . Both subjects worked in a water-treatment plant and they may have been exposed in the past to significant concentration of radon in air. Radon is a gas, but its decay products are solid and partly deposited inside the body. A method previously used to assess past radon exposures is the detection of the decay product ^{210}Pb , located mostly in bones and liver. Being a low-energy emitter, in-vivo measurements are performed preferably on the skull or knees, as described in ICRP78 and Eisenbud et al. (1969); Muikku et al. (2003); Wahl et al. (2000).

The new HPGe system was not yet complete, due to a missing detector, so a counting geometry not previously planned was used: two detectors were placed on the sides of the skull, where the skin is the thinnest, one was placed exactly behind the head (see figure 6.4). The position was chosen with the help of one simulation using the reference ICRP phantom. This phantom was chosen instead of MEETMan because it reproduces an average male, while MEETMan reproduces a subject bigger and heavier.

Each subject was asked to lay on the stretcher in reclined position and one measurement 2000 s long was performed. Since there are no background lines in the 43-50 keV region, no natural (room) background subtraction was performed. The ROI was centred on 46.5 keV (main emission line of ^{210}Pb) and 2.5 FWHM wide (11 channels, 45-47.5 keV), the local background continuum was estimated linearly, as suggested in the standards (ISO), using



Figure 6.4: Photos of the set-up used to perform the two ^{210}Pb measurements. The plastic foil was used to avoid contamination of the detector window.

Table 6.1: Results (MDAs and activities) obtained from the measurements. The threshold refers to the decision threshold, the MDA is the minimum reliably detectable activity. See section 3.5 for more information. The detector on the left of the first subject detected a number of counts higher than the expected value for the null hypothesis.

Subject	Detector	Net	Bkg.	Efficiency	Activity (Bq)	Threshold (Bq)	MDA (Bq)
One	Back	41	40	$2.62 \cdot 10^{-5}$	-57	302	656
	Left	56	28	$2.32 \cdot 10^{-5}$	543	285	629
	Right	41	37	$2.28 \cdot 10^{-5}$	7	334	727
	All	138	105	$7.22 \cdot 10^{-5}$	156	177	374
Two	Back	18	12	$2.62 \cdot 10^{-5}$	90	162	386
	Left	22	22	$2.22 \cdot 10^{-5}$	-17	245	562
	Right	30	30	$2.28 \cdot 10^{-5}$	-41	291	659
	All	70	64	$7.22 \cdot 10^{-5}$	14	134	290

the regions 43-45 keV and 47.75-50 keV (5 channels each). Figure 6.5 shows the spectra.

The calibration, not only for the 46.5 keV energy, but for the whole energy range of the detectors (15-2000 keV), was obtained numerically, using MCNPX with the reference male phantom from ICRP. The calibration data are referred to the complete skeleton considered homogeneously contaminated. The final efficiency curves are shown in figure 6.6.

The calculations were performed using the formulas specified by the international standards and the values are reported in table 6.1. The results were not scaled to the size of the subjects or of their heads, because, as already discussed, the detection efficiency for low-energy emitters depends almost exclusively on the exposed surface. Other parameters such as bone thickness could not be estimated and their role has yet to be investigated.

Some conclusions can be inferred from the results. First of all, the MDAs are comparable with the values expected from table 5.1, proving the quality of the models of the detectors and of the method used to define the counting configurations. More precisely, the MDA is proportional to the counting efficiency and to the photon yield of the decay process. The nuclide ^{241}Am ,

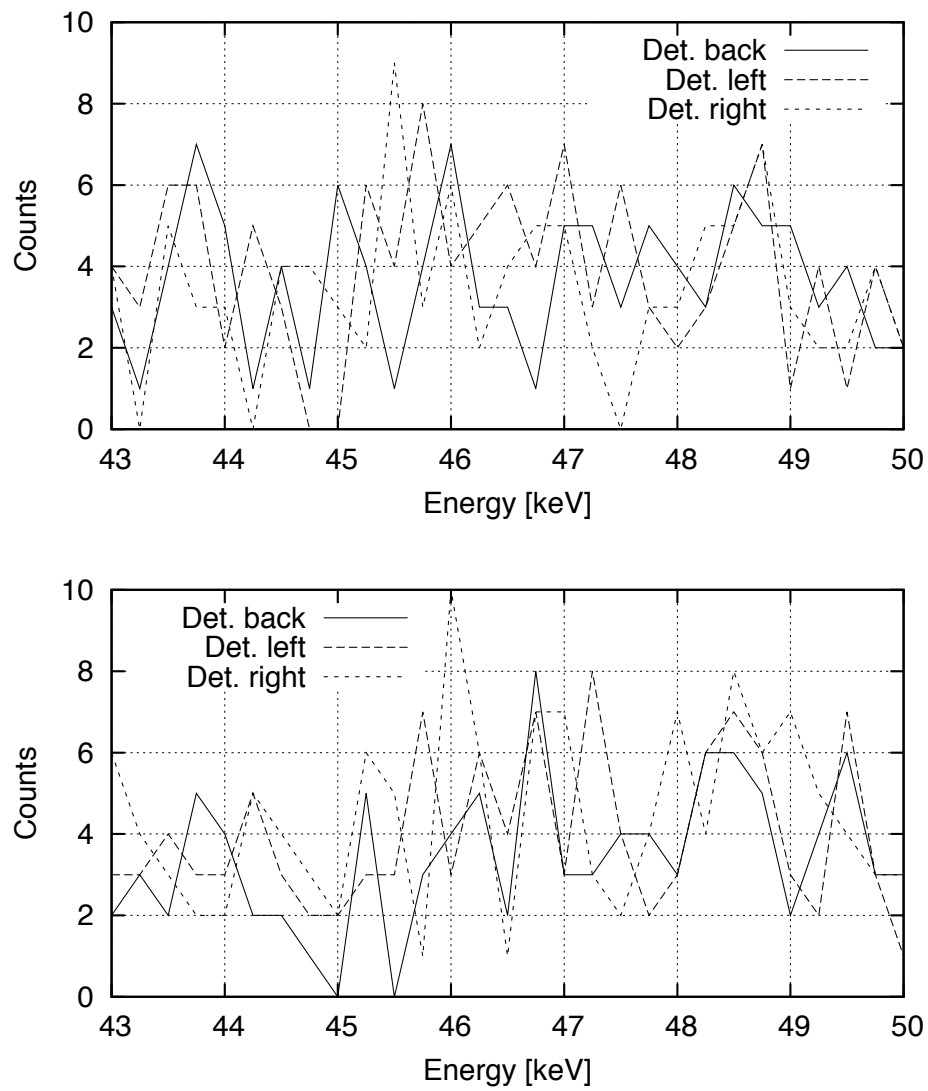


Figure 6.5: Spectra obtained from the measurements of the two subjects, first one on top and second one bottom. The ROI ranges from 45 keV to 47.5 keV, the other channels are used as background.

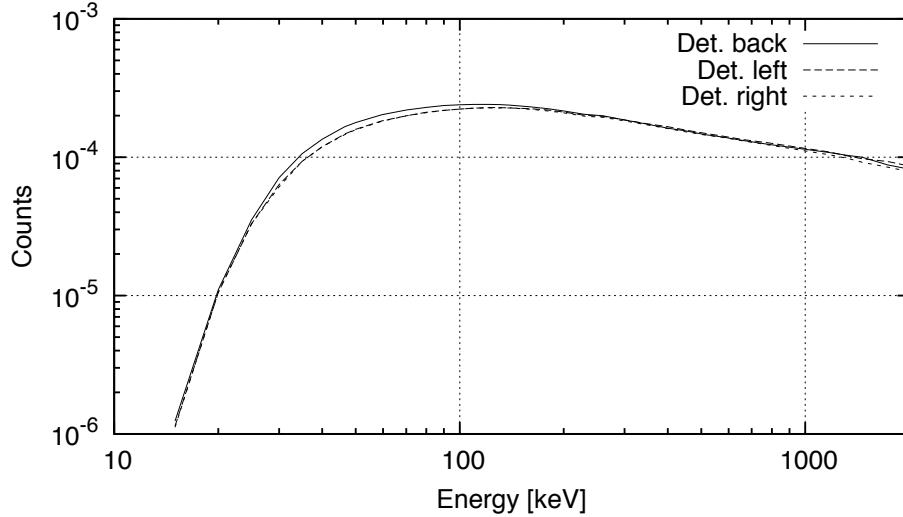


Figure 6.6: Calibration curves obtained for the three detectors used for the measurement of the skull.

used for the definition of the set-ups, emits gammas at 59.5 keV, ^{210}Pb at 46.5 keV. Since the detectors are in close contact to the source and the absorption in the entrance window is negligible (according to the simulations and to the manufacturer data), the intrinsic detection efficiency can be considered as first approximation constant, only the yield in photons per decay changes. In table 5.1 the expected MDA is about 70 Bq, the MDA for ^{210}Pb can be calculated as 590 Bq from the ratio of the yields:

$$MDA_{210\text{Pb}} = \frac{y_{241\text{Am}}}{y_{210\text{Pb}}} MDA_{241\text{Am}} \quad (6.1)$$

Concerning the goal of the measurements, the aggregate values (‘All’ detectors) show the lack of any measurable or detectable activity in both subjects: the values fall below the decision threshold. The only exception is the detector placed on the left of the skull of the first subject, with a value of activity between the decision threshold and the MDA. The values for the other two detectors are however significantly lower and the aggregate value can be considered more reliable.

Another interesting fact is the significantly higher (64%) number of counts in the background regions for the first subject, compared to the results of the

Table 6.2: Peaks producing Compton in the low-energy region of the spectrum. The uncertainties are expressed in percent between parentheses.

	Subject one	Subject two	Difference
Bkg. ^{210}Pb	105 (10)	64 (13)	64%
Peak 511 keV	327 (7)	206 (13)	59%
Peak 1460 keV	834 (3)	788 (4)	6%

second one. A first check was performed by considering the ^{40}K peak, but the difference among the two subjects is not enough to explain the increase in the low-energy background (see table 6.2). A second peak considered is the 511 keV annihilation peak, originated by β^+ decays of radionuclides in air, sometimes abundant at IVM, even after air filtration. The two contribution together can explain with good approximation the increase of the continuum background in the low-energy region.

As conclusion, it must be noted that the MDA in the lowest energy region is greatly affected not only by the contribution of higher-energy radionuclides located in the subject being measured (mainly ^{40}K), but also by the environment. Its relative importance is significant, also if the measurement is performed in a highly shielded chamber (in this case, the reduction of background counts is one hundred compared to the external environment).

6.2.2 WBC Measurements with an IGOR Phantom

The new system, complete of the four detectors, was used to measure the IGOR phantom in different configurations. The goal was to check the final mechanics installed in the room and to obtain a first set of calibration data, to be compared with the simulations and computational calibrations that will follow.

The IGOR phantom provides in six different configurations from P1 to P6, corresponding respectively to subjects of 12 kg, 24 kg, 50 kg, 70 kg, 90 kg and 110 kg. Each one can be arranged in three different positions: standing, sitting, sitting-bending. In this case, none of them corresponded exactly to the reclined set-up used in the new body counter, therefore the sitting

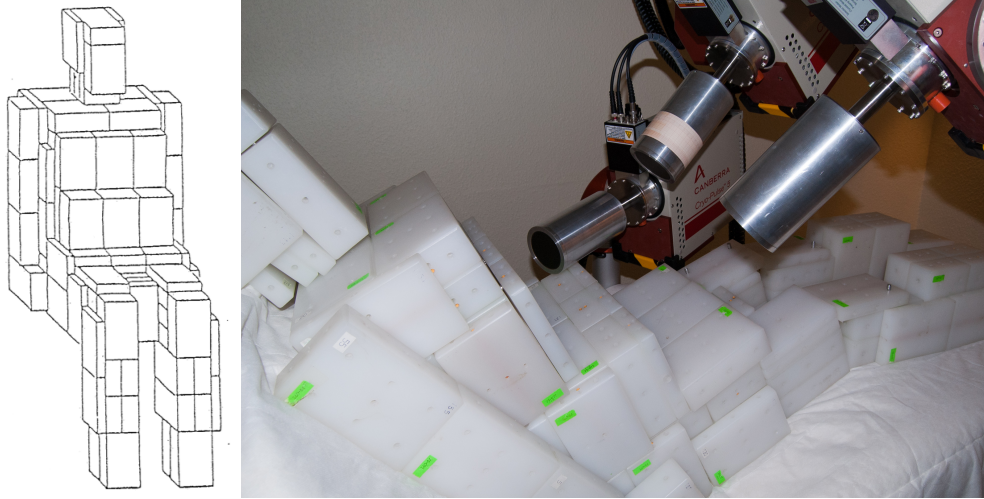


Figure 6.7: IGOR P6 in sitting (left) and reclined (right) configuration.

arrangement was used as basis to build the phantoms on the new reclinable stretcher. Only the three heaviest configurations were used, P4 to P6, since they represent the majority of the subjects measured at IVM. The changes from the original set-up involved the modification of the hips and upper legs to reproduce the bending of the subjects in reclined position and the change in orientation of some bricks in the lower-torso. The torso was also built not as a single block, by connecting all the bricks together, but as layers of bricks: upper torso, middle torso, lower torso. The advantage was the easier positioning along the reclined support, but the resulting shape was that of a staircase. A comparison of the sitting and reclined shape of IGOR P6 is shown in figure 6.7, where the ‘staircase’ effect is also visible.

The positioning of the detectors as previously defined with MCNPX simulations for WBC measurements was not possible and some changes had to be applied due to limitations of the mechanics. More specifically, the two detectors hanging from the ceiling were placed 10 cm lower. In this configuration, all the detectors reached the end of the operating range: the detector on a cart behind the subject the lowest position and the other three the highest position. In the future, tests with the detector behind the back placed in a higher position will be performed to evaluate advantages and disadvantages of the change. The detectors in their final configuration are

shown in figure 6.8 and 6.9 (the latter is a panorama image showing the whole room).

The correct rotation of the detectors was checked with the controller developed for this application, shown in figure 6.10. The position of the carts in the room and of the hubs along the rails on the ceiling was measured with a laser device. The final positions were marked with stickers to allow the future alignment of the detectors also without measuring instruments.

The measurements of the different phantoms and sources were performed for P5 and P6 separately, 4 000 s per nuclide per phantom with the exception of ^{40}K , measured for 40 000 s. IGOR P4 was an exception, being measured with less activity (about half) but longer, 80 000 s. The resulting peaks are better defined and future measurements will follow the same procedure, since it is faster and requires less movements of the bricks for the loading, thus making the configurations more reproducible. This solution has only one disadvantage: peaks from ^{133}Ba and ^{137}Cs in the 30-36 keV region are overlapping and cannot be correctly resolved. This was not an issue for WBC because the analysis was performed starting at 81 keV: low-energy peaks (below 50 keV) cannot be reliably detected with detectors far from the source. A special test was performed with IGOR P5: the detectors hanging from the ceiling were shifted 5 cm from the original position along the head-feet direction to study the effect of errors connected to their positioning. All the other coordinates and angles were kept constant.

The resulting detection efficiencies are reported in figure 6.11, 6.12 and 6.13.

The graphs show all the nuclides at the same time, but the energy lines from the different nuclides are naturally sorted by energy, therefore the part below 400 keV of the curves belongs to ^{133}Ba , follow the ^{137}Cs peak, the ^{60}Co duplet and the ^{40}K peak. The uncertainties are calculated from the counting statistics and from the uncertainty on the activity of the sources (5%). In case of ^{40}K , the additional uncertainty from the subtraction of the background is taken into account.

Detectors 3 and 4, as expected, have the lowest detection efficiencies, being them focused on its homogeneity and not on its magnitude. The 5 cm shifts of these two detectors in the head-feet direction proved almost ineffective:



Figure 6.8: Detectors in the final WBC configuration. The detectors are numbered starting from the detector behind the back (det. 1), then detector on the left (det. 2), front-left (det. 3) and front-right (det. 4).



Figure 6.9: Detectors in the final WBC configuration. Panorama obtained from multiple images.



Figure 6.10: Controller used to position the detectors.

the variation of the detection efficiency was smaller than the magnitude of the counting uncertainties.

Detector 1, being in direct contact with the phantom, achieves the highest efficiency but there is an issue for the P4 case, where the ^{40}K peak has an efficiency almost as twice as high as expected. Being all the nuclides measured at the same time, the change cannot be explained by errors in the counting time. The activity loaded in the phantom is also easily calculated (see table 6.3), and cannot be underestimated, since only two rods, over 71 total, could be replaced by higher-activity ones. An error on the estimation of the natural ^{40}K background would also affect the results at most 10%, therefore another explanation has to be found. A possible one concerns the position of the radioactive rods: being the phantom built as different layers of bricks, it is possible that some of the rods, placed near the border, slid towards the bottom and were left naked, without polyethylene scatterer around. The issue will be investigated with further measurements of the P4 phantom.

The results show also the variation of efficiency as function of the phantom size. It can be noted that detector 3 and detector 4 have detection efficiencies almost constant from P4 to P6, while detector 1 and detector 2 lose up to 20% from P4 to P6. As expected, the lower-energy region of the spectrum, below 500 keV, is affected the most. The results from the tests with the detectors shifted 5 cm from the original position are not reported because a the shift produced variations smaller than the total uncertainties. This suggests that

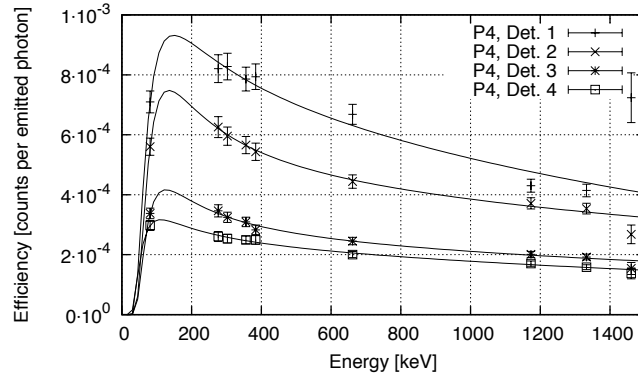


Figure 6.11: Efficiencies calculated for the IGOR P4 phantom.

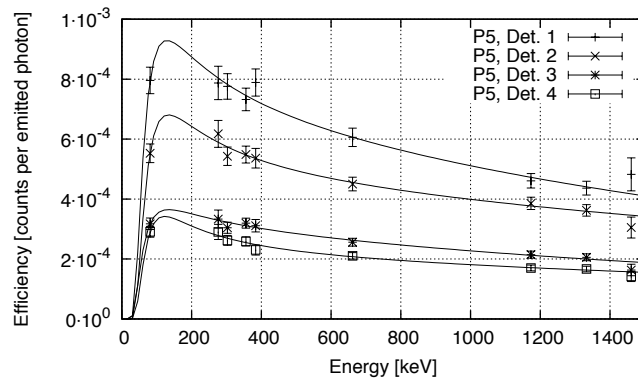


Figure 6.12: Efficiencies calculated for the IGOR P5 phantom.

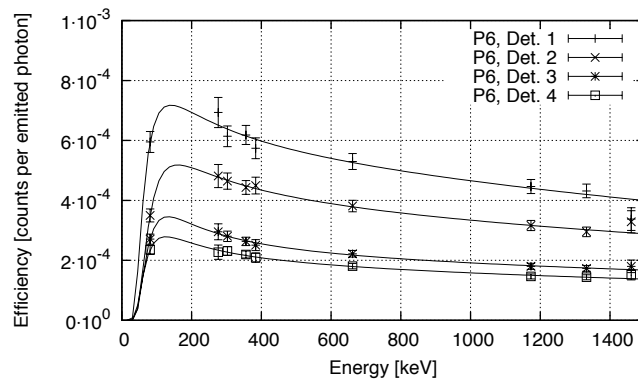


Figure 6.13: Efficiencies calculated for the IGOR P6 phantom.

Table 6.3: Nuclides and corresponding activities used for the measurements of the different phantoms.

Phantom	Nuclide	Half rods	Full rods	Total activity (Bq)	Meas. time (s)
P4	^{133}Ba	2	69	2 356	80 000
	^{137}Cs	2	69	4 206	80 000
	^{60}Co	2	69	993	80 000
	^{40}K	2	69	2 807	80 000
P5	^{133}Ba	42	140	5 428	4 000
	^{137}Cs	42	140	9 683	4 000
	^{60}Co	42	140	2 283	4 000
	^{40}K	65	144	7 074	40 000
P6	^{133}Ba	42	140	5 428	4 000
	^{137}Cs	42	140	9 683	40 000
	^{60}Co	42	140	2 283	4 000
	^{40}K	65	182	8 598	40 000

small positioning errors will not affect the results of routine measurements, where the counting time is only 300-600 s.

Chapter 7

Overview and Conclusions

In this work the redesign, building and testing of a new body counter was described. The old system, arranged in fixed or semi-fixed configuration, was replaced with a new one made of four HPGe detectors with significantly more degrees of freedom. In addition, the old analog electronic modules were upgraded to digital ones, able to achieve comparable or better performances while reducing the amount of maintenance required to calibrate the detectors.

Being the mechanics of the new detectors completely redesigned, new measurement configurations for partial-body and whole-body counting were defined using Monte Carlo simulations. This step required a characterisation of the detectors and the building of accurate MCNPX models and the results were validated with measurements and simulations of the LLNL torso phantom.

The definition of the configurations was performed for two different arrangements: flat stretcher and sitting set-up. The MDA for the two cases were comparable, with the exception for liver measurements, but the sitting set-up would give more freedom in the positioning of the detector and was ultimately chosen. A stretcher with the ability to assume a reclined position was chosen from a catalogue and modified according to preliminary testing.

The new system could not be operated with the pre-existing software platform due to the design choices performed by the original developers, therefore a new software was produced, able to operate either standalone or as module

of the old platform.

Concerning the tests of the final system, some of the new detectors had to be brought to the manufacturer for repairs and maintenance, therefore the number of tests performed was limited. The first test here reported concerns the estimation of the MDA for low-energy sources dispersed in lungs, being this the most common type of measurements performed in the PBC at IVM. The results proved the quality of the system: the MDA calculated for the detectors placed in front of the lungs alone is comparable or lower (5.8-11.2 Bq) than the values attainable with the old system (10-20 Bq), even if the detection efficiency is constrained by the smaller crystal size.

Real-world measurements of low-energy emitters in subjects were also tried, but no contamination was found. The MDA calculated for this case were comparable with the values expected from the simulations, proving again the quality of the models and of the method used.

The test of the new system with the IGOR phantom was heavily affected by the time available and this work can report only some preliminary results. The data collected show already that the goals of the WBC configuration were achieved: detectors 1 and 2 present higher detection efficiencies, but are more affected by the shape and size of the phantom. Detectors 3 and 4 collect less photons but present smaller variation in the detection efficiency.

As next steps, further measurements will be performed with the new system to test some additional measurement scenarios. The software will be perfected in cooperation with the operators of the IVM and with the help of their feedback. As soon as the software is ready, the system will gradually replace the phoswich detectors for routine measurement or part of it. The quality management documentation and the accreditation for quality management will follow.

Appendix A

Software Developed

This appendix describes some of the algorithms used in the new software for the handling of the HPGe detectors and the structure of the database used to store the input and output data of the measurements.

A.1 Database

The database designed for the the software is divided into 15 main tables and 5 additional tables to connect their data. An overview of the structure is given in figure A.1 and the description of the tables follows.

Measurements This is the main table where the results of the measurements (the single spectra) are stored. Two field are provided for the date and the operator who inserted the record, as required by the QM. These two fields are also found in most tables and they will not be discussed further. Each record contains the spectrum in raw format (binary, each channel is a 32 bit integer) and also the CAM file generated by *Genie-2K*, since it contains all the parameters used for the measurement and the settings of the detector. Additional fields are provided to identify the measurement configuration, the source and also the detector: each real measurement produces as many records as the number of detectors used.

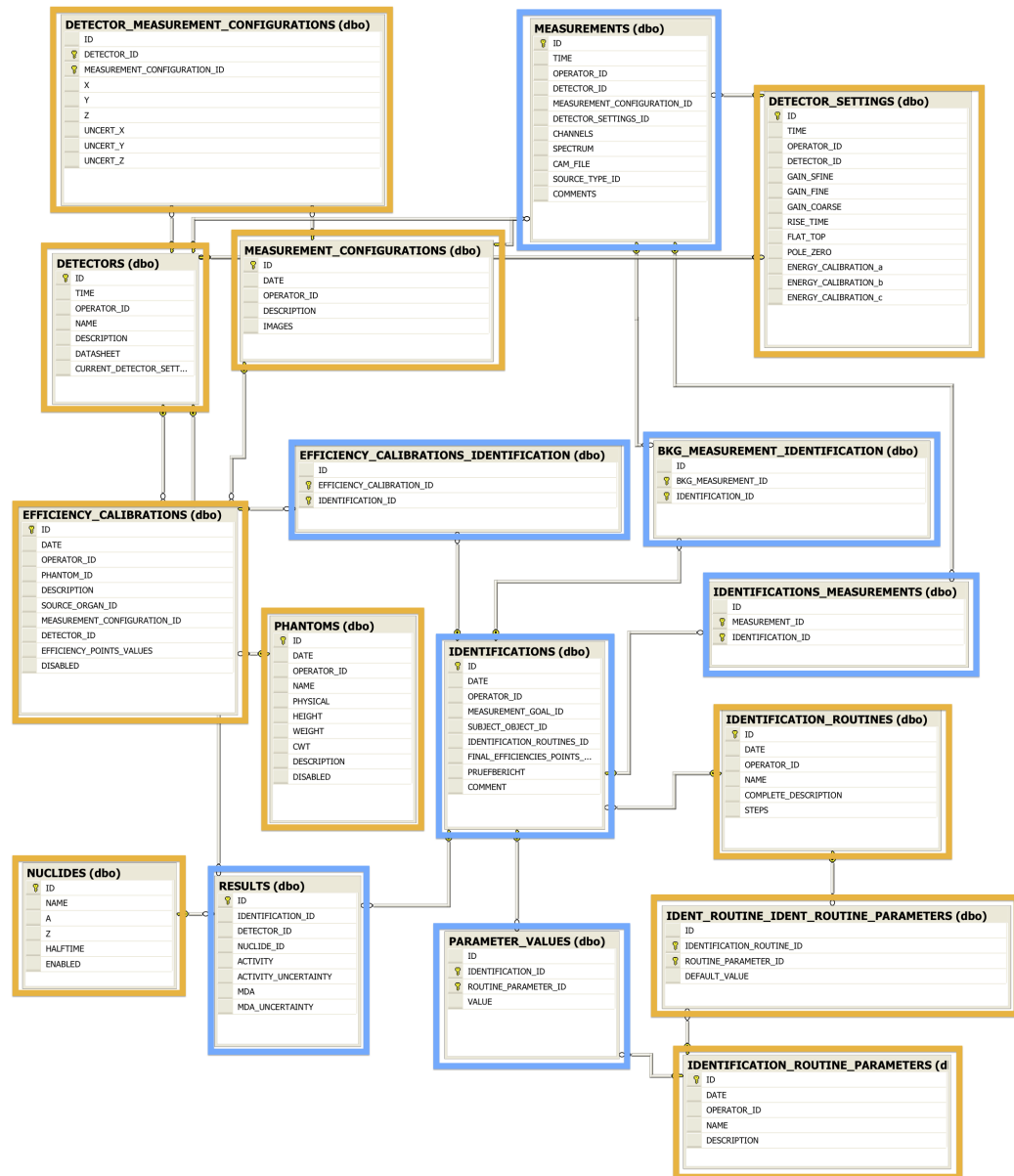


Figure A.1: Structure of the database. Tables marked in orange contain settings or required data that do not change regularly, tables marked in blue contain data produced during measurements and identifications.

Identifications An identification is a process that takes multiple input spectra and produces an estimate of the activities detected. In addition to the information on the specific subject measured, the identification routine and the final efficiency values used for the processing are indicated. The spectra used are not saved in this table because their number may change, therefore an additional table tracks the associations measurements/identifications. Measurements and identifications were split also to allow the user to analyse the same spectra multiple times, for example to experiment with different parameters or with different source organs.

Results Different records are produced per identification: each one reports the activity and the MDA of a specific nuclide found or not found in the subject.

Identification Routines This table lists the different routines available to the user. To make the software as versatile as possible, the steps were not saved in the source code, but in this specific table: a field lists which ones have to be executed and the software simply calls the correct routines. For example, the analysis routine used to measure the background contains only ‘PS_CAN’, meaning that after the spectrum has been acquired, the different peaks are located and each area calculated without further steps. The suffix ‘_CAN’ means that the algorithm from Canberra will be used, but custom algorithms are possible.

Identification Routine Parameters This table lists the default parameters used for the analysis. Each one is copied to the CAM file before processing with the algorithms from Canberra and, after the analysis, it is copied to another table that relates parameters to identifications. The goal of this latter table is to store the effective values, since the defaults can change, and to make the search of identifications that used specific parameters easy: if an error on a parameter is found, the identifications affected must be executed again.

Efficiency Calibrations This table contains the efficiencies calculated with MCNPX or measured with phantoms. Each record stores, in addition to the energy/efficiency pairs, links to the tables describing the phantom, the source organ, the measurement configuration and the detector used.

Efficiency Calibrations Identifications This table connects identifications and efficiencies used to generate the final curve. If manual values are entered in the efficiency calibration window, this table does not list any record for that specific identification.

A.2 Software and Routines

A.2.1 Energy Calibration

The energy calibration routine uses three peaks to calculate the correct gain for the amplification stage of the detectors. The location of the peaks can be customised, but the software already suggests ^{241}Am (59.5 keV), ^{137}Cs (661 keV) and ^{60}Co (1173 keV, 1332 keV) because they span almost the whole energy range of the detectors (15-2000 keV) and they are easily available.

Given the three expected positions, the software searches the regions within 40 channels around them for the highest channel. This can be useful if the sources used are weak and the background peaks are stronger than the calibration peaks. It can be useful also to exclude the low-energy noise found sometimes below 20 keV.

The exact position of each peak is not calculated as the highest channel (it would be too approximate) and not with a Gaussian peak fitting (the increase in accuracy is not worth the effort), but as a simple weighted mean of the number of counts around the highest channel:

$$C = \frac{\sum_{j=M}^N I(j) \cdot j}{\sum_{j=M}^N I(j)} \quad (\text{A.1})$$

where

C is the centre of the peak, expressed as channels;

M is the starting channel used;

N is the end channel used;

$I(j)$ is the number of counts in the channel j .

At the time being, the region used for the calculation (from M to N) is 9 channels, corresponding to the total width of peaks in the low-energy regions of the detectors available at IVM.

The new gain is obtained as weighted average of the ratios between expected and measured peak positions:

$$G_f = G_c \frac{\sum_{i=1}^3 C_i^2 / P_i}{\sum_{i=1}^3 C_i} \quad (\text{A.2})$$

where

G_f is the final gain;

G_c is the current gain;

C_i is the expected channel of the peak i ;

P_i is the current position of the peak i , expressed in channels.

At the time being the routine operates only on the slope of a linear calibration and no offset is used, because they would range from -0.25 keV to 0.25 keV. Future tests will determine the advantages of a calibration with variable offset and, if needed, the routine will be improved.

A.2.2 Interpolation of Energy Points

In the ‘efficiency calibration’ step, the efficiency curve is generated for each detector according to the CWT of the subject and to the different input calibrations selected by the user. A diagram illustrating the procedure is shown in figure A.2.

Different curves may use different energies, therefore an interpolation is required to uniform the calibration sets. As already discussed in section 3.3.1, different degrees of approximation are possible for the interpolation, depending on the number of available points and on the detector used. For example, small coaxial detectors can be correctly calibrated with a single polynomial of appropriate order (up to fifth), but bigger crystals present a constant detection

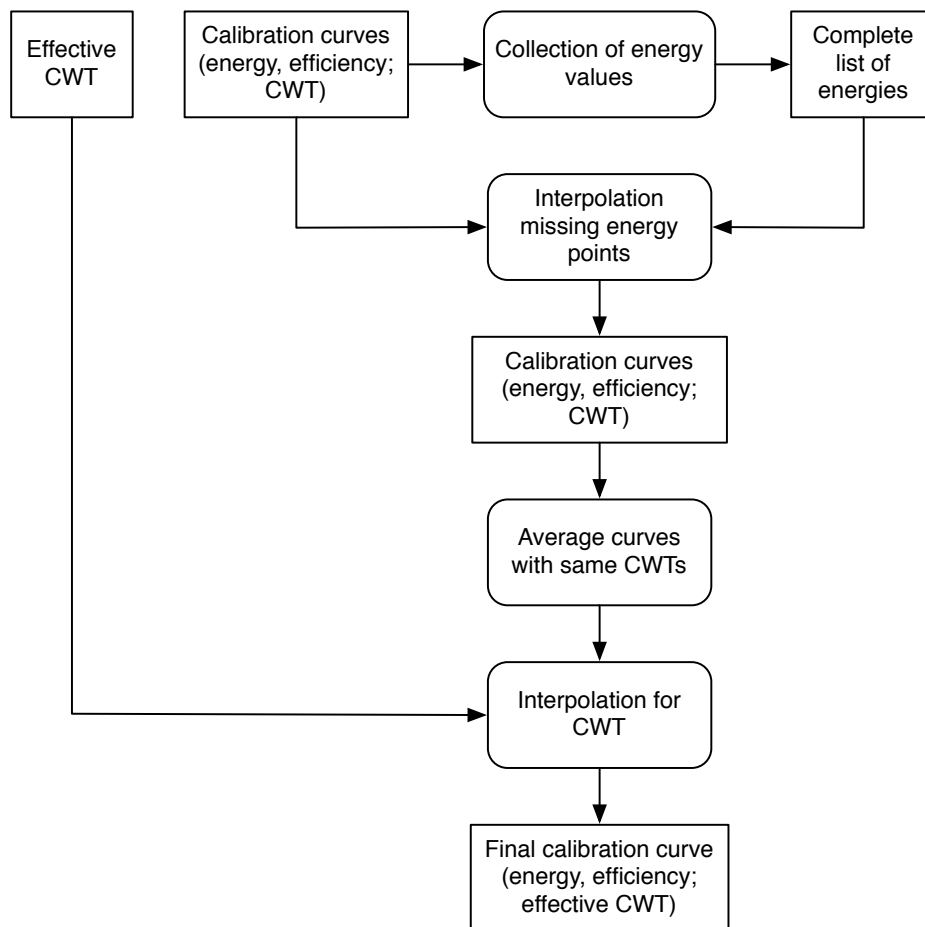


Figure A.2: Diagram of the interpolation steps performed during the calibration. Data in square boxes, processes in rounded boxes.

efficiency (for point sources in air) that cannot be correctly modelled with a single polynomial (see figure 3.3). In this case dual polynomial are used, one for the low-energy region and one for the higher-energies. These polynomials interpolate all the efficiency points given in the corresponding energy region. This software, however, will be using mostly calibrations obtained with MCNPX simulations, where a higher number of calibration points is available. Since the points can be closely spaced, a linear interpolation in logarithmic scale has been implemented.

The routine that calculates the efficiencies generates first a list of all energies provided in the calibration sets selected by the user. Each calibration curve is then processed and the missing efficiency points interpolated using the following formula:

$$\log \eta = \log \eta_1 + (\log E - \log E_1) \frac{\log \eta_2 - \log \eta_1}{\log E_2 - \log E_1} \quad (\text{A.3})$$

where

E is the energy whose efficiency is missing;

η is the efficiency for the energy E ;

E_1 and E_2 are the energies of the nearest available points;

η_1 and η_2 are the efficiencies calculated for the nearest available points.

After all the curves have been processed, those corresponding to the same CWTs are averaged and only one curve per CWT is left.

The final step is the generation of the efficiencies for the CWT of the specific subject. Since the absorption of photons in matter follows a decaying exponential law, a regression algorithm is first used independently on each energy to estimate the parameters of the exponential, then the function is calculated for the desired CWT.

The algorithm used for the regression (Fair, 2008) is linear, therefore a logarithm is applied to the efficiencies. The weights should reflect the errors corresponding to changes in the input parameters. To calculate them for the case where a function is applied to the input data, a first approximation is:

$$\Delta f \approx \frac{df}{dy} \Delta y \quad (\text{A.4})$$

$$\Delta y \approx \left(\frac{df}{dy} \right)^{-1} \Delta f \quad (\text{A.5})$$

$$w (\Delta y)^2 \approx \left(\frac{df}{dy} \right)^{-2} (\Delta f)^2 \quad (\text{A.6})$$

$$w \approx \left(\frac{df}{dy} \right)^{-2} \quad (\text{A.7})$$

where

f is the function used to transform the data (in this case, a logarithm);

y is the parameter interpolated, in this case an efficiency;

w is the weight used in the regression.

In case of a logarithmic transformation, $w = y^2$.

The final curve, defined for all energies of the input calibration set and interpolated for the CWT of the specific subject, is then saved and the analysis routine defined in the database is started.

Appendix B

Publications

List of publications produced as part of the present project.

B.1 Peer-Reviewed Articles

Hegenbart, L., Marzocchi, O., Breustedt, B. et al. *Validation of a Monte Carlo efficiency calibration procedure for a partial body counter system with a voxel model of the LLNL torso phantom*. Radiation Protection Dosimetry, 133(3):158–164, 2009

Marzocchi, O., Breustedt, B. and Urban, M. *Characterisation, modelling and optimisation of the model of a HPGe detector with the aid of point sources*. Appl Radiat Isot, 2009. doi: 10.1016/j.apradiso.2009.11.022

Marzocchi, O., Breustedt, B., Mostacci, D. et al. *Theoretical Assessment of Whole Body Counting Performances Using Numerical Phantoms of Different Gender and Sizes*. Radiat Prot Dosimetry, 2010b. doi: 10.1093/rpd/ncq319

Marzocchi, O., Breustedt, B., Mostacci, D. et al. *Comparison of stretched and sitting configurations for partial-body measurements*. Applied Radiation and Isotopes, In Press, Corrected Proof, 2010a. doi: DOI:10.1016/j.apradiso.2010.11.012

Elanique, A., Marzocchi, O., Leone, D. et al. *Dead layer thickness characterization of an HPGe detector by measurements and Monte Carlo simulations*. Appl. Radiat. Isot., 2011. Submitted

B.2 Internal Reports

Marzocchi, O. *Characterisation of a Canberra Cryo Pulse CP-5 Radiation Detector*;

Marzocchi, O. *Measurements of a Subject Contaminated with Am-241: Comparison of Results obtained with a Cryo Pulse CP5 and Obtained with Computational Simulations of a MEEtman Phantom* published in:

Urban, M. and Bickel, A. *Jahresbericht 2007 der Hauptabteilung Sicherheit*. Technical Report 7410, Hauptabteilung Sicherheit, 2007

Marzocchi, O., Mohr, U., Breustedt, B. *Intercomparison exercise 2008: comparison of results obtained in a whole body counter with either four NaI detectors or two HPGe detectors*;

Marzocchi, O. *Use of voxels phantoms for the optimisation of partial body counting Detector set-ups for the measurement with HPGe detectors of the radioactivity in different organs*;

Hegenbart, L., Marzocchi, O. *Validation of a Numerical Efficiency Calibration Procedure for a Partial Body Counter System with a Voxel Model of the LL-Realistic-Torso-Phantom* published in:

Urban, M. and Bickel, A. *Jahresbericht 2008 der Hauptabteilung Sicherheit*. Technical Report 7476, Hauptabteilung Sicherheit, 2009

Marzocchi, O., Gerblich, N., Breustedt, B. *Erstellung und Validierung von Detektormodellen für den MCNPX-Code*;

Marzocchi, O., Breustedt, B., Urban, M. *Definition der Detektorkonfigurationen für Ganz und Teilkörpermessungen*;

Marzocchi, O., Ugi, S., Liedtke, T., Arend, F. *Entwicklung und Test der Detektorhalterungen*;

Mohr, U., Breustedt, B., Marzocchi, O., Cordes, G., Biegard, N. *Ringvergleiche* published in:

Knebel, J. U. and Mohr, U. *Jahresbericht 2009*. Technical Report 7552, Institut für Strahlenforschung, 2010

B.3 Conference Proceedings

Marzocchi, O. and Breustedt, B. *Measurements of a Subject Contaminated with ^{241}Am : Comparison of Results Obtained with Different Calibration Methods and a Canberra Xtra HPGe Detector*. In e.V. und Kerntechnische Gesellschaft e.V., D. A. (editor), *Jahrestagung Kerntechnik 2009 Proceedings*. Kerntechnische Gesellschaft e.V. (KTG), INFORUM Verlags- und Verwaltungsgesellschaft mbH, Berlin, 2009

Marzocchi, O., Breustedt, B. and Zankl, M. *Placement of HPGe Detectors for Whole Body Counting Applications Using Simulations of Voxel Phantoms*. In e.V. und Kerntechnische Gesellschaft e.V., D. A. (editor), *Jahrestagung Kerntechnik 2010 Proceedings*. Kerntechnische Gesellschaft e.V. (KTG), INFORUM Verlags- und Verwaltungsgesellschaft mbH, Berlin, 2010c

Bibliography

- Akkurt, H. and Eckerman, K. F. *Development of PIMAL: Mathematical Phantom with Moving Arms and Legs*. Technical Report ORNL/TM-2007/14, Oak Ridge National Laboratory, 2007.
- Allison, J., Amako, K., Apostolakis, J. et al. *Geant4 developments and applications*. IEEE Transactions on Nuclear Science, 53(1):270–278, 2006.
- Canberra Industries, Inc. *DSA-1000 Digital Spectrum Analyzer Hardware Manual*. 800 Research Parkway, Meriden, CT 06450, USA, 2005.
- Canberra Industries, Inc. *Genie 2000 Spectroscopy Software Customization Tools v 3.1*. 800 Research Parkway, Meriden, CT 06450, USA, 2006a.
- Canberra Industries, Inc. *Genie™ 2000 Gamma Analysis Software v.3.1*. 2006b.
- Canberra Industries Inc. *Extended Range Coaxial Ge Detectors (XtRa)*. Retrieved on the 23th of December 2010, 2010a. <http://www.canberra.com/products/496.asp>.
- Canberra Industries Inc. *Germanium Detectors*. Retrieved on the 2nd of January 2011, 2010b. <http://www.canberra.com/products/465.asp>.
- Canberra Industries Inc. *DSA-1000 Desktop Spectrum Analyzer*. Retrieved on the 26th of January 2011, 2011. <http://www.canberra.com/products/635.asp>.
- Cosmoderm Reichert GmbH. *Cosmoderm: Firmenprofil*. Retrieved on the 24th of January 2011, 2011. <http://www.cosmoderm.de/profil/index.html>.
- Currie, L. A. *Limits for qualitative detection and quantitative determination. Application to radiochemistry*. Analytical Chemistry, 40(3):586–593, 1968. doi: 10.1021/ac60259a007. <http://pubs.acs.org/doi/pdf/10.1021/ac60259a007>.

- Dean, P. N. *Estimation of chest wall thickness in lung counting for plutonium*. Health Phys, 24(4):439–441, 1973.
- Decay Data Evaluation Project. *Recommended Data*. Retrieved on the 23th of December 2010, 2010. http://www.nucleide.org/DDEP_WG/DDEPdata.htm.
- Doerfel, H., Heide, B. and Sohlin, M. *Entwicklung eines Verfahrens zur numerischen Kalibrierung von Teilkörperzählern*. Wissenschaftlicher Bericht FZKA 7238, Forschungszentrum Karlsruhe, 2006.
- Eisenbud, M., Laurer, G. R., Rosen, J. C. et al. *In Vivo Measurement of Lead-210 As an Indicator of Cumulative Radon Daughter Exposure in Uranium Miners*. Health Physics, 16(5), 1969.
- Elanique, A., Marzocchi, O., Leone, D. et al. *Dead layer thickness characterization of an HPGe detector by measurements and Monte Carlo simulations*. Appl. Radiat. Isot., 2011. Submitted.
- Fair, W. J. *An Algorithm for Weighted Linear Regression*. Retrieved on the 8th of March 2011, 2008. <http://www.codeproject.com/KB/recipes/LinReg.aspx>.
- Fry, F. A. and Sumerling, T. *Measurement of chest wall thickness for assessment of plutonium in human lungs*. Health Phys, 39(1):89–92, 1980.
- Geiger, H. and Müller, W. *Elektronenzählrohr zur Messung schwächster Aktivitäten*. Naturwissenschaften, 16:617–618, 1928. 10.1007/BF01494093.
- Genicot, L. J., Geboers, I., Damen, A. et al. *The reduction of limits of detection in in vivo counting of low-energy photon emitters by optimising the shape and size of detectors*. Radiation Protection Dosimetry, 105(1-4):457–462, 2003. <http://rpd.oxfordjournals.org/content/105/1-4/457.full.pdf+html>.
- Gerblich, N. *Erstellung und Validierung von Detektormodellen für den MCNPX-Code*. Bachelorarbeit, Berufsakademie Karlsruhe, 2009.
- Gómez-Ros, J., de Carlan, L., Franck, D. et al. *Monte Carlo modelling of Germanium detectors for the measurement of low energy photons in internal dosimetry: Results of an international comparison*. Radiation Measurements, 43(2-6):510 – 515, 2008. doi: DOI:10.1016/j.radmeas.2007.12.023. Proceedings of the 15th Solid State Dosimetry (SSD15).

- Griffith, R. V., Anderson, A. L., Dean, P. N. et al. *Tissue-Equivalent Torso Phantom for Calibration of Transuranic Nuclide Counting Facilities*. Radiobioassay and Internal Dosimetry Work Shop, Albuquerque, NM, 1986.
- Gualdrini, G. and Ferrari, P. *A review of voxel model development and radiation protection applications at ENEA*. Radiation Protection Dosimetry, 140(4):383–390, 2010. doi: 10.1093/rpd/ncq124. <http://rpd.oxfordjournals.org/content/140/4/383.full.pdf+html>.
- Gün, H. *Bestimmung der Brustwandstärke als Kalibrierparameter für Teilkörpermessungen*. Diplomarbeit, Fachhochschule Giessen Friedberg, 2010.
- Hegenbart, L. *Numerical Efficiency Calibration of In Vivo Measurement Systems*. Ph.D. thesis, Universität Karlsruhe (TH), 2009.
- Hegenbart, L., Marzocchi, O., Breustedt, B. et al. *Validation of a Monte Carlo efficiency calibration procedure for a partial body counter system with a voxel model of the LLNL torso phantom*. Radiation Protection Dosimetry, 133(3):158–164, 2009.
- Hegenbart, L., Na, Y. H., Zhang, J. Y. et al. *A Monte Carlo study of lung counting efficiency for female workers of different breast sizes using deformable phantoms*. Physics in Medicine and Biology, 53(19):5527, 2008.
- IGOR. *Technical documents for human whole body phantom*. Research and Technical Centre “Protection”, Saint Petersburg, Russia, 1997.
- International Commission on Radiation Units and Measurements. *ICRU Report 48 – Phantoms and Computational Models in Therapy, Diagnosis and Protection*, volume 3 of *Journal of the ICRU*. Nuclear Technology Publishing, 1992.
- International Commission on Radiation Units and Measurements. *ICRU Report 69 – Direct Determination of the Body Content of Radionuclides*, volume 3 of *Journal of the ICRU*. Nuclear Technology Publishing, 2003.
- International Commission on Radiological Protection. *ICRP Publication 23 – Report of the Task Group on Reference Man*. Pergamon Press, 1975.
- International Commission on Radiological Protection. *ICRP Publication 67 – Age-Dependent Doses to Members of the Public from Intake of Radionuclides: Part 2 Ingestion Dose Coefficients*. Pergamon Press, 1993.

- International Commission on Radiological Protection. *ICRP Publication 78 – Individual Monitoring for Internal Exposure of Workers*, volume 27 of *Annals of the ICRP*. Elsevier Science, 1998.
- International Commission on Radiological Protection. *ICRP Publication 89 – Basic Anatomical and Physiological Data for Use in Radiological Protection: Reference Values*. Number 89 in *Annals of the ICRP*. Elsevier Science, 2002.
- International Commission on Radiological Protection. *ICRP Publication 110 – Adult Reference Computational Phantoms*, volume 39 of *Annals of the ICRP*. Elsevier Ltd., 2009.
- ISO11929. *ISO 11929 – Determination of the characteristic limits (decision threshold, detection limit and limits of the confidence interval) for measurements of ionizing radiation – Fundamentals and application*. ISO, International Standards for Business, Government and Society, 2010.
- Johnson, J. B. *Thermal Agitation of Electricity in Conductors*. *Phys. Rev.*, 32(1):97, 1928. doi: 10.1103/PhysRev.32.97.
- Kawrakow, I. and Fippel, M. *Investigation of variance reduction techniques for Monte Carlo photon dose calculation using XVMC*. *Phys. Med. Biol.*, 45(8):2163–2183, 2000.
- Kawrakow, I., Mainegra-Hing, E. and Rogers, D. W. O. *EGSnrcMP: the multi-platform environment for EGSnrc*. Technical Report PIRS-877, National Research Council of Canada, Ottawa, Canada, 2003.
- Kitware Inc. *VTK file formats for VTK Version 4.2.1*. 2003. <http://www.vtk.org/>.
- Kitware Inc. *Paraview 3.61*. 2008-09. <http://www.paraview.org/>.
- Knebel, J. U. and Mohr, U. *Jahresbericht 2009*. Technical Report 7552, Institut für Strahlenforschung, 2010.
- Knoll, G. F. *Radiation Detection and Measurement*. Wiley, 3rd edition, 2000.
- Kovtun, A., Firsanov, V., Fominykh, V. et al. *Metrological Parameters of the Unified Calibration Whole-Body Phantom with Gamma-Emitting Radionuclides*. *Radiation Protection Dosimetry*, 89(3-4):239–242, 2000. <http://rpd.oxfordjournals.org/content/89/3-4/239.full.pdf+html>.

- Kramer, B. M., G. H. Hauck. *Comparison of the 1st, 2nd and 3rd Generation Lawrence Livermore National Laboratory Torso Phantoms*. Radiation Protection Dosimetry, 102(4):323–332, 2002. <http://rpd.oxfordjournals.org/content/102/4/323.full.pdf+html>.
- Kramer, G. H., Hauck, B. M. and Allen, S. A. *Comparison of the LLNL and JAERI torso phantoms using Ge detectors and phoswich detectors*. Health Phys, 74(5):594–601, 1998.
- Leone, D. and Breustedt, B. *Simulation of Phoswich Detectors Using MCNPX and EGSnrc*. Radiation Protection Dosimetry, 2010. doi: 10.1093/rpd/ncq507. <http://rpd.oxfordjournals.org/content/early/2010/12/22/rpd.ncq507.full.pdf+html>.
- Lynch, T. P., Tolmachev, S. Y. and James, A. C. *Estimating ^{241}Am activity in the body: comparison of direct measurements and radiochemical analyses*. Radiation Protection Dosimetry, 134(2):94–101, 2009. doi: 10.1093/rpd/ncp089. <http://rpd.oxfordjournals.org/content/134/2/94.full.pdf+html>.
- Manohari, M., Mathiyarasu, R., Rajagopal, V. et al. *Calibration of Phoswich-Bades Lung Counting System Using Realistic Chest Phantom*. Radiation Protection Dosimetry, 2010. doi: 10.1093/rpd/ncq325. <http://rpd.oxfordjournals.org/content/early/2010/11/01/rpd.ncq325.full.pdf+html>.
- Markku, J. K., Pertti, A. A. and Jorma, T. R. *SAMPO80: An accurate gamma spectrum analysis method for minicomputers*. Nuclear Instruments and Methods in Physics Research, 190(1):89–99, 1981. doi: DOI:10.1016/0029-554X(81)90209-3.
- Martland, H. S., Conlon, P. and Knep, J. P. *Some Unrecognized Dangers in the Use and Handling of Radioactive Substances*. Journal of the American Medical Association, 85(23):1769–1776, 1925. doi: 10.1001/jama.1925.02670230001001. <http://jama.ama-assn.org/content/85/23/1769.full.pdf+html>.
- Marzocchi, O. and Breustedt, B. *Measurements of a Subject Contaminated with ^{241}Am : Comparison of Results Obtained with Different Calibration Methods and a Canberra Xtra HPGe Detector*. In e.V. und Kerntechnische Gesellschaft e.V., D. A. (editor), *Jahrestagung Kerntechnik 2009 Proceedings*. Kerntechnische Gesellschaft e.V. (KTG), INFORUM Verlags- und Verwaltungsgesellschaft mbH, Berlin, 2009.

- Marzocchi, O., Breustedt, B., Mostacci, D. et al. *Comparison of stretched and sitting configurations for partial-body measurements*. Applied Radiation and Isotopes, In Press, Corrected Proof, 2010a. doi: DOI:10.1016/j.apradiso.2010.11.012.
- Marzocchi, O., Breustedt, B., Mostacci, D. et al. *Theoretical Assessment of Whole Body Counting Performances Using Numerical Phantoms of Different Gender and Sizes*. Radiat Prot Dosimetry, 2010b. doi: 10.1093/rpd/ncq319.
- Marzocchi, O., Breustedt, B. and Urban, M. *Characterisation, modelling and optimisation of the model of a HPGe detector with the aid of point sources*. Appl Radiat Isot, 2009. doi: 10.1016/j.apradiso.2009.11.022.
- Marzocchi, O., Breustedt, B. and Zankl, M. *Placement of HPGe Detectors for Whole Body Counting Applications Using Simulations of Voxel Phantoms*. In e.V. und Kerntechnische Gesellschaft e.V., D. A. (editor), *Jahrestagung Kerntechnik 2010 Proceedings*. Kerntechnische Gesellschaft e.V. (KTG), INFORUM Verlags- und Verwaltungsgesellschaft mbH, Berlin, 2010c.
- Microsoft Corporation. *Microsoft Excel 2010*. 2011. <http://office.microsoft.com/en-us/excel/>.
- Mohr, U. and Breustedt, B. *Messung von inkorporierten Radionukliden mittels Gammaskpektrometrie im Teilkörperzähler mit Phoswichdetektor*. Method Description MB-HS-012 Rev. 1, Hauptabteilung Sicherheit - KES, 2007.
- Mottaghian, M., Koochi-Fayegh, R., Ghal-Eh, N. et al. *Photocathode non-uniformity contribution to the energy resolution of scintillators*. Radiation Protection Dosimetry, 140(1):16–24, 2010. doi: 10.1093/rpd/ncq041. <http://rpd.oxfordjournals.org/content/140/1/16.full.pdf+html>.
- Muikku, M., Rahola, T., Pusa, S. et al. *Estimation of human exposure to natural radionuclides by using in vivo skull measurements*. Radiat Prot Dosimetry, 105(1-4):615–618, 2003. <http://rpd.oxfordjournals.org/cgi/reprint/105/1-4/615.pdf>.
- Nelson, H., W. R. and Hirayama and Rogers, D. W. O. *The EGS4 Code System*. Technical Report SLAC-265, Stanford Linear Accelerator, 1985.
- Pelowitz, D. G. *MCNPX User's Manual version 2.5.0*. Technical Report LA-CP-05-0369, Los Alamos National Laboratory, 2005.

- Rimpler, A. and Barth, I. *Beta radiation exposure of medical staff and implications for extremity dose monitoring*. Radiation Protection Dosimetry, 125(1-4):335–339, 2007. doi: 10.1093/rpd/ncl384. <http://rpd.oxfordjournals.org/content/125/1-4/335.full.pdf+html>.
- Ryan, M. and Poston, S., J. W. (editors). *A Half Century of Health Physics - A Historical Review*. Lippincott Williams & Wilkins, 2006.
- Sachse, F. B., Werner, C. D., Meyer-Waarden, K. et al. *Development of a human body model for numerical calculation of electrical fields*. Comput Med Imaging Graph, 24(3):165–171, 2000.
- Salvat, F., Fernandez-Varea, J. M. and Sempau, J. *PENELOPE-2006, A Code System for Monte Carlo Simulation of Electron and Photon Transport*. In *Workshop Proceedings, NEA-6222*. OECD, Barcelona, Spain, 2006.
- Sangster, K. *Bestimmung der optimalen Pulsformparameter eines DSA 1000 für verschiedene Germaniumdetektortypen*. Projektarbeit, Berufsakademie Karlsruhe, 2007.
- Schläger, M. *Precise modelling of coaxial germanium detectors in preparation for a mathematical calibration*. Nuclear Instruments and Methods in Physics Research Section A: Accelerators, Spectrometers, Detectors and Associated Equipment, 580(1):137–140, 2007.
- Schroeder, W., Martin, K. and Lorensen, B. *Visualization Toolkit*. Kitware, Inc., 4th edition, 2006.
- Schwabenland, F. *Am241 head phantom*. Master's thesis, DH, 2010.
- Sessler, S. *Numerische Simulation von im Karlsruher Ganzkörperzähler gemessenen IGOR-Spektren*. Diplomarbeit, Berufakademie Karlsruhe, 2007.
- Snyder, W. S., Fisher, H. L. J., Ford, M. R. et al. *Estimates of absorbed fractions for monoenergetic photon sources uniformly distributed in various organs of a heterogeneous phantom*. J Nucl Med, 3:7–52, 1969.
- Soil, H., Viol, C. and Gordon, M. *The elimination of soluble radium salts taken intravenously and per os*. New York Med. J., 101:896–898, 1915.
- The Perl Foundation. *Perl 5.8.8*. 2008. <http://www.perl.org>.
- Tilley, A. R. *The Measure of Man and Woman. Human factors in design*. Wiley, 2002.

- Urban, M. and Bickel, A. *Jahresbericht 2007 der Hauptabteilung Sicherheit*. Technical Report 7410, Hauptabteilung Sicherheit, 2007.
- Urban, M. and Bickel, A. *Jahresbericht 2008 der Hauptabteilung Sicherheit*. Technical Report 7476, Hauptabteilung Sicherheit, 2009.
- U.S. Environmental Protection Agency. *Common Industrial Devices and Other Uses of Radioactive Sources*. Retrieved on the 23th of December 2010, 2010. <http://www.epa.gov/rpdweb00/source-reduction-management/applications.html>.
- Wahl, W., Haninger, T., Kucheida, D. et al. *Study of Long-Term Radon Progeny in Humans for Retrospective Evaluation of Radon Exposure*. Journal of Radioanalytical and Nuclear Chemistry, 243:447–450, 2000. 10.1023/A:1016078115609.
- X-5 Monte Carlo Team. *MCNP – A General Monte Carlo N-Particle Transport Code, Version 5*. Technical Report LA-UR-03-1987, Los Alamos National Laboratory, 2008.
- Xu, X. G., Zhang, J. Y. and Na, Y. H. *Preliminary Data for Mesh-Based Deformable Phantom Development: Is it Possible to Design Person-Specific Phantoms On-demand*. In *The International Conference on Radiation Shielding-11*. Pine Mountain, GA, 2008.
- Zankl, M., Becker, J., Fill, U. et al. *GSF male and female adult voxel models representing ICRP Reference Man – the present status*. In *The Monte Carlo Method: Versatility Unbounded in a Dynamic Computing World*. (American Nuclear Society, La Grange Park, USA, 2005. Submitted.
- Zankl, M., Petoussi-Henss, N., Fill, U. et al. *The application of voxel phantoms to the internal dosimetry of radionuclides*. Radiation Protection Dosimetry, 105(1-4):539–547, 2003. <http://rpd.oxfordjournals.org/content/105/1-4/539.full.pdf+html>.
- Zubal, I. G. *The Zubal Phantoms*. 2009. <http://noodle.med.yale.edu/zubal/>.

Acronyms

BREP Boundary representative

FWHM Full width at half maximum

GIT Gastrointestinal-tract

HPGe High-purity germanium detector

ICRP International Commission on Radiological Protection

IVM In-vivo monitoring laboratory

JAERI Japan Atomic Energy Research Institute

KIT Karlsruhe Institute of Technology

KSM KIT-Sicherheitsmanagement

LLNL Lawrence Livermore National Laboratory

MC Monte Carlo

MDA Minimum detectable activity

NSD Normalised standard deviation

PMT Photomultiplier tube

QM Quality management

ROI Region of interest

Voxel From vo(lumetric) (pi)xel, 3D equivalent of the 2D pixel.

XtRa Extended range (germanium detector)